Effects of Cholesterol on the Magnetite Nanoparticles Induced Deformation and Poration of Giant Lipid Vesicles

by

Salma Akter

MASTER OF SCIENCE IN PHYSICS

Department of Physics

BANGLADESH UNIVERSITY OF ENGINERRING AND TECHNOLOGY

October, 2022

The thesis titled "Effects of Cholesterol on the Magnetite Nanoparticles Induced Deformation and Poration of Giant Lipid Vesicles" submitted by Salma Akter, Roll No. 0419142501 F, Session: April/2019, has been accepted as satisfactory in partial fulfillment of the requirement for the degree of MASTER OF SCIENCE IN PHYSICS on 29 October, 2022.

BOARD OF EXAMINERS

Dr. Mohammade Abu Sayem Karal
Professor
Department of Physics, BUET, Dhaka

Chairman
(Supervisor)

Dr. Nasreen Akter
Professor and Head
Department of Physics, BUET, Dhaka

Member
(Ex-Officio)

Dr. A. K. M. Akter Hossain
Professor
Department of Physics, BUET, Dhaka

Member

Dr. Muhammad Samir Ullah
Associate Professor
Department of Physics, BUET, Dhaka

Member

Dr. Md. Aminul Islam Talukder
Professor
Department of Physics
University of Dhaka, Dhaka-1000

Member
(External)

CANDIDATE'S DECLARATION

It is hereby declared that this thesis or any part of it has not been submitted elsewhere for the award of any degree or diploma.

Salma Akter

(Salma Akter)
Roll No. 0419142501 F
Session: April, 2019

Dedicated

To

My Beloved Parents

&

Honorable Teachers

Acknowledgments

Abstract

Cholesterol (chol) is one of the important elements in the cell membranes. We have been investigated the effects of chol on the deformation and poration of cell mimetic giant unilamellar vesicles (GUVs) induced by anionic magnetite nanoparticles (NPs) of average size 18 nm. Lipids and chol are used to prepare the charged and neutral GUVs in which chol varies from 0 to 40 mole% for biologically relevant membranes. The degree of deformation such as compactness remains 1.0 for spherical shaped GUVs, and it increases with time for both charged and neutral membranes. The average compactness decreases with chol, and at 60 min, the values are 1.280 ± 0.002 and 1.131 ± 0.010 for 0 and 40% chol containing charged membranes, respectively, while 1.269 ± 0.008 and 1.099 ± 0.004 for 0 and 40% chol containing neutral membranes, respectively. The values of fraction of deformation are 0.63 ± 0.02 for 0% chol, and 0.24 ± 0.01 for 40% chol in charged membranes, while 0.44 ± 0.02 for 0% chol, and 0.21 ± 0.003 for 40% chol in neutral membranes at 60 min. Membrane poration has been investigated by the leakage of encapsulating fluorescent probe (calcein) of GUVs. The values of fraction of poration are 0.24 ± 0.02 for 0% chol and 0.04 ± 0.01 for 40% chol containing charged membranes, while 0.28 ± 0.06 for 0% chol and 0.05 ± 0.01 for 40% chol containing neutral membranes at 50 min. Both the fraction of poration and fraction of deformation decrease with chol in the membranes. The fraction of deformation is higher for charged GUVs than neutral ones, while the fraction of poration shows the opposite result. The possible mechanism for vesicle deformation and lipid membrane poration has been discussed.

Contents

List of Figures

22 nm sizes NPs may not be completely covered.

the same conditions as shown in (a).

images of a single GUV's demonstrate the deformation. The number on each image depicts the time in minutes after the addition of NPs. Scale bar is 15 μm. (b) The time dependent compactness, C_{om}, of the GUV as shown in (a). (c) The time dependent average compactness, C_{om}^{av} of several GUVs under the same conditions as shown in (a).

the GUV. The time in seconds after the addition of NPs in the GUVs suspension is shown by the number on each image. The scale bar is 15 μm. (b) The time dependent change in normalized fluorescence intensity inside of GUV, as indicated in (a). The inset displays the rapid change in fluorescence intensity with time. (c) The variation in normalized fluorescence intensity for 5 different GUVs under the same conditions as in (b).

same conditions as in (b).

GUVs due to the interaction of 3.33 µg/mL NPs. "Common murre egg-shaped" GUV in (a) and (c), and "stingray fish-shaped" GUV in (b). The time in minute after the addition of NPs is depicted by the number on each image. The scale bar is 15 µm.

List of Table

List of Abbreviations

Symbol	Abbreviations
NPs	Nanoparticles
ULVs	Unilamellar vesicles
MLVs	Multilamellar vesicles
MVVs	Multivesicular vesicles
OLVs	Oligolamellar vesicles
GUVs	Giant Unilamellar Vesicles
LUVs	Large Unilamellar Vesicles
SUVs	Small Unilamellar Vesicles
DOPC	1,2-dioleoyl-sn-glycero-3-phosphocholine
DOPG	1,2-dioleoyl-*sn*-glycero-3-phospho-(1´-*rac*-glycerol)
DLPC	1,2-dilauroyl-*sn*-glycero-3-phosphocholine
DPPC	1,2-dipalmitoyl-*sn*-glycero-3-phosphocholine
SOPC	1-stearoyl-2-oleoyl-*sn*-glycero-3- phosphocholine
POPC	1,2-dipalmitoleoyl-*sn*-glycero-3-phosphocholine
diC22:1PC	1,2-dierucoyl-*sn*glycerol-3-phosphocholine
DMPC	1,2-dimyristoyl-*sn*-glycero-3-phosphocholine
DOTAP	1,2-dioleoyl-3-trimethylammonium propane
DOPE	L-α-dioleoylphosphatidylethanolamine
Rh-DOPE	1,2-dioleoyl-sn-glycero- 3-phosphoethanolamine-*N*-(lissamine rhodamine B sulfonyl)
NBD-DPPE	*N*-(7-nitrobenz-2- oxa-1,3-diazol-4-yl)-dipalmitoylphosphatidylethanolamine
Chol	Cholesterol
PBS	Phosphate buffered saline
MOPS	3-(N-Morpholino)-propanesulfonic acid
AuNPs	Gold Nanoparticles
CSMNs	Charged core-shell magnetic nanoparticles
FCS	Fluorescence Correlation Spectroscopy
FRET	Forster Resonance Energy Transfer
ITC	Isothermal Titration Calorimetry

AFM	Atomic force microscopy
NSE spectroscopy	Neutron spin-echo spectroscopy
^{2}H NMR spectroscopy	Solid-state deuterium NMR spectroscopy
MD simulations	Molecular dynamics simulations
DNA	Deoxyribonucleic Acid
RNA	Ribonucleic Acid
ATP	Adenosine Triphosphate
LDL	Low-density lipoprotine
HDL	High- density lipoprotine
VLDL	Very low- density lipoprotine
XRD	X-Ray Diffraction
MRI	Magnetic Resonance Imaging
nm	Nanometer
PIPES	Piperazine-1, 4-bis (2-ethanesulfonic acid
EGTA	Ethylene glycol-bis (2-aninoethylether)-$N,N,N'N'$-tertraacetic acid
BSA	Bovine serum albumin
PC	Phosphatidylcholine
DI water	De-ionized water

CHAPTER 1

INTRODUCTION

1.1 Background

Nanoparticles (NPs) have unique biophysical and biochemical properties [1], which are largely determined by their size and shape [2, 3]. NPs are used in a variety of areas such as medical [4], pharmacology [5], and biotechnology [5, 6]. In recent years, NPs have been potentially used to identify the cause of and treat certain diseases, including cancer [7, 8]. One of the important applications of NPs is the delivery of drugs into targeted cells [9]. Enhancing the radiotherapy dose with gold NPs (AuNPs) seems to be a promising strategy for better cancer treatment [10]. AuNPs offer a versatile chemical platform for the incorporation of different targeting strategies and the endowment of desirable features. Radiation dose, hyperthermia, temporal fractionation, and beam energy were some of the variables examined [10, 11]. AuNPs systems have been investigated as radio sensitizers among other NPs systems. The quantity of ingested AuNPs in the cells had an impact on the radio sensitization. In comparison to AuNPs with sizes of 14 and 74 nm, those with a diameter of 50 nm had the highest radio sensitization enhancement fact [12].

A new area of potential for cancer treatment is nanotechnology. By creating functionalized particles for focused treatment, it has the potential to reduce systemic toxicity. NPs also offer a different approach to overcome multidrug resistance because they have the ability to avoid the drug effluence mechanism linked to this trait. In addition to the benefits NPs provide in terms of treatment, NPs are also showing promise as useful diagnostic tools [13]. From a variety of studies, it has been confirmed the antibacterial and anticarcinogenic properties of NPs. Due to the high level of interest in employing synthesized NPs for medical applications, it is crucial to evaluate the side effects of NPs on health. Environmental groups have focused a lot of attention on the interaction of NPs with cells. Quantum dots and other designed NPs can enter the cytoplasm of eukaryotes when they are suitably transformed, most likely through receptor-mediated endocytosis. Several severe illnesses have been observed in pulmonary system due to the toxicity of environmentally available NPs [14, 15]. At 200

µg/mL, it has been observed that AuNPs have minimal toxicity, resulting in a 15% reduction in cell viability. While cytotoxicity may be induced at higher concentrations, many chemicals become poisonous at these levels [16]. Cellular toxicity is caused by the release of harmful Zn^{2+} ions as a result of ZnO dissolution through interactions at successive nano-bio interfaces in the extracellular environment and the acidifying lysosome. Zn^{2+} release in the lysosome and intracellular milieu can lead to a number of detrimental cellular effects, including lysosomal degradation, mitochondrial disruption, and the generation of reactive oxygen species, the activation of pro-inflammatory cytokines, and the synthesis of chemokines [17]. Though research on nanotechnology is important for mankind, it is also important to save ourselves from the toxicity of nanomaterials [18].

One of the main reasons for substantial mortality and morbidity in cardiorespiratory illnesses is the emission of NPs from various sources to the environment [19, 20]. Medical implants, contrast agents of MRI, insecticides, and food processing are just a few of the ways NPs enter the human body [21–23]. Due to their small size, NPs can easily diffuse in the air and be inhaled [24]. Synthesis NPs are able to enter the body through six main routes: inhalation, intraperitoneal, intravenous, subcutaneous, dermal, and oral. Once within the body, the NPs engage in interactions with biological elements, including cells and proteins, before being absorbed [15-17]. NPs in the environment can readily enter the body by inhalation and interact with blood cells, causing discomfort in the cardiovascular and pulmonary systems [25].

Iron impurities in burning fuels like diesel, as well as interior sources like printer toners and leaking stoves, are common sources of magnetite NPs [26]. These particles have been found in abundance in human brains, which are common in cities [27]. Such magnetite NPs can directly come to the brain through olfactory nerve, causing a build-up of reactive oxygen species in cells. The increased generation of reactive oxygen species has been linked to neurological illnesses (such as Alzheimer's) [28]. Magnetite NPs have also been discovered in amyloid plaques, which is the aggregation of misfolded proteins [29]. Alzheimer's disease is caused by those misfolded proteins. As a result, the study of the interactions of magnetite NPs with cells and vesicle membranes is critical for determining how cells and vesicles affected by the adsorption of NPs.

Cell membranes, which are a complex structure containing proteins, lipids, cholesterols and lipopolysaccharides, are the main boundary for the interaction of NPs with cells [30]. Membranes show less permeability to water, small molecules, and ions [31-33]. To circumvent the complexities of cell membranes, cholesterol-containing lipid bilayer of giant unilamellar vesicles (GUVs) with sizes (10 μm or more) comparable to cells are being potentially used as a mimic of cell membranes for studying peptide-induced pore formation [34, 35]. Cholesterol (50 mol% of the total lipid content or more) is one of these components that are essential for the proper functioning of a biological system [36]. Although lipids are affected by cholesterol's ordering properties, its impact on the mechanical characteristics of lipid membranes is debatable. It affects membrane flexibility and increases lipid packing density, which both have an impact on the mechanical properties of membranes [31, 32], leaving unresolved issues concerning the mechanism of cholesterol-lipid interaction. The bending modulus is a crucial metric in determining the lipid bilayer's mechanical properties [37]. Cholesterol affects plasma membrane physicochemical activity [38], voltage-gated ion channel kinetics [39], G-protein coupled receptor function [40], and the velocity of motion of hydrophobic tails [41], among other things. Cholesterol also has effect on membrane mechanical stability, strengthening mechanical strength, influencing membrane elasticity, and increasing lipid packing density through 'condensing and ordering' effects [42-44]. Incorporation of cholesterol into the membranes affects the bending rigidity and stiffens them [45]. As the sizes of GUVs are similar to real cells, hence the interaction of different membrane active agents such as peptides, toxins, and NPs has previously been studied [46, 47]. Furthermore, GUVs were used to study mechanical and electrical tension-induced membrane poration [48, 49].

Cholesterol has been shown to impact membrane bending rigidity and area compressibility modulus in various investigations [50–53]. Within the monolayer, at a crucial plane with a constant area, the intrinsic curvature was found to have radii of 29.4 Å for DOPE (L-α-dioleoylphosphatidylethanolamine)/tetradecane at 22 °C and 27 Å at 30 mol% cholesterol. The intrinsic curvature dropped from 62.5 Å to 40 Å for DOPC (1.2-dioleoyl-sn-glycero-3-phosphocholine)/tetradecane at 32 °C as its cholesterol content rose from 30 to 50 mol%. For pure DOPC, the inherent radius of curvature was estimated 87.3 Å. With 30 mol% cholesterol in each, the DOPC/tetradecane and DOPE/tetradecane bending moduli were 15 and 9.0 k_BT,

respectively [50]. The relationship in fluid vesicle membranes between tension and projected surface area has been measured using sensitive micropipette technique throughout a 4-order-of-magnitude tension range. The targeted region increased logarithmically with tension in the low-tension region. The bending modulus of the membranes is obtained from the slope of ln (tension) versus area dilation. Due to the direct expansion of area per molecule in the high-tension region, the predicted area crosses over to vary linearly with tension [52]. Cholesterol's effect on bilayer bending modulus is lipid-specific rather than universal [54, 55]. In the DOPC /chol and DOPG (1,2-dioleoyl-*sn*-glycero-3-phospho-(1´-*rac*-glycerol)/ DOPC/chol vesicles, there is a rising tendency of bending rigidity with cholesterol content [56-58, 37]. The terminal P^- of the dipole of (P^--N^+) of DOPC has been assumed to be tightly connected to the lipid main molecular structure, whereas the terminus N^+ has relative freedom. Anionic NPs' electric field interacts with the N^+ terminal, rises the angle of (P^--N^+) vector tilt. Hence, the interaction of anionic NPs, the electric dipole's normal component increases in relation to the bilayer periphery [47, 59].

1.2 Motivation

Till to date, various features of NPs' interaction with lipid vesicles have been studied [60]. The anionic charged bilayers tended to bind with the cationic core-shell magnetic NPs [61]. Encapsulating cationic NPs caused several sorts of shape changes in neutral DOPC-GUVs, such as protrusion and pearling [62]. As a result of NP binding in membranes, GUVs deform and porate [61, 63]. An investigation of the effects of anionic magnetite NPs (the same NPs utilized here) on the deformation and poration of cholesterol-free DOPG/DOPC-GUVs and DOPC-GUVs has recently been published [59]. Because biological (i.e., human) cells have cholesterol in their membranes, understanding how cholesterol affects lipid vesicle deformation and membrane pore formation by anionic NPs is important. As the cholesterol containing membranes are used for biological relevance of cell membranes, hence the investigations of the effects of magnetite NPs on the deformation and poration in such membranes of GUVs are important. In addition, the NPs-induced cholesterol containing vesicle deformation and poration are not reported yet, which is investigated in this research. Both charged DOPG/DOPC/chol-GUVs and neutral DOPC/chol-GUVs are used for this study.

Cholesterol mole fraction is varied from 0 to 40% in the synthesized lipid membranes. Eco-friendly green synthesis technique is used to synthesize the magnetite NPs.

1.3 Objective of the Present Study

The main objectives of this research are as follows:

i. Synthesis of cholesterol containing charged and neutral membranes of GUVs using the natural swelling method. Purification of GUVs using the membrane filtering method.

ii. Investigations of the deformation, compactness, and poration of GUVs induced by NPs for different cholesterol containing charged and neutral membranes.

iii. Investigations of the fraction of deformation and poration of GUVs at different cholesterol and NPs concentrations.

iv. Comparison the results of compactness, fraction of deformation, fraction of poration, average time of poration between the cholesterol containing neutral and charged GUVs.

v. Reveal the possible mechanism of NPs-induced vesicle deformation and lipid membrane poration in cholesterol containing membranes.

1.4 Outline of the Thesis

The purpose of this thesis is to study the interaction of anionic magnetite NPs and cholesterol containing GUVs. The outline of the thesis is mentioned below:

Chapter one mainly focused on the background and the justification of research. The objectives with specific aims are discussed in this chapter.

Chapter two describes the literature review and theoretical aspects. It also contains basic information about biomembranes, lipid membranes, vesicles, GUVs, NPs, and cholesterol. The biomedical applications of NPs are mentioned here.

Chapter three discusses the materials and methods, which included NPs synthesis, GUVs synthesis, GUVs purification, measuring procedure etc.

Chapter four is the important part of this thesis, which represents the results. The discussion behind the results is described. The mechanism of interaction is illustrated and discussed thoroughly.

Chapter five discusses the overall conclusions of thesis. Future direction of research is presented here.

CHAPTER 2

LITERATURE REVIEW AND THEORETICAL ASPECTS

2.1 Literature Review

Karal *et al*. investigated the deformation and poration of 60%DOPC/40%DOPG-GUVs (% indicates more %) induced by anionic magnetite NPs of size 18 nm [59]. Fig. 2.1 shows the deformation of GUVs over time. The interaction of 3.33 µg/mL NPs with a 'single 60%DOPC/40%DOPG-GUV' is depicted in Fig. 2.1. In the absence of NPs, the GUV has a spherical structure at 0 min, as shown in Fig. 2.1(A). Within the first 2 minutes after adding the NPs to the vesicle suspension, this shape does not change. A little deformation began at 3 min, and a major deformation appeared between 45 and 60 minutes. The compactness, C_{om}, is used to determine the degree of deformation. C_{om} is defined by the following equation,

$$C_{om} = \frac{P^2}{4\pi S_{cr}}$$

(2.1)

where, P denotes the perimeter and S_{cr} denotes the area of the image cross section of GUVs. The time dependent change of C_{om} of GUV as shown in Fig. 2.1(A) is presented in Fig. 2.1(B). The value of C_{om} is 1.0 at 2 min and at 56 min, the C_{om} value is 1.274. The change in average compactness, C_{om}^{av}, of GUVs is shown in Fig. 2.1(C), where C_{om}^{av} increases over time. In each separate experiment, the mean value of compactness, C_{om}^{av}, and standard errors at various times were computed from three different experiments using a total number of 20-30 GUVs (i.e., number of measured GUVs, N = 20-30). When NPs adsorbed to the vesicle membranes, surface area mismatches between the external and internal monolayer occurred, according to the 'bilayer-coupling model' [64]. In this model for a given area S, volume of the GUV, V, and area difference between the two monolayers of the bilayer, $\Delta S = S_{ex} - S_{in}$, where S_{ex} and S_{in} are the areas of the outer and inner monolayer of the membrane, respectively. The shape of the GUV is considered to be determined by minimizing the bending energy of the membrane. Due to the area mismatch between the two monolayers, the outer monolayer shrinks, causing GUVs to bend in order to maintain the lowest surface free energy. It is reasonable to assume that as time passes, NPs absorption at membrane interfaces rises, resulting in increased surface pressure in the lipid membranes which in turn causes C_{om} to rise.
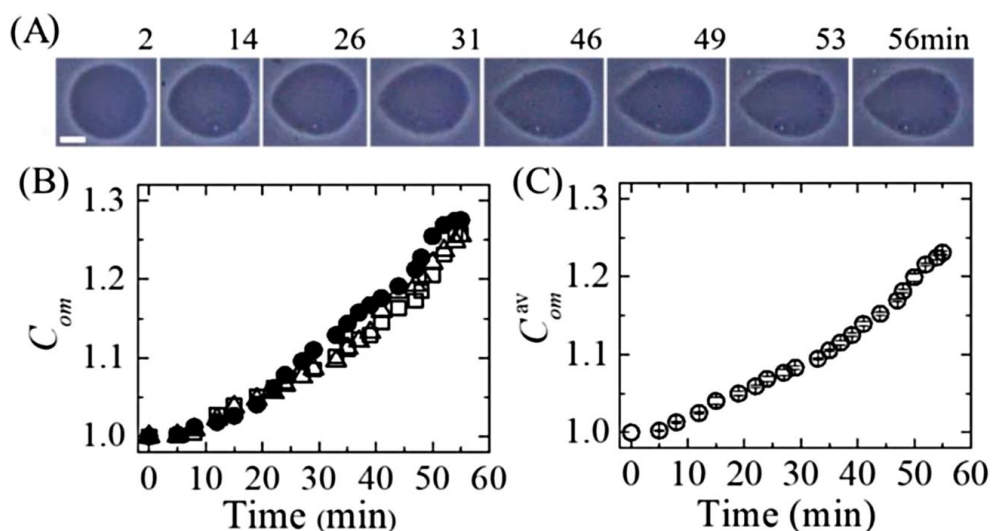
Fig. 2.1 The deformation and the corresponding compactness of 60%DOPC/40%DOPG-GUVs in the presence of 3.33 µg/mL NPs. (A) Phase contrast images of a 'single GUV' demonstrate the deformation. The number on each image depicts the time in minutes after the addition of NPs. Scale bar is 10 µm. (B) The time dependent compactness, C_{om}, of the GUV as shown in (A). (C) The time dependent average compactness, C_{om}^{av} of several GUVs.

The poration in lipid membranes of GUVs is described in Fig. 2.2. Because of the concentration different between the internal (0.10 M sucrose) and the external (0.10 M glucose) of the GUV, there is a significant contrast of light between its interior and exterior of vesicle at 0 s in Fig. 2.2(A). When NPs are added to GUV suspension, the contrast does not change for 90 s, after which the light intensity of the GUV's interior rises with time and after 297 s the light intensity of the GUV's inside and outside are almost equal. The variation in normalized intensity with time is seen in Fig. 2.2(B). Three different 60%DOPC/40%DOPG-GUVs at 3.33 µg/mL NPs is presented in Fig. 2.2(C). The side bar in (B, C) displays the intensity of the GUV's interior.

The discussion of pore formation is presented here. The inner monolayer is stretched as a result of the binding of NPs in the outer monolayer, creating pore(s) in the bilayer. The thermal energy changes the lipid membrane density, where lateral density of lipid molecules would exist. In a stretched membrane, the size of the rarefaction is higher. Such rarefaction transforms into a hydrophilic pre-pore with an effective radius, r, if its size exceeds a critical value, r_c. If $r < r_c$, the pre-pore soon closes; however, if $r = r_c$, the pre-pore becomes a transmembrane pore.
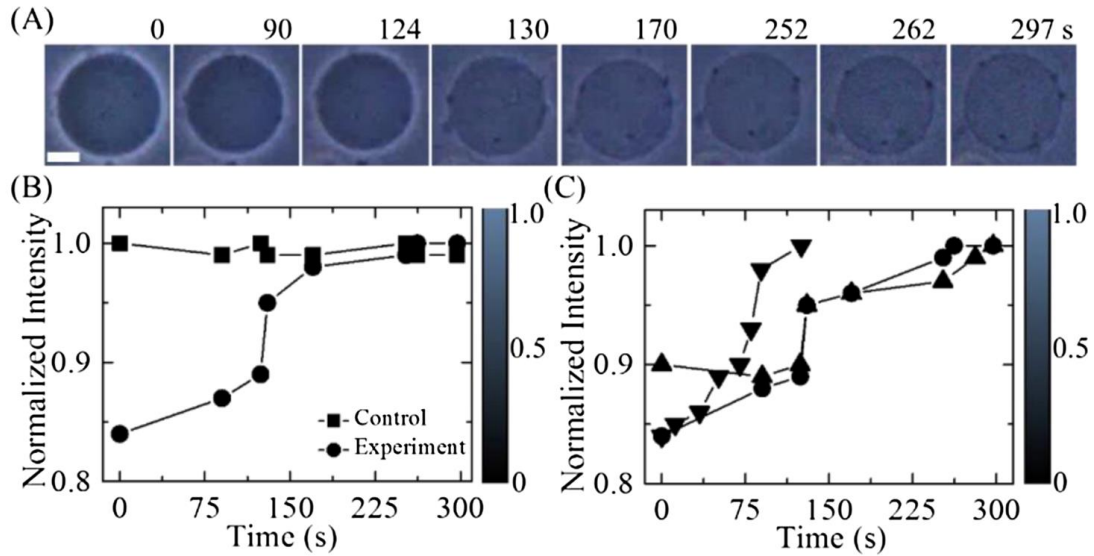
Fig. 2.2 The sucrose releases from 60%DOPC/40%DOPG-GUVs due to the interaction of 3.33 μg/mL NPs. (A) Phase contrast images of a single GUV sucrose release. The number on each image depicts the time in second after the addition of NPs. Scale bar is 10 μm. (B) The time dependent normalized intensity of the GUV as shown in (A). (C) The time dependent normalized intensity of three different GUVs is presented under the same conditions as shown in (A). The side bar in (B, C) displays the intensity of the GUV's interior.

In accordance with the conventional explanation of pore development, the free energy of a pre-pore is defined as follows [65-67],

$$E(r, \sigma_{st}) = 2\pi r \Gamma - \pi r^2 \sigma_{st} \tag{2.2}$$

The terms $-\pi r^2 \sigma_{st}$ and $2\pi r \Gamma$ are used to describe lateral tension (stretching) and line tension, respectively. The stretching is caused by the binding of NPs, which causes the pre-pore to expand. The line tension, Γ tends to decrease the pre-pore. The transmembrane pore formation requires to overcome the barrier energy, $E(r_c) = \frac{\pi \Gamma^2}{\sigma_{st}}$. The development of transmembrane pores in vesicles caused sucrose leak out to the outer environment.

Bhat *et al.* investigated the effects of gold nanoparticles (AuNPs) on packing of lipid molecules and pore formation in the membranes [68]. Large unilamellar vesicle (LUVs) and GUVs were synthesized in PBS (phosphate buffered saline) buffer using DMPC (1,2-dimyristoyl-*sn*-glycero-3-phosphocholine) lipid using the 'thin lipid film extraction method' [69]. They employed citrate-stabilized AuNPs [70], with AuNP diameters

ranging from 5 to 30 nm to match bio- macromolecules and several cell membrane elements. Fluorescent dye was Laurdan, which is a hydrophobic fluorescent probe which is used for evaluating lipid stacking [71]. The structural formulas of DMPC and Laurdan are shown in Fig. 2.3(a & b). In the ordered gel phase, Laurdan's maximum emission is 440 nm for lipids and changes to 490 nm in the disorganized fluid stage (Fig. 2.3c), a red shift produced by enhanced dipolar relaxation of Laurdan's luminous naphthalene moiety [72]. Because the lipids in the gel stage (Fig. 2.3d) are closely stacked, repositioning of water molecules on all sides of the energized dipole of Laurdan is unlikely. In the liquid disordered phase (Fig. 2.3e), however, the elevated concentration and fluidity of water molecules increases Laurdan's dipolar relaxation, causing the emission to move to the red [73-75]. Since the head groups of lipids forfeit their triangle lattice orientation and accept a more disorganized arrangement with increasing inter-molecular spacing as fluidity increases [76], the liposome structure changes from annular to less annular [77].
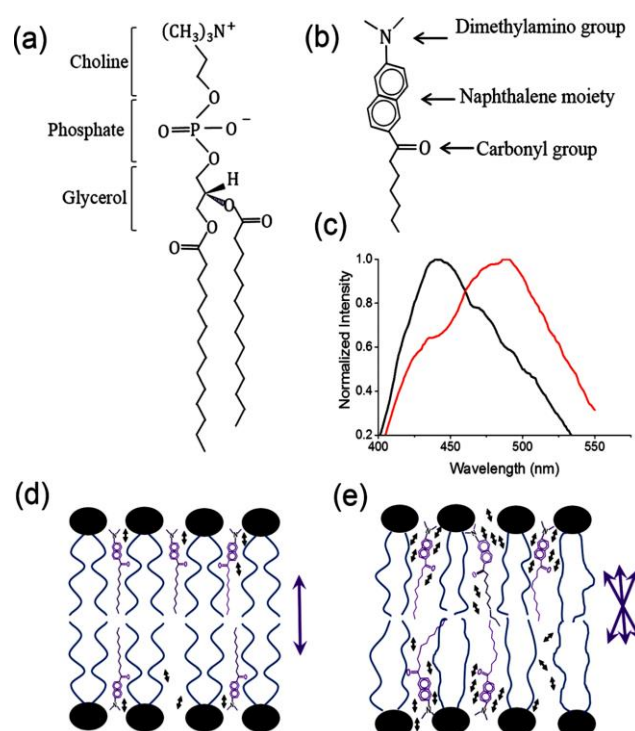
Fig. 2.3 (a) DMPC lipid. (b) Laurdan molecule. (c) Laurdan's fluorescence red shift. (d) Organized DMPC bilayers. (e) Disorganized DMPC bilayers.

The histograms of percent counts for liposomes with low (0-0.5), medium (0.5–0.8), and high (0.8–1) circularities are juxtaposed with delegate fluorescence pictures of Laurdan-labeled liposomes coated with varied shape AuNPs in Fig. 2.4. The population of high-circularity liposomes lacking AuNPs is 86%, the highest of any liposomes studied. With 10 and 30-nm AuNP treatment, rod-like liposomes were observed more frequently, as shown by a substantially higher low- rotundity count of 21% and 17%, in some respects. As a result, the average circularities of 10 and 30 nm AuNPs were 0.77 and 0.82. The fact that AuNP-instigated membrane fluidization results in less annular liposomes is supported by the mean circularities.
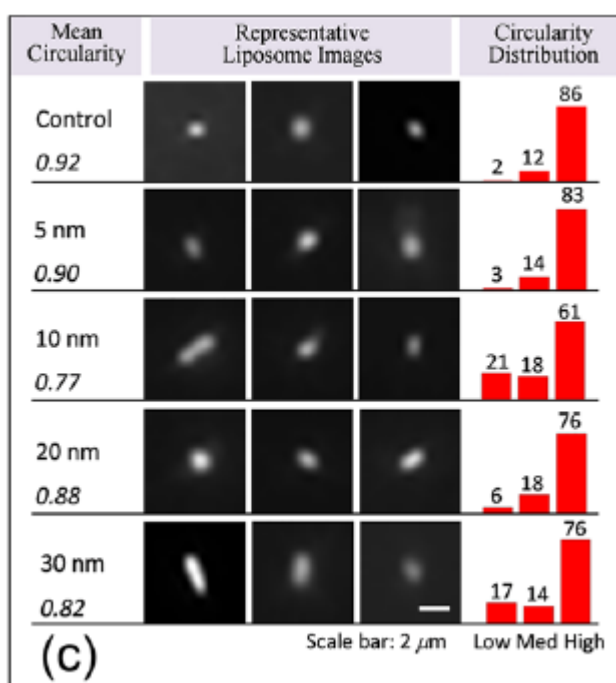
Fig. 2.4 Fluorescence images of liposomes influenced by AuNP at various sizes (center), circularity's mean values (left), and histograms of percent populations (right).

Membrane pore development is a secondary result of AuNPs adsorption, which is caused by the lateral pressure created by AuNPs adsorption [78]. Fig. 2.5 shows the mechanism of pore formation. The head groups of lipid and charged AuNPs exert electrostatic forces that cause molecules of the liposome to pack closely around the binding sites, generating raft-like domains (Fig. 2.5b). The dipole-charge interaction with an AuNPs with a citrate cap causes the DMPC molecule head groups to shift from a leaning to a stand-up state (Fig. 2.5c). Potential top view of the arrangement of the

lipid head groups in a pore created by several AuNPs adsorption (Fig. 2.5d), here the ordered domains (shown in a dark tint) are disturbed areas with AuNPs positioned on top that have been removed for viewing convenience.
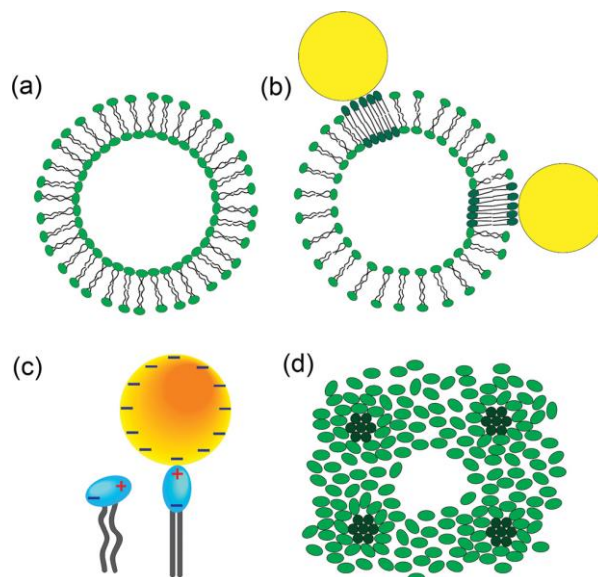
Fig. 2.5 Illustration of the mechanism of pore formation in lipid bilayer by NPs. Lipid head groups (a) and charged AuNPs exert electrostatic forces that cause molecules of the liposome to pack closely around the binding sites, generating raft-like domains (b). (c) The dipole-charge interaction with AuNPs with a citrate cap causes the head group of a DMPC molecule to shift from a leaning to a stand-up state. (d) Potential top view of the arrangement of the lipid head groups in a pore created by several AuNPs adsorptions.

These investigations concluded that NPs modify the hardness of lipid membranes: lipids at detention sites are toughen by adsorption of AuNPs, whilst lipids further away are fluidized. Negatively charged AuNPs can interacts zwitterionic membranes and generate nano-sized pores in the lipid bilayers due to fluidization, which raises the liposome surface area and changes the structure of the membrane.

Laurencin *et al*. investigated the interactions between GUVs and charged core-shell magnetic nanoparticles (CSMNs) [61]. They are attempting to create a simpler approach for examining interaction between the cell membranes and NPs. They synthesized GUVs in MOPS (3-(N-Morpholino)-propanesulfonic acid) buffer (1 mM buffer in pH 7.4) using neutral DOPC, negatively charged DOPG, and positively charged DOTAP (1,2-dioleoyl-3-trimethylammonium propane) lipid by the 'electro

formation method' [79]. Fluorescent dye was 1,2-dioleoyl-sn-glycero- 3-phosphoethanolamine-N-(lissamine rhodamine B sulfonyl) (Rh-DOPE). They concentrated on charged functionalized CSMNs with cationic or anionic properties, with a diameter of 35 nm [80-85]. They used three different types of microscopes in their experiment: optical, electron, and confocal.

When DOPG/DOPC-GUVs were introduced to a liquid mixture of fluorescent cationic FITC-PEG-amine CSMNs, a uniform distribution of fluorescent dye is observed at the membranes of GUVs. The red fluorescence of Rh-DOPE indicates only membrane (Fig. 2.6a), while the green fluorescence indicate the incorporation of NPs in membranes (Fig. 2.6b). The overlapping of Fig. 2.6(a) and (b) is shown in Fig. 2.6(c), indicating yellow in the confocal microscopic image. The two fluorescence peaks are observed in the line profile in Fig. 2.6(d). Because of the interaction between cationic CSMNs and anionic GUVs, hybrid giant vesicles were formed with a tightly packed layer of CSMNs and no visible vesicle rupture.
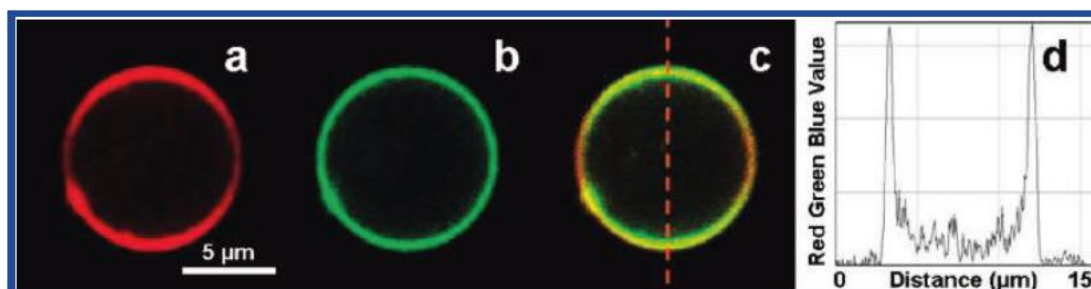
Fig. 2.6 Confocal micrographs of negatively charged GUVs covered with cationic CSMNs. (a) Rh-DOPE-induced red fluorescence of the membrane. (b) Cationic CSMNs adsorbed on the membrane-induced green fluorescence. (c) Combined images of (a) and (b). (d) Plot profile matching the dotted orange line on (c).

Yu *et al.* investigated the pearling of GUVs induced by cationic aliphatic amine NPs [62]. They studied how to get phospholipid vesicles to convert from their regular spherical structure into pearls and pearl necklaces that last for hours. They used the 'gentle hydration approach' [86] to generate GUVs in this work. They used a mixture of DOPC and the fluorescent lipid 1,2-dioleoyl-*sn*glycero-3-phosphoethanolamine-*N*-(lissamine rhodamine B sulfonyl) (DOPE-RhB) in choloroform/methanol (2/1 by volume). A thin lipid layer was created at the bottom of a flask by dehydrating the lipid

mixture and hydrated with 0.10 M sucrose enclosing a specific quantity of aliphatic amine NPs (usual diameter 200 nm, surface charge 40 Å^2/charge group (Invitrogen Inc.)) overnight at 40 °C. Cationic NPs with diameters of 40 and 100 nm were used to corroborate the universality of these findings. GUV has a circular form in the absence of NPs (Fig. 2.7A). Tubular protrusions emerge when 0.01 nM cationic NPs are enclosed inside GUVs (Fig. 2.7B). Fig. 2.7(C-G) depicts the dynamic alteration of a distinct GUV during the course of 12 minutes. There are two stages: first, tubes erupting and expanding from the parent sphere; second, the disintegration of the parent sphere into pearls. The pearls seemed to grow in a consistent pattern.
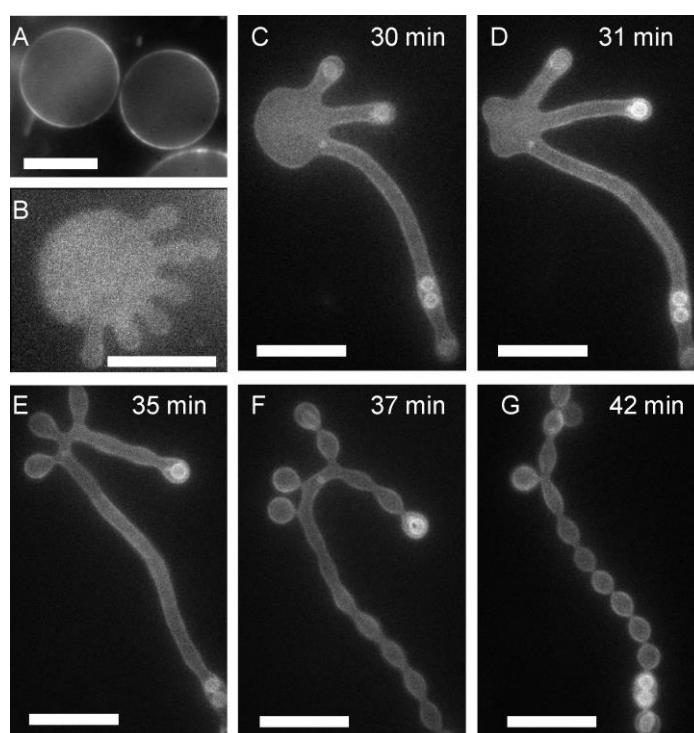
Fig. 2.7 Shape changes of DOPC GUVs. (A) The GUV form is spherical in the absence of NPs. (B) Tubular protrusions develop in the presence of 0.01 nM cationic NPs. The dynamic process is depicted over the course of 12 minutes as seen in the panels (C-G). After the NPs that were outside of the GUVs were taken out, time passed. The end result, a necklace made of uniformly sized ellipsoidal pearls, stays stable for hours. Scale bar is 20 μm.

The pearl necklace developed in the early phases at a greater (1 nM) NPs density, and after 20 min, they converted into distinct, uniform-sized round pearls that nevertheless formed a chain. The size variation of 100 unconnected GUVs with 10 nM enclosed NPs density and 50 GUVs with no NPs. The higher the NPs concentration, the smaller the vesicles became, by a factor of two. The physical explanation is most likely a mismatch

of surface area between the external and internal surfaces of the bilayer caused by cationic NPs adsorption, which raises the head group area of zwitterionic lipids [87, 47]. The mismatch causes spontaneously bending, which is increased by electrostatic attraction between charged NPs, stiffening the membrane and causing wrinkling, which leads to the apparent spherical structure variation.

Wang *et al.* investigated the NPs-induced surface reconstruction of PC membranes [47]. They used uncharged DOPC, DLPC, and DPPC lipids and followed 'extrusion method' [88] for LUV synthesize at 1 vol% density in PBS buffer (10 mM; pH, 6.0). DOPC and DLPC are normally in fluid phase and DPPC is normally in gel phase. They employed NPs made from carboxyl-modified (- 0.91 e^-/nm^2) and amidine-modified (+ 0.25 e^+/nm^2) white polystyrene (PS) latex with size of 20 nm; as well as, silicon dioxide NPs (~ 0.11 e^-/nm^2) and supercoiled plasmids in control experiments. They performed Fluorescence Correlation Spectroscopy (FCS) [89], Forster Resonance Energy Transfer (FRET) [90] and Isothermal Titration Calorimetry (ITC) experiments [91].

When anionic NPs were interacted with DLPC liposomes containing Laurdan [92], the raw fluorescence data is shown in Fig. 2.8(A). Fluorescence intensity was plotted in opposite to the wavelength, and they noticed that as NPs concentration grew, blue emission increased and red emission decreased. This suggested that the fluid–gel phase coexists in such a way that the volume of fluid to gel stage fluctuates. The logarithmic standardized emission is displayed opposite time on the nanosecond time scale in Fig. 2.8(B). They chose NBD and Rhodamine B (RhB) because NBD-labeled phospholipids are acquainted to divide into the gel stage of lipid membranes, but RhB-labeled phospholipids do not [93]. After NPs binding, the donor mean lifetime increases from 4.6 to 5.2 ns, while the FRET efficiency, as measured by forever, reduces from 0.65 $\pm$ 0.06 to 0.45 $\pm$ 0.05 ns. After introducing NPs, the lifetime of NBD rose as expected, indicating that it had partitioned into the gel stage. Prior investigations on microscopic phase split using two chemically distinct lipid ingredients [94] predicted a magnitude of decrease in this range, validating the hypothesis of local phase transition. They observed non-specific adhesion of charged NPs onto phospholipid bilayers with a single element containing PC head groups in fluorescence and calorimetry studies, resulting in reproduction of the surface at the NPs adsorption spots [94, 87]. Positively charged NPs

cause otherwise gel membranes to fluidize, while negatively charged NPs cause local gelation in otherwise fluid bilayers.
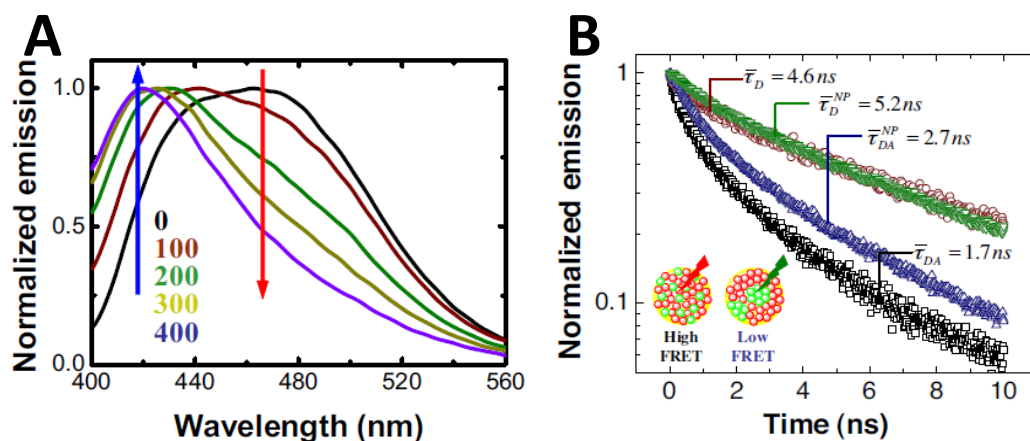
Fig. 2.8 (A) Normalized emission after anionic (carboxyl-modified) NPs bind to 200 nm DLPC vesicles is shown against wavelength. The number ratio of particles to vesicles $C_{NP}/C_L = 0, 100, 200, 300,$ and 400 for the number ratio of particles to liposomes. (B) Fluorescence emission plotted against time for FRET studies using 200 nm DOPC vesicles after anionic (carboxyl-modified) NPs were added at $C_{NP}/C_L = 200$.

Roiter *et al.* studied the interaction of NPs with lipid membrane [95]. They used AFM (Atomic force microscopy) to explore the interaction of lipid bilayers made from DMPC with nanostructured silica surfaces [96, 97], and by covering glossy silicon chips with silica NPs with diameters varying from 1 to 140 nm, nano-structured surfaces were created. Taking into account their electrostatic charge, hydrophobicity, and size, NPs can interact with lipid bilayers in three different ways, as shown in Fig. 2.9. The lipid bilayer creates pores by NPs with sizes bigger than 1.2 nm and less than 22 nm, as observed in Fig. 2.9(a, b). At the same time, NPs on a surface or other surface characteristics less than 1.2 nm in diameter do not break the lipid membrane, and it passes over them (Fig. 2.9c). Big NPs with width more than 22 nm are encased in a lipid bilayer (Fig. 2.9d), unless the particle's surface is rough, in which case the lipid bilayer covering of spherical particles is insufficient (Fig. 2.9e).
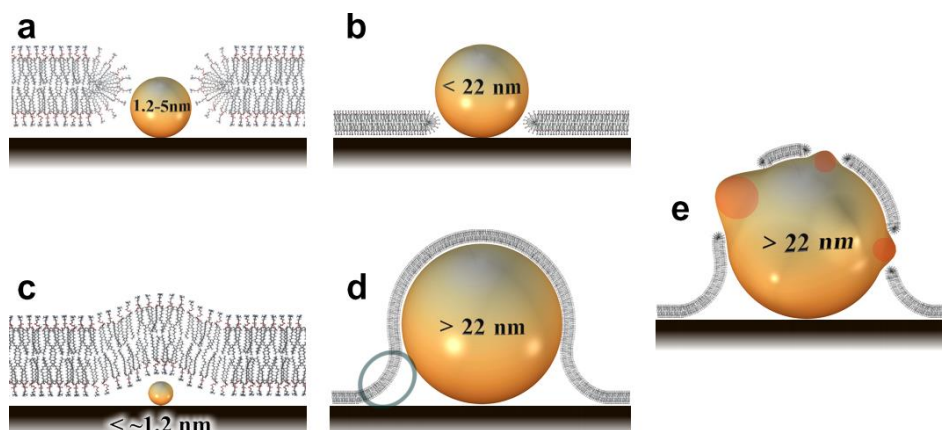
Fig. 2.9 Illustration of the mechanism of pore formation in a lipid bilayer induced by different sizes of NPs, (a) the lipid bilayer creates pores by NPs of sizes larger than 1.2 nm and smaller than 22 nm (b). (c) NPs less than 1.2 nm in diameter do not break the lipid membrane, and it passes over them. (d) NPs of sizes higher than 22 nm are encased by lipid bilayer. (e) Due to the surface roughness, more than 22 nm sizes NPs may not be completely covered.

One of the most crucial characteristics of lipid membranes is the bending modulus, which is crucial for many biological activities as exo- and endocytosis, vesicle fusion, and the control of membrane protein activity. The bending modulus expresses a material propensity to withstand bending. It is the energy needed to deform the bilayer from its inherent curvature to another curvature. The biological processes such as membrane fusion [98] and endocytosis [99] are occurred due to bending modulus.

Karal *et al.* investigated the influences of cholesterol on the vesicle's size distribution and the bilayer bending rigidity [58]. Three different membranes such as DOPC/chol, DOPG/DOPC/chol, POPC (1,2-dipalmitoleoyl-*sn*-glycero-3-phosphocholine)/chol were used. The values of bending modulus for DOPC/chol (100/0), DOPC/chol (85/15), DOPC/chol(71/29), and DOPC/chol (60/40)-GUVs were 18.0 ± 0.9, 23.5 ± 0.3 28.1 ± 0.3, and 31.2 ± 0.3 $k_{B}T$, respectively. Regarding charged membranes, the values of bending modulus for DOPG/DOPC/chol (70/30/0), DOPG/DOPC/chol (46/39/15), DOPG/DOPC/chol (43/28/29), and DOPG/DOPC/chol(40/20/40)-GUVs were 25.9 ± 0.5, 26.9 ± 0.3, 32.1 ± 0.4, and 37.5 ± 0.6 $k_{B}T$, respectively. For the case of POPC/chol (100/0), POPC/chol (85/15), POPC/chol (71/29), and POPC/chol (60/40)-GUVs, the values of bending modulus were 18.5 ± 0.6, 23.3 ± 0.8, 28.2 ± 0.6, and 31.1 ± 0.5 $k_{B}T$,

respectively. In all cases of membranes, with an increase in membrane cholesterol concentration, the bending modulus increases.

Eid *et al.* investigated the bending rigidity of membranes by means of buckling simulations [37], where they used membrane buckling method [100, 101]. In addition, they investigated the relationship between simulation results and system size and strain [102], and discovered that whenever the number of nodes exceeded a specific limit, the box's sizes had very little effect upon the findings. The apparent elastic modulus of phase-separated mixtures was also nearer to the milder element's value. These estimates of the folding elasticity are based on a direct relation among the area compressibility modulus and the bending modulus [103]. Fig. 2.10(A) demonstrates the membrane bend in a sample chamber that is rectangular and has sides that are L_x, L_y, and L_z long. Fig. 2.10(B) demonstrates the diameters of 20 nm, bending modulus estimates are reliable and higher, but considerable discrepancies are found for tiny components ($L_z = 18$ and 15 nm). Fig. 2.10(C) demonstrates that the computed folding elasticity values grew as system size shrank.
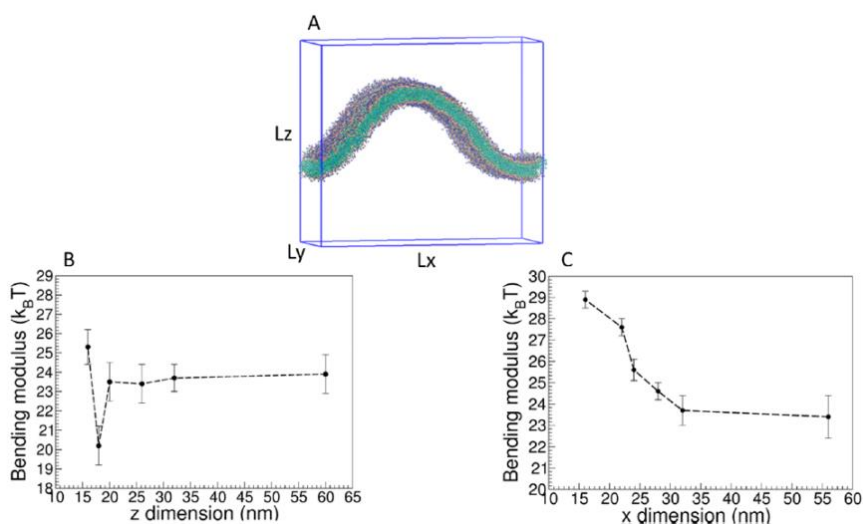
Fig. 2.10 (A) Simulation of a membrane buckle with side lengths L_x, L_y, and L_z. (B) Calculation of the DOPC lipid membrane's bending modulus based on simulations of varying sizes in the z-dimension. (C) Calculation of the DOPC lipid membrane's bending modulus based on simulations of varying sizes in the x-dimension.

Chakraborty *et al*. investigated how cholesterol stiffens unsaturated lipid bilayers [57]. They reported that cholesterol makes DOPC membranes more stiff when bend, same to saturated membranes, by raising the bilayer's packing consistency, with an extensive approach that included neutron spin-echo (NSE) spectroscopy [104], solid-state deuterium NMR (^{2}H NMR) spectroscopy [105], and molecular dynamics (MD) simulations [106]. LUVs were used for NSE, multilamellar vesicles for ESR, and multilamellar stacks for ^{2}H NMR investigations in their study. Fig. 2.11(A) shows that the dynamic structural factor, q, declines more gradually for DOPC/Chol membranes than for DOPC membranes at all wave vectors, and Fig. 2.11(B) shows that bending rigidity modulus increases with increasing cholesterol concentration.
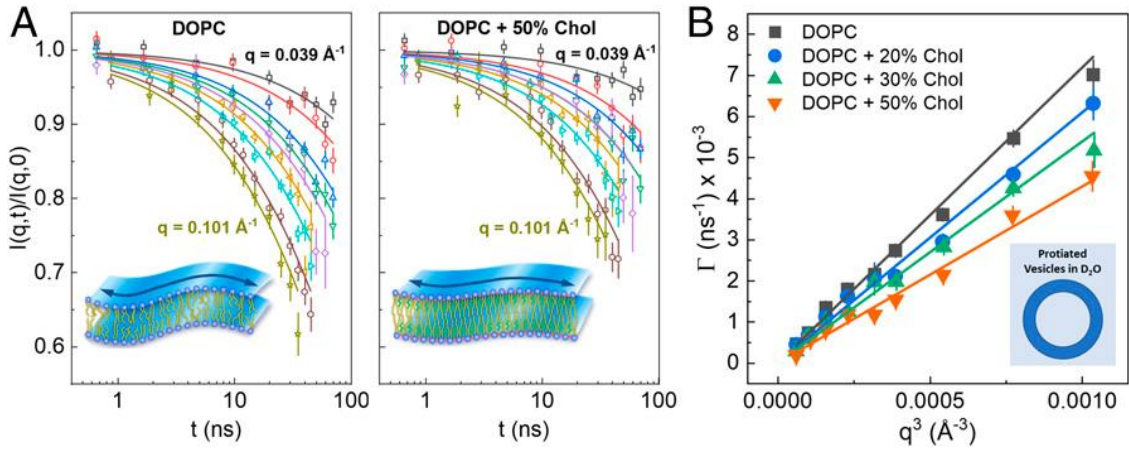
Fig. 2.11 (A) Dynamics in DOPC/chol membranes clearly slow down as evidenced by the intermediate scattering functions (I(q,t)/I(q,0)) of DOPC bilayers without cholesterol (Left) and 50 mol% cholesterol (Right). (B) DOPC/chol vesicles decay rates in D$_2$O are q-dependent (Inset). The increasing trend of bending modulus is shown by a reduction in the slope of solid lines with increasing cholesterol content.

They used a stretched-exponential function to characterize the NSE dynamic structural factor:

$$\Gamma_{\text{bend}}(q) = 0.0069 \frac{k_B T}{\eta_{sol}} \sqrt{\frac{k_B T}{\kappa}} \, q^3 \tag{2.3}$$

Here $\Gamma_{\text{bend}}(q)$ is the decay rate of the folding variations, $k_B T$ is the thermal energy, η_{sol} is the solvent's (i.e., D$_2$O or ^{2}H$_2$O) viscosity, q is the wave vector transfer, κ is the effective bending rigidity modulus.

The relative bending rigidity moduli (k/k_0) are plotted against cholesterol concentration (mol%) in Fig. 2.12(A), and the bending rigidity moduli increase with increasing cholesterol concentration in every experiment using NSE spectroscopy, ^{2}H NMR spectroscopy, and MD simulation. In Fig. 2.12(B), relative bending rigidity moduli (k/k_0) are plotted against area per lipid (Å^2), and we can see that bending rigidity moduli decrease with increasing area per lipid in both experiments, implying that membrane lipids are packed more tightly. Enhanced molecular stacking and membrane thickness characterize these alterations [107]. Cholesterol affects unsaturated DOPC membranes via a lipid- stacking process same to that observed in saturated lipid membranes [54], as evidenced by the synergistic alterations in structural and dynamical membrane properties.
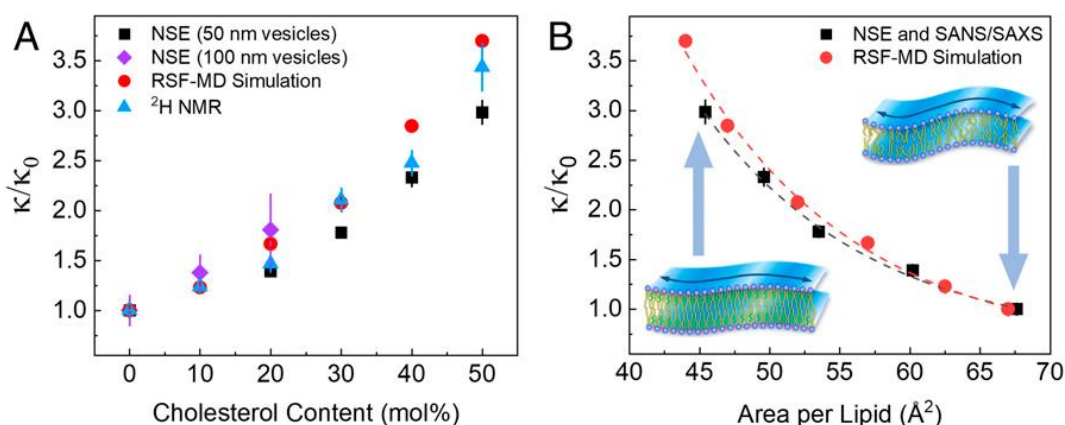
Fig. 2.12 The bending rigidity moduli (κ/κ_0) of DOPC membranes increases roughly identically with raising cholesterol (A) and decreases with increasing area per lipid (B). The dashed lines serve as a visual aid.

Pan *et al.* investigated the cholesterol effect on the structural and mechanical aspects of lipid membranes, which depends on the chain saturation of lipids [54]. The impacts of cholesterol on bending modulus of membranes (K_C), thickness of membrane (D_{HH}), incomplete and visible regions of cholesterol and lipid, and the rank variable (S_{xray}) are all dependent on the number of saturated hydrocarbon chain in a lipid molecule, according to this research. They also found that up to 40% cholesterol has no effect on the K_C of membranes made up of phosphatidylcholine lipids using two cis monounsaturated chains, but has the predicted rigidifying impact on membranes made up of two saturated chains. For the production of unilamellar vesicles, they employed

DOPC, SOPC, DMPC, DPPC, and diC22:1PC lipids [108]. K_C for DMPC grows fast as cholesterol concentration c raises, and by $c = 0.3$, however, it is over than four times bigger than at $c = 0$. They could only get K_C up to $c = 0.3$ for DMPC in this experiment because raising K_C reduces the strength of the diffused dispersion necessary for this approach. K_C increases in SOPC, but not as substantially as in DMPC, and it plateaus above $c = 0.3$. The outcomes of SOPC are equivalent to those of POPC, which has a saturated sn-1 chain with two less carbons [109]. SOPC/cholesterol [110] and POPC/ergosterol [109] likewise showed a K_C leveling off. Their more interesting finding is that the K_C for c up to 0.4 in both DOPC and diC22:1PC is practically uniform.
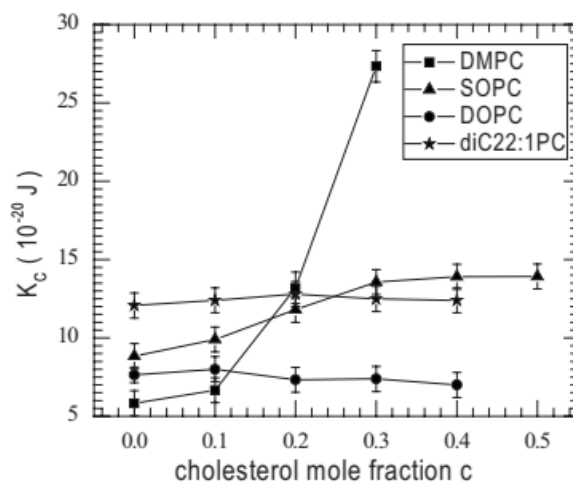
Fig. 2.13 Cholesterol-dependent bending modulus of four different lipid bilayers

They highlighted that the fundamental phenomenological explanation is that cholesterol's impact on K_C rises considerably with the amount of saturated chains, whereas cholesterol has no effect on K_C in DOPC [111]. The polymer brush theory [103] was used to calculate the area compressibility modulus K_A by,

$$K_C = K_A (2D_C)^2/24 \qquad (2.4)$$

These K_C findings support the elastic moduli at the higher cholesterol range and call into question the utility of universal ideas. Though the majority of the outcomes were collected at 30 °C, extra data obtained at various temperatures to permit for a decreased temperature component does not indicate consistency for cholesterol's influence on every lipid bilayers.

2.2 Biomembranes

Biomembranes are a thin biological covering that surrounds and isolates the living cell from its environment. Its thickness is 4 nm. Biomembranes are mostly a lipid bilayer that allows only very tiny molecules like as water, oxygen, and carbon dioxide, as well as polar compounds of hydrophobic molecules (e.g. DNA, RNA, carbohydrates, amino acids and ions), to pass through. Ion pumps and exchangers control the transmembrane movement of ions like as Na^+, K^+, Ca^+, and Cl^-. The cell can create chemical and electrical gradients thanks to these. To promote the membrane potential of a cell, the chemical gradients of Na^+ and K^+ is maintained across the membranes under physiological conditions, which is important for many cellular functions. The Ca^{2+} signaling system regulates the majority of cellular activities, and the content of free Ca^{2+} in the cytoplasm is strongly regulated. The concentration of free Ca^{2+} inside the cell is kept very low (0.10 M), whereas the outside concentration of the cell is multifold larger (1.30 M). The high levels of intercellular ATP stimulate several active ports, which help to sustain the gradients along with the energy-dependent cellular processes that are necessary for cell integrity.
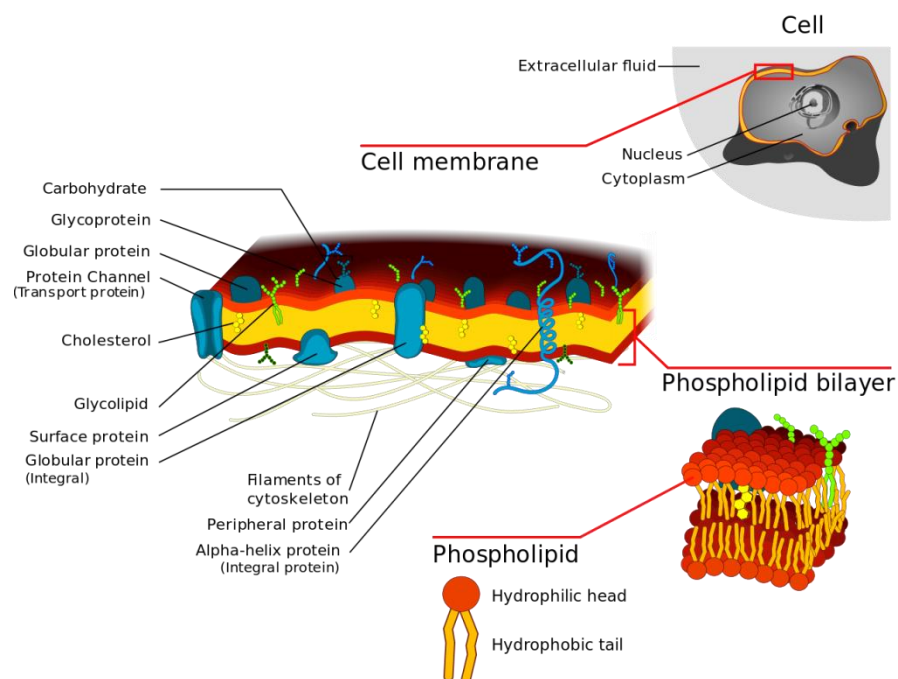
Fig. 2.14 An extensive illustration of cell membrane [112]

2.3 Lipid Bilayer

Lipids are organic compounds that are non-polar in nature and are soluble only in non-polar solvents and insoluble in water. The most prevalent element is lipid of all types of biological membranes [113]. A lipid molecule contains a hydrophilic head and a hydrophobic tail. The fatty acid tails extend inward to produce a compact hydrophobic core zone, while the hydrophilic glycerol moieties of the lipid molecules stay in contact with water [114]. Fig. 2.15 shows the schematic illustrations of a lipid molecule (bottom right).

A lipid bilayer (phospholipid bilayer) is made up of two layers of lipid molecules. They are flat sheets of membranes that surround all cells and form a continuous barrier. The lipid tail made up of two fatty acid chains make up these bilayers. Other than phospholipids, biological membranes often contain a variety of substances. Cholesterol is an important example in animal cells since it serves to reinforce the bilayer and reduce its permeability. Cholesterol also aids in the regulation of the function of several membrane proteins. Ions can't pass through bilayers therefore cells use proteins called ion pumps to transfer ions across their membranes, allowing them to adjust salt concentrations and pH. Phospholipid bilayers are a molecular system with aligned molecular systems that have remarkable thermal, optical, and electrical properties [115-119]. Phospholipids are an extremely desirable soft material due to their antifouling, self-healing, and distinctive optical features of lipid bilayers [115]. Fig.2.15 shows schematic diagram of lipid bilayer.
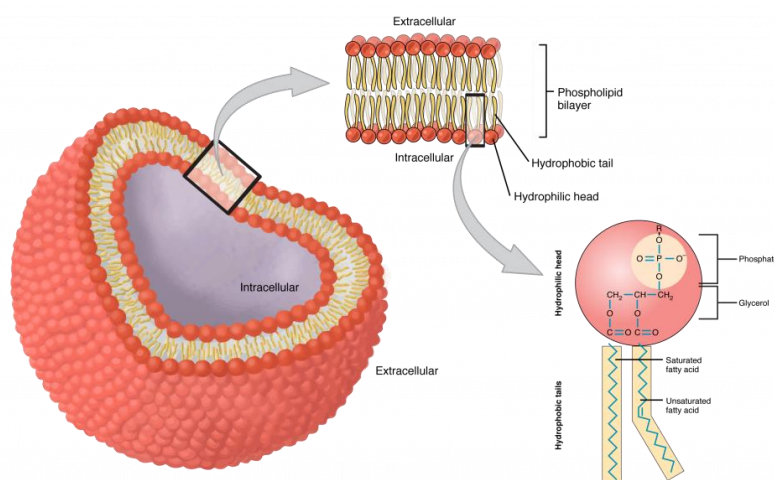
Fig. 2.15 Schematic diagram of lipid and lipid bilayer [120]

2.4 Vesicles and Its Classification

Vesicles are a synthesized spherical chamber containing aqueous solution inside and surrounded by a lipid bilayer [121]. Vesicles are used as a mimic of cells [122]. On the basis of structure, vesicles are mainly four types; one is unilamellar and another is multilamellar. Unilamellar vesicles **(ULVs)** contain only one lipid bilayer. Multilamellar vesicles **(MLVs)** contain more than one lipid bilayers as like as onion. Multivesicular vesicles **(MVVs)** contain more than one vesicle as like as rambai. Oligolamellar vesicles **(OLVs)** contain concentric lamellae (ranging between two to five). On the basis of size, Unilamellar vesicles are three types: (i) Small Unilamellar Vesicles (SUVs) which size range of 20-100 nm (ii) Large Unilamellar Vesicles (LUVs) which size range of 100-1000 nm, and (iii) Giant Unilamellar Vesicles (GUVs) which size range of 1-200 μm. Fig. 2.16 shows the different classes of vesicles. GUVs are employed as a model for biological membranes in research [123]. Typically, the diameters of animal and plant cells are 10–30 μm and 10–100 μm, respectively. Even mitochondrial cell organelles are typically 1-2 μm in length. As a result, the size of the specimen being researched should be taken into account while choosing a model membrane.

(i) Unilamellar vesicles

SUV   LUV   GUV

< 100 nm

100-1000 nm

> 1 μm

(ii) Multilamellar vesicles   **(iii) Multivesicular vesicles**

> 100 nm   > 1 μm
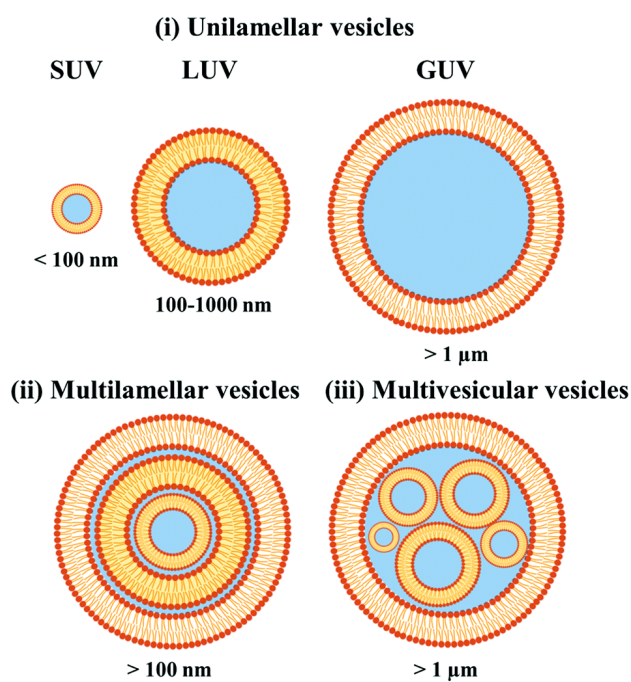
Fig. 2.16 Illustration of different classes of vesicles [124]

2.5 Cholesterol

Cholesterol is a waxy and fat-like material found across every cell of the human body including blood plasma [125]. It is a sterol [126], which means that cholesterol is a combination of steroid and alcohol. The chemical formula of cholesterol is $C_{27}H_{46}O$ and molecular weight is 386.65 g/mol. Cholesterol is insoluble in water, although it is soluble in alcohol and ether and chloroform to a lesser extent. Cholesterol contributes for over 30% of the membranes in all animal cells. It plays a crucial role in the development of membranes as well as the control of membrane fluidity across a broad range of physiological temperatures. The hydroxyl group of cholesterol interacts with water molecules surrounding the lipid membrane, as do the polar heads of membrane phospholipids and sphingolipids. Animal cells do not need to produce cell walls because cholesterol increases membrane packing by interacting with phospholipid fatty-acid chains, altering membrane fluidity [127], and maintaining membrane integrity (like plants and most bacteria). Animals can move because of the membrane is stable and strong without being stiff, allowing animal cells to change shape. In Fig. 2.17, an illustration is provided to highlight how cholesterol combines with the cell membranes.
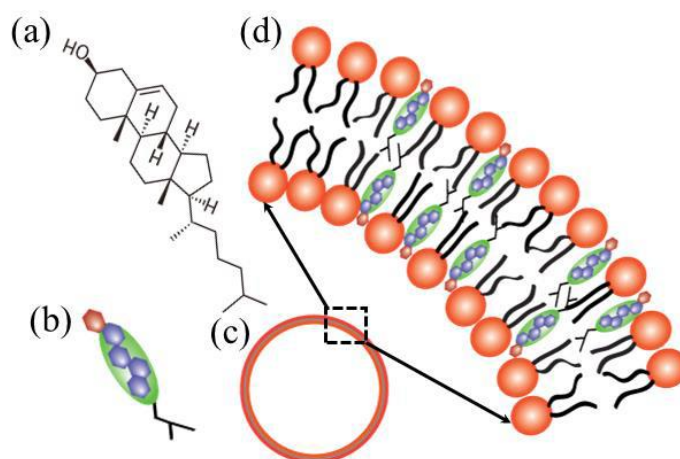
Fig. 2.17 (a) Cholesterol structure, (b) Cholesterol depiction, (c) GUV lipid membrane, and (d) Cholesterol-rich lipid membrane [58].

Fats are complicated combinations of triglycerides with minor amounts of PC lipids and cholesterol molecules, which are used to make all animal and human cell membranes. Because cholesterol is produced by all animal cells, it can be found in various amounts in all animal-based meals. Cheese, egg yolks, beef, pork, chicken, fish, and shrimp are

all good sources of cholesterol. Human breast milk contains a large amount of cholesterol as well. Dietary cholesterol consumption, on the other hand, has a poor correlation with blood plasma cholesterol levels. Although there is a link between saturated fat consumption and cholesterol levels, the majority of cholesterol in the blood comes from endogenous sources (i.e. produced by the liver).

2.5.1 Classification of cholesterol

Lipoproteins inside the bloodstream transport cholesterol all through the body. The brief description of cholesterol is given below:

Low-density lipoprotein (LDL): LDL is often called "the bad cholesterol". LDL particles are the primary transporters of cholesterol in the bloodstream. The optimal range of LDL cholesterol is <130 mg/dL.

High-density lipoprotein (HDL): HDL is often called "the good cholesterol". In a mechanism known as reverse cholesterol transport, HDL particles are considered to transfer cholesterol back to the liver, for excretion or for use by other hormone-producing organs [128]. Low quantities of HDL particles are linked to atheromatous illness, whereas high numbers of HDL particles are linked to improved health outcomes [129]. The optimal range of HDL cholesterol is >60 mg/dL.

Very low-density lipoprotein (VLDL)

The liver makes VLDL molecules from triacylglycerol and cholesterol that aren't employed in the formation of bile acids. The optimal range of VLDL cholesterol is <150 mg/dL.

2.5.2 Advantages and disadvantages of cholesterol

Body requires cholesterol to produce hormones, vitamin D, and digestive fluids. Cholesterol also aids in the correct functioning of the organs. Having too much LDL cholesterol, on the other hand, can be a problem. Over time, high LDL cholesterol can cause artery damage, contribute to heart disease, and raise the risk of stroke.

2.6 Nanoparticles

Nanoparticles (NPs) are small particles of size from 1 to 100 nm. The layer between surfaces is a crucial component of nanoscale matter, as it influences all of its properties.

Inorganic NPs and organic NPs are two different forms of NPs. Metal and metal oxides, which are powerful antibacterial agents, are among the inorganic NPs. Inorganic NPs include metal oxide NPs such as Ag, Fe_3O_4, TiO_2, CuO, and ZnO. At high temperatures, organic NPs are often less stable. As a result, inorganic NPs are more commonly used as antibacterial polymers [130]. Modern high-tech materials require metal NPs with controlled facet, size, and shape [131]. Metal oxide-based NPs are synthesized to alter the properties of their respective metal-based NPs. For example, iron (Fe) NPs instantly oxidizes to iron oxide (Fe_2O_3) in the presence of oxygen at room temperature.

2.6.1 Magnetite nanoparticles

Magnetite (Fe_3O_4) is a ferromagnetic black mineral that contains both Fe (II) and Fe (III). XRD is used to obtain the crystal structures. With iron cations occupying interstitial regions and O^{2-} ions creating a face-centered cubic lattice, the structure is inverse spinel. Half of the Fe^{3+} cations occupy the tetrahedral sites, while the other half, together with Fe^{2+} cations, occupies the octahedral sites. The formation of magnetite, which is composed of iron, both ferrous and ferric, necessitates settings with intermediate amounts of oxygen availability [132], increasing their reactivity compared to iron nanoparticles. The improved reactivity and efficiency of metal oxide NPs are the fundamental reasons for their creation [133]. Fig. 2.18 shows the crystal structure of Fe_3O_4 NPs.
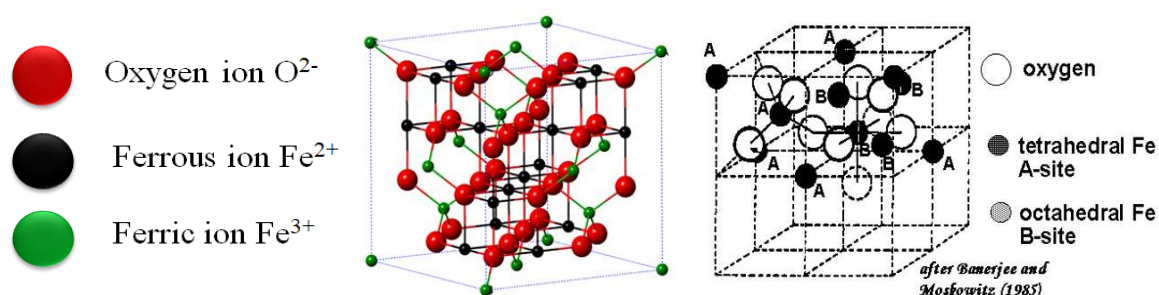
Fig. 2.18 Crystal structure of Fe_3O_4 NPs [134]

2.7 Adverse Effects of Magnetite NPs

Iron impurities in burning fuels like diesel as well as interior sources like printer toners and leaking stoves are some typical sources of magnetite NPs. Human brain contains large amounts of magnetite NPs, which are common in urban areas. Such magnetite NPs can go straight to the brain via the olfactory nerve and build-up of reactive oxygen species in cells. Enhanced reactive oxygen species production links to neurodegenerative diseases (e.g., Alzheimer's) [28]. It was also found magnetite NPs in amyloid plaques (aggregates of misfolded proteins) [29]. Such proteins are responsible for causing Alzheimer's disease. One of the main reasons of substantial mortality and morbidity in cardiorespiratory illnesses is the emission of NPs into the environment from numerous sources [19, 20]. Medical implants are one way through which NPs can get into human body, magnetic resonance imaging contrast agents, insecticides, and food processing [21–23]. Due to their small size, NPs can easily diffuse in air and inhaled [24]. Syntheses NPs may get inside of body through six main routes: inhalation, intraperitoneal, intravenous, subcutaneous, dermal, and oral. Once within the body, the NPs engage in interactions with biological elements like proteins and cells before being absorbed [15-17]. Environmental NPs are easily inhaled into the body and interact with blood cells, causing discomfort in the cardiovascular and pulmonary systems [28].

CHAPTER 3

MATERIALS AND METHODS

3.1 Chemical and Reagents

For the synthesis of GUVs and magnetite NPs, several kinds of lipids, cholesterol, chemicals, and reagents were used. Lipids were purchased from Avanti Polar Lipids Inc. (Alabaster, AL). The cholesterol, chemicals, and reagents were purchased from Sigma-Aldrich (Germany).

The compounds that we used in our investigations are as follows:

Lipids, Cholesterol, Glucose, Sucrose, Sodium chloride, Sodium hydroxide, Piperazine-1, 4-bis (2-ethanesulfonic acid) (PIPES), Ethylene glycol-bis (2-aninoethylether)-*N,N,N´N´*-tertraacetic acid (EGTA), Bovine serum albumin (BSA), Chloroform

3.1.1 Lipids

The following two lipids were used to prepare the membranes of GUVs.

1) 1,2- dioleoyl-*sn*-glycero-3-phosphocholine (DOPC)
2) 1,2-dioleoyl-*sn*-glycero-3-phospho-(1´-*rac*-glycerol) (DOPG)

1) 1,2- dioleoyl-*sn*-glycero-3-phosphocholine

DOPC is a phosphatidylcholine (PC) with both oleoyl phosphatidyl acyl groups at positions 1 and 2. In animal cell membranes, PC is the most prevalent lipid. DOPC dissolves in chloroform. The molecular formula of DOPC is $C_{44}H_{84}NOP_8$, and the molecular weight is 786.113 g/mol. The chemical structure of DOPC is shown in Fig. 3.1.
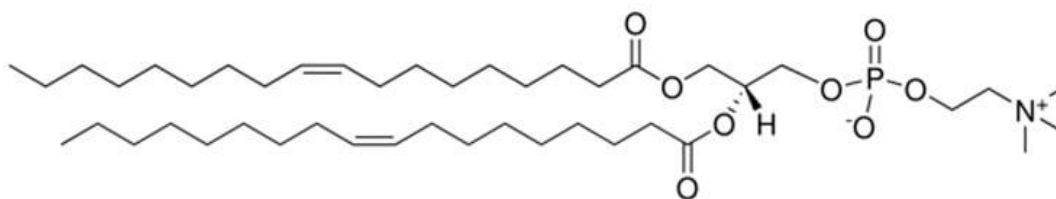
Fig. 3.1 Chemical structure of DOPC lipid [135]

2) 1,2-dioleoyl-*sn*-glycero-3-phospho-(1´-*rac*-glycerol)

DOPG is a Phosphatidylglycerol with an L-glycerol 3-phosphate backbone and either saturated or unsaturated fatty acids ester-bonded to its carbons 1 and 2. It is found in large concentrations in all cell membranes and in low concentrations in fat reserves. DOPG's head group contains two hydroxyl groups. A phosphomonoester is used to bind the head group substituent glycerol. DOPG is a lipid with an anionic charge. DOPG dissolves in chloroform. $C_{42}H_{79}O_{10}P$ and 797.026 g/mol are the chemical formula and molecular weight, respectively. The structure of DOPG is depicted in Fig. 3.2.
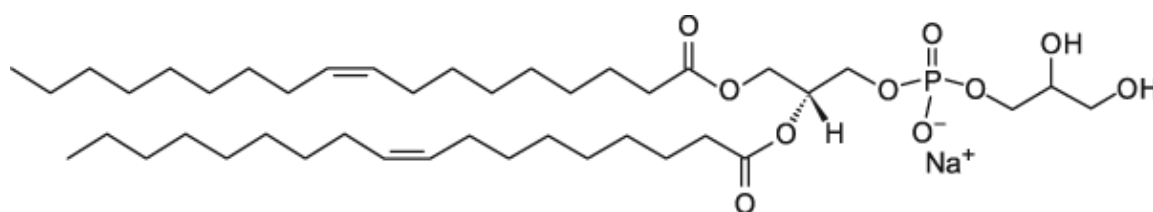
Fig. 3.2 Chemical structure of DOPG lipid [136]

3.1.2 Cholesterol

Cholesterol is a natural substance. It is a sterol, which is a lipid. It is a biosynthetic element of membranes of mammalian cells and is created biochemically by all mammalian cells. It's a crystalline yellowish substance. Cholesterol is insoluble in water, although it is soluble to a lesser extent in alcohol, ether, and chloroform. $C_{27}H_{46}O$ and 386.65 g/mol are the chemical formula and molecular weight, respectively. The boiling and melting points are respectively 148.5 °C and 360 °C. Triglyceride was employed in this study. Fig. 3.3 depicts the chemical structure of cholesterol.
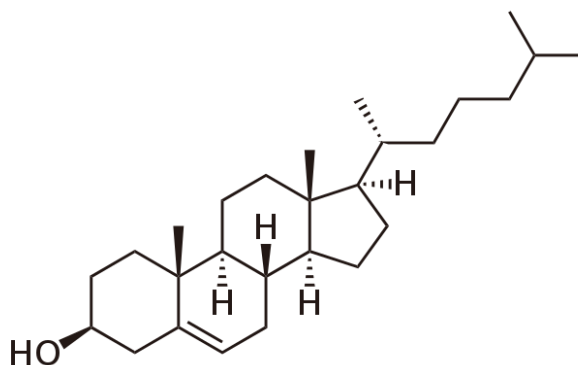
Fig. 3.3 Chemical structure of cholesterol [137]

3.1.3 Calcein

Calcein, often referred to as fluorescein complex, is an orange-colored fluorescent dye having excitation and emission wavelengths of 495 and 515 nm, respectively. Calcein is frequently employed as an indication of lipid vesicle leakage because it self-quenches at concentrations above 70 mM. It is also traditionally employed as a complexometric indicator for the fluorometric determination of calcium as well as for the titration of calcium ions. The chemical formula of calcein is $C_{30}H_{26}N_2O_{13}$ and molecular weight is 622.53 g/mol. Fig. 3.4 depicts the chemical structure of calcein.
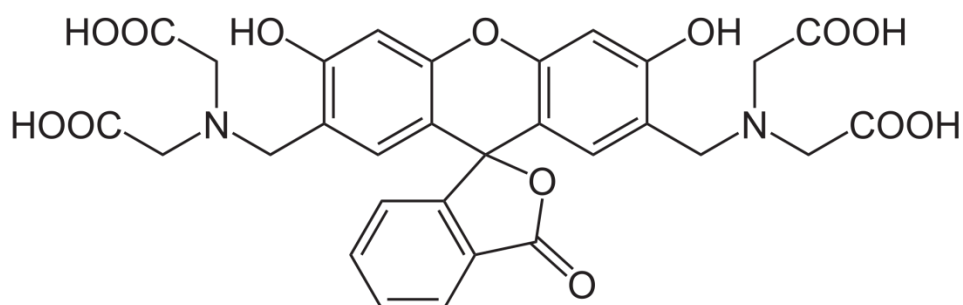
Fig. 3.4 Chemical structure of cholesterol [138]

The non-fluorescent acetomethoxy derivate of calcein (calcein AM, AM = acetoxymethyl), which can enter live cells via the cellular membrane, is utilized in biology because it can evaluate the viability of cells and mark them briefly.

3.1.4 Glucose

Glucose is one of the most prevalent monosaccharide, a subclass of carbohydrates. The chemical formula of glucose is $C_6H_{12}O_6.H_2O$ and molecular weight is 198.171 g/mol.

3.1.5 Sucrose

The most prevalent sugar is sucrose. The chemical formula of sucrose is $C_{12}H_{22}O_{11}$ and molecular weight is 342.2965 g/mol.

3.1.6 Sodium chloride

Sodium chloride is generally known as salt. Its chemical formula is NaCl and molecular weight is 58.44 g/mol.

3.1.7 Sodium hydroxide

Common terms for the inorganic compound sodium hydroxide include lye and caustic soda. Its chemical formula is NaOH and molecular weight is 39.997 g/mol.

3.1.8 Piperazine-1, 4-bis (2-ethanesulfonic acid)

PIPES, is a buffering agent that is commonly employed in biochemistry. It is a buffer for ethanesulfonic acid. Its chemical formula is $C_8H_{18}N_2O_6S_2$ and molecular weight is 302.36 g/mol.

3.1.9 Ethylene glycol-bis (2-aninoethylether)-*N,N,N′N′*-tertraacetic acid

EGTA, commonly referred as egtazic acid, is a chelating agent. Its chemical formula of EGTA is $C_{14}H_{24}N_2O_{10}$ and molecular weight is 380.35 g/mol.

3.1.10 Bovine serum albumin

BSA is a kind of serum albumin protein that comes from cows. In research, it is frequently used as a reference for protein concentration. Its chemical formula is $C_{123}H_{193}N_{35}O_{37}$ and molecular weight is 66430.3 g/mol.

3.1.11 Chloroform

Chloroform, generally known as trichloromethane, is a translucent, colorless liquid which is thicker than water and has a pleasing ether-like odor. It is nonflammable. Its chemical formula is $CHCl_3$ and molecular weight is 119.37 g/mol.

3.2 Chemicals for the Synthesis of Magnetite NPs

The chemicals which were used for the synthesis of magnetite NPs are: Ferric chloride anhydrous ($FeCl_3$), ferrous chloride tetra hydrates ($FeCl_2 \cdot 4H_2O$), sodium hydroxide (NaOH), diethylene glycol (DEG), and *Ipomoea aquatica* leaf extracts etc.

3.3 Instruments for the Synthesis of NPs and GUVs

The main instruments that were used for these investigations are: Inverted phase contrast fluorescent microscope (Olympus IX 73, Japan) connected with CCD camera (DP22, Olympus, Japan), Centrifuge machine (NUVE NF 800R, Turkey), Peristaltic pump (SP2, China), Incubator (Phoenix Tin-35, Germany), Drying oven (Ecocell, Germany), pH meter (BT675 Boeco, Germany), Analytical balance (Radwag, Poland), Vortex mixture (Stuart SA8, UK), Motor drive magnetic stirrer with hotplate (MSH 420, Boeco, Germany), Bath sonicator (Hwashin, Korea), Precision micropipette (OHAUS, USA) etc.

3.4 Synthesis Reaction of Fe_3O_4 NPs

Fe_3O_4 NPs were conjugated employing a natural green conjugation method that employed $FeCl_3$ and $FeCl_2 \cdot 4H_2O$ as precursors and *Ipomoea aquatica* leaf extract as reducing and capping agents. *Ipomoea aquatica* leaf extract was assimilated to a liquid combination of Fe^{3+} and Fe^{2+} chloride at a 2:1 ratio to make Fe_3O_4 [139]. The interplay among Fe_3O_4 NPs charged groups that were implicated with *Ipomoea aquatica* leaf extract is shown in Fig. 3.5. The following is a summary of the overall reaction:

Ipomoea aquatica + H_2O + Fe^{2+}(aq) + Fe^{3+}(aq) $\longrightarrow$ [*Ipomoea aquatica* / Fe^{3+} - Fe^{2+}]

[*Ipomoea aquatica* / Fe^{3+} - Fe^{2+}] + 8OH^- (aq) $\longrightarrow$

[*Ipomoea aquatica* / Fe_3O_4] $\downarrow$(s) + 4H_2O (aq)
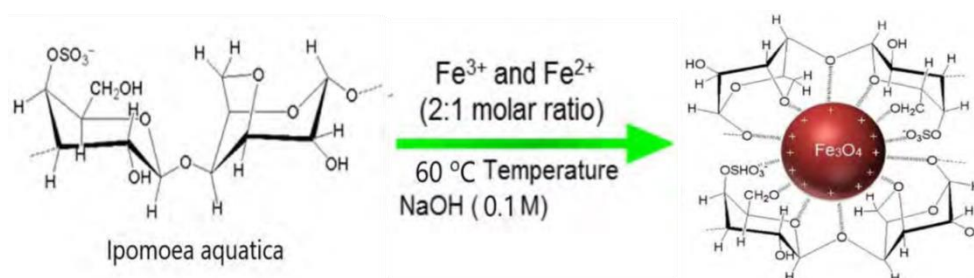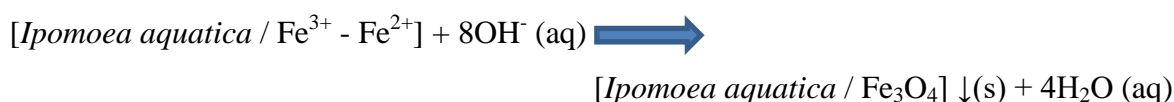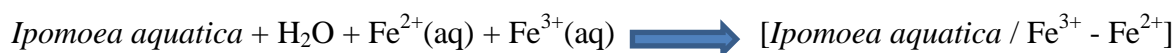
Fig. 3.5 Interaction between Fe_3O_4 NPs charged groups and *Ipomoea aquatica* leaf extract [140].

3.4.1 *Ipomoea aquatic* leaf extracts preparation

Ipomoea aquatica, often known as water spinach, is a haughty hemi-hydrophyte plant cultivated for its young leaves and shoots as a potherb. Fig. 3.6 shows the steps for preparing the *Ipomoea aquatica* leaf extracts. At first, the leaves of *Ipomoea aquatica*

were purchased from a nearby market. To eliminate dust, the leaves were mildly rinsed in de-ionized water. The leaves were air dried in a dust-free setting. To make the finest paste, dried leaves were sliced into exquisite bits, knead and strained. 60 g of the leaves paste was diluted with 400 mL de-ionized water and boiled for 4 hours and 30 minutes at 80 °C. Straining the composition using Whatman No.1 filter paper after cooling the leaf extracts was obtained and stored at 4 °C for subsequent studies.
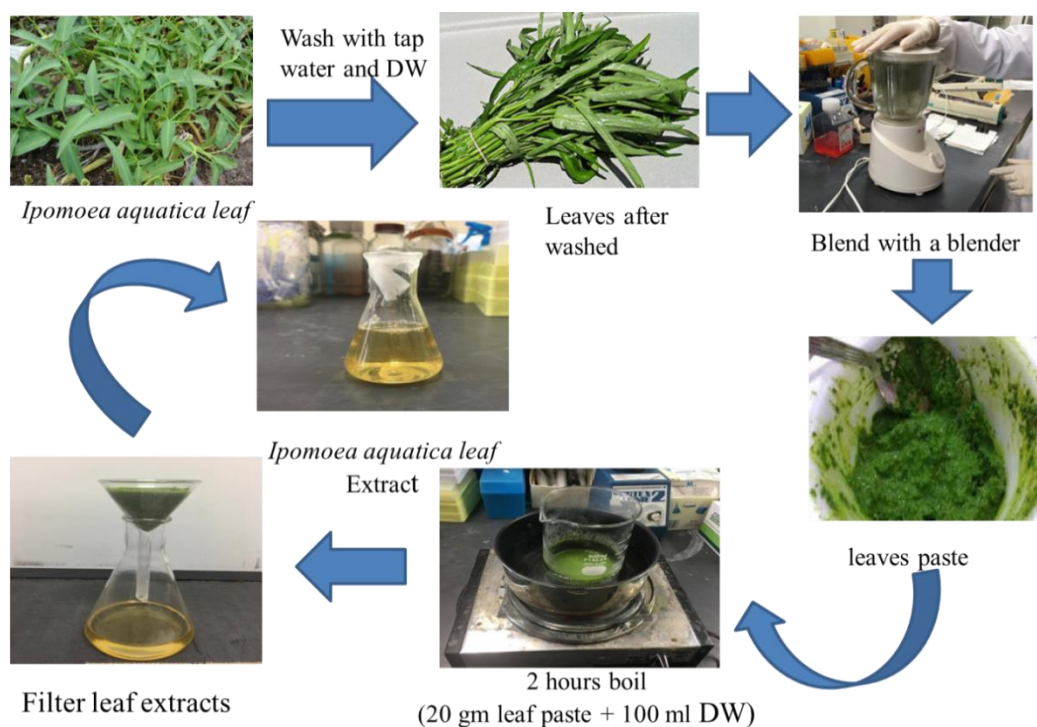
Fig. 3.6 *Ipomoea aquatica* leaf extracts preparation

3.4.2 Synthesis of magnetite NPs

The following is a detailed description of the Fe_3O_4 NPs synthesis procedure:

To make a 0.05 M solution, mix 0.99 g $FeCl_2.4H_2O$ with 100 mL DI water, and mix 1.622 g $FeCl_3$ with 100 mL DI water to prepare a 0.1 M solution. In a individual beaker with magnetic stirrer (800 rpm), combine 20 mL 0.05 M $FeCl_2.4H_2O$ and 20 mL 0.1M $FeCl_3$ at 60 °C. After 10 minutes, add 5 mL Ipomoea aquatica leaf extract to the composition and stir along with the magnetic stirrer. After another 10 minutes, 100 mL 0.10 M NaOH solution was assembled, and the solution color changed to black, indicating the generation

of Fe$_3$O$_4$ NPs. The biomolecules of leaf extracts acted as stabilizers as well as reducing agents to prepare NPs using FeCl$_3$ and FeCl$_2$·4H$_2$O as precursors.
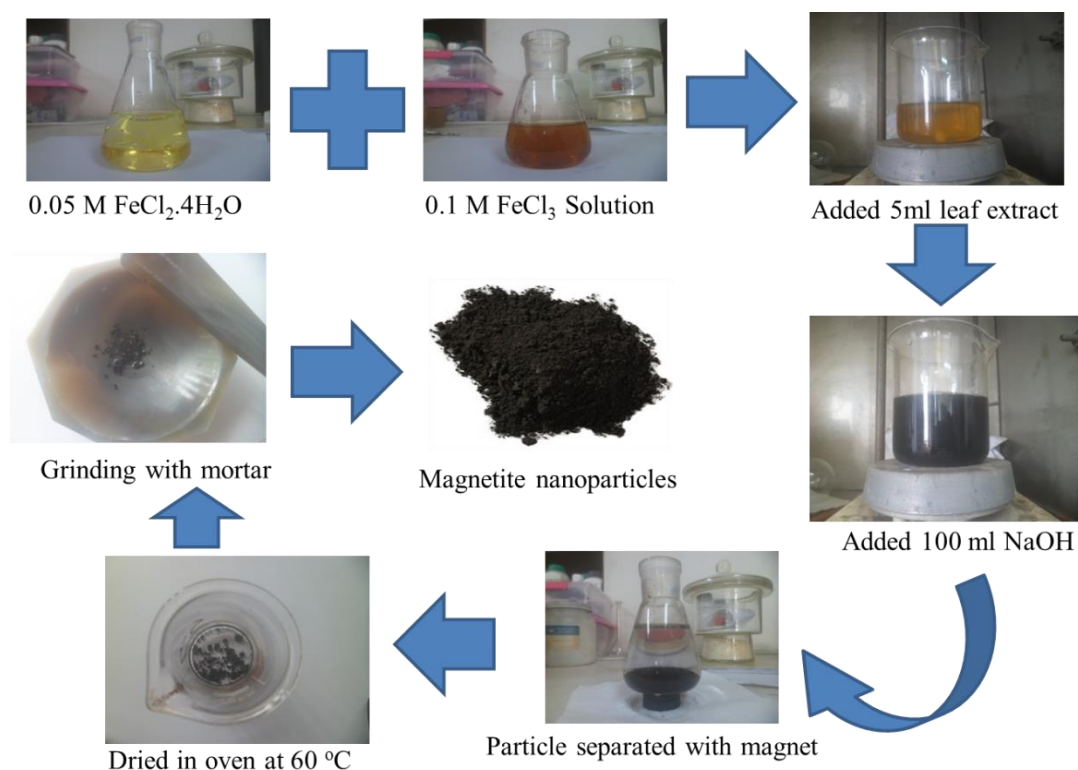
Fig. 3.7 Synthesis the magnetite NPs

3.4.3 Concentration of magnetite NPs

At the final stage of the synthesis, the NPs were precipitated at the bottom of glass beaker, which then accumulated using a magnetic bar. The solution in the beaker on the upper side was removed. The synthesized NPs were placed in aluminum foil and drier for 48-72 hours at 60 °C (dried NPs are shown). The dried NPs were then converted to powder form using a hand mortar. At first, a relatively higher NPs concentration of 0.20 mg/mL was prepared in the buffer for charged vesicles and in MilliQ for neutral vesicles, which was then diluted to several concentrations such as 0.006, 0.01, and 0.013 mg/mL. To interact the NPs with lipid vesicles, 100 μL NPs were mixed with 200 μL purified suspension of GUVs in a microchamber. Hence, the total volume of NPs and vesicles suspension was 300 μL. In that case, the corresponding effective concentrations of NPs in the observation microchamber were 2.00, 3.33, and 4.67 μg/mL.

3.4.4 Zeta potential and average size of magnetite NPs

The zeta potential is a measure of the difference in potential between the bulk fluid in which a particle is dispersed and the layer of fluid containing the oppositely charged ions that is associated with the nanoparticle surface. It is commonly used to determine the magnitude of a charge. The surface charge density of NPs was investigated using the zeta potential. The zeta potential, as shown in Fig. 3.8, is the conventional method for observing the surface charge. The electrostatic repulsive force between the NPs is provided by the zeta potential, which is approximately -21.3 mV, confirming that the magnetite NPs are anionic [59].
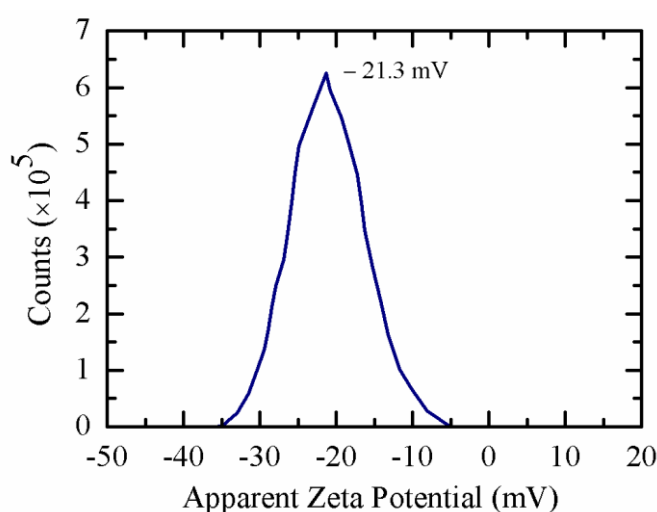
Fig. 3.8 Zeta potential of magnetite NPs [59]

TEM examination was used to determine the size and shape of the produced Fe_3O_4 NPs, as illustrated in Fig. 3.9. In order to do TEM examination, a suspension of Fe_3O_4 NPs in ethanol was made, and 1 μL of the suspension was applied to a formvar-coated grid, dried at 25 ⁰C, and then stored on a specimen holder. At a 120 kV accelerating voltage, the image was observed. The TEM image amply displays the uniform distribution, smooth edges, and spherical shape of the produced Fe_3O_4 NPs. The particle sizes of the synthesized NPs were in the range of 15 to 20 nm and the average size was 18 nm.
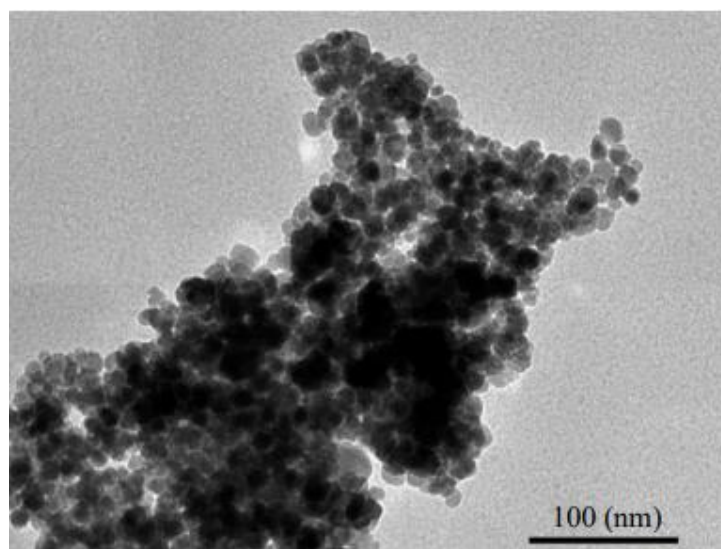
Fig. 3.9 TEM image of Fe₃O₄ NPs [132].

3.5 Synthesis of GUVs

The DOPG/DOPC/chol (70/30/0) (70/30/0 specifies molar ratio), DOPG/DOPC/chol (46/39/15), DOPG/DOPC/chol (43/28/29), and DOPG/DOPC/chol (40/20/40)-GUVs were prepared in a physiological buffer (10mM PIPES, 150mM NaCl, pH 7.0, 1mM EGTA) using the natural swelling method [141]. The surface charge density of these charged membranes was almost the same (-0.16 C m^{-2}) for 0, 15, 29 and 40% chol [58]. For the preparation of charged GUVs, at first, 1 mM DOPG, DOPC and cholesterol (total amount of the mixture was 200 mL) were taken into a glass vial (4.5 mL), which was slightly shaked and kept without any motion for 1 minute to get a homogeneous composition mixture. The solution was dried with a mild flow of nitrogen gas to produce a thin and homogeneous lipid film. Then, the glass vial was kept in a vacuum desiccator for 12 hours. After this, the sample was pre-hydrated for 8 min at 45 ℃ by pouring 20 mL MilliQ water into the vial, followed by incubation for 3.5 hours at 37 ℃ with 1 mL 0.10 M sucrose in buffer. To prepare the fluorescent probe (calcein) encapsulated GUVs, we used 1 mM calcein with 0.10 M sucrose in buffer for incubation of the suspension of vesicles. To prepare the neutral membranes containing cholesterol, DOPC/chol (100/0), DOPC/chol (85/15), DOPC/chol (71/29), DOPC/chol (60/40)-GUVs were prepared in 0.10 M sucrose containing MilliQ water. The steps of synthesis of GUVs are shown in the block diagram (Fig. 3.10) and schematic figure below.
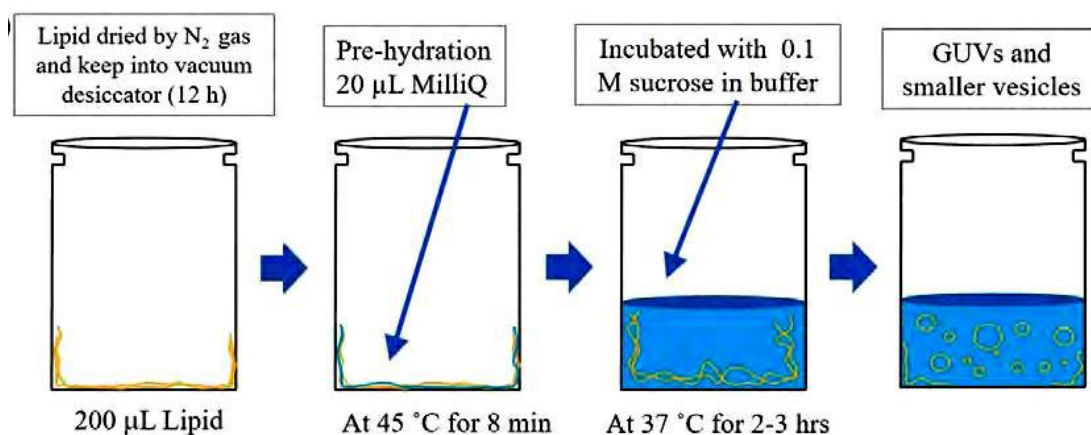
Fig. 3.10 Schematic diagram of the synthesis of GUVs using the natural swelling method

Table 3.1 Different types of sample

Chol	Sample	
(%)	**Charged membrane (DOPG/DOPC/Chol)**	**Neutral membrane (DOPC/Chol)**
0	70/30/0	100/0
15	46/39/15	85/15
29	43/28/29	71/29
40	40/20/40	60/40

3.6 Purification of GUVs

Following incubation, the GUVs suspension was centrifuged at $13,000 \times g$ (here g is the acceleration due to gravity) for 20 minutes at 20 °C using a refrigerated centrifuge, and the supernatant bearing GUVs was filtered through a nuclepore polycarbonate membrane with a 10 μm diameter pores (Whatman® Nuclepore™ Track-Etched Membranes, UK) clamped in a polypropylene filter holder (Swinnex, $\phi = 25$ mm, Millipore Co., Billerica, MA). The filter holder's upper end was associated to a 10 mL plastic (polypropylene) syringe 2 (JMI Syringes and Medical Devices Ltd. Bangladesh), and the lower end was associated to a tube bearing three different types of polypropylene fittings (Luer fittings

VRFE6, VRFC6, VRSC6; AS-ONE, Japan) with an internal diameter of 3 mm. The tube in this scenario has a total of 9 fittings, as in the membrane filtering method [123].
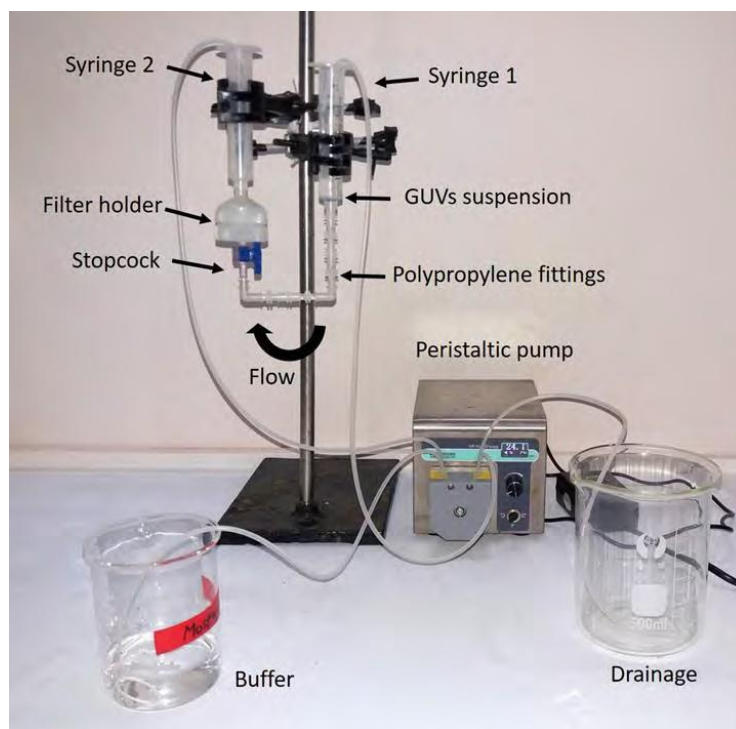
Fig. 3.11 Membrane filtration method [142]

The tube's opposite end was linked to syringe 1, which had the similar 10 mL capacity as the tube. The GUV solution in 0.10 M glucose buffer was assembled to syringe 1, wherein the buffer flow was constantly regulated by a double-headed peristaltic pump (CPPSP2, Shenchen, China) via a plastic tube with an internal diameter of 3 mm (JMI Syringes and Medical Devices Ltd. Bangladesh). Air bubbles were meticulously eliminated from the polypropylene tube and filter holder before initiating the flow of buffer from beaker to syringe 1. Fig. 3.11 depicts the purification technique's configuration. Because the buffer flowed from the bottom to the top at the filter, relatively small vesicles were allowed to get via the filter and enter the top syringe (syringe 2).The injection of buffer bearing 0.10 M glucose to syringe 1 was halted after a set amount of time had passed, and the buffer within syringe 2 was withdrawn through the pump at the equivalent streaming rate. In fine, the filter holder and suspension in the tube was culled and filtered before being employed as a GUV suspension.

3.7 Observations of GUVs

After purification, a microchamber was filled with 200 µL of purified GUVs suspension (the inner fluid is 0.10 M sucrose in buffer, whereas the exterior fluid is 0.10 M glucose in buffer) as shown in Fig. 3.12(a). In a handcrafted microchamber (total volume 300 µL), different intentness of 100 µL NPs were introduced to a 200 µL GUVs suspension. A U-shaped silicone rubber spacer was used to create the microchamber on a glass slide. In the GUVs suspension, the NPs concentration is deemed uniform. The effective NP concentrations in the suspension were calculated to be 2.00, 3.33, and 4.70 µg/mL, respectively. For reducing the strong attraction of GUVs to glass, 0.10% (w/v) BSA disintegrated in the buffer bearing 0.10 M glucose was applied to the glass surface and the microchamber.
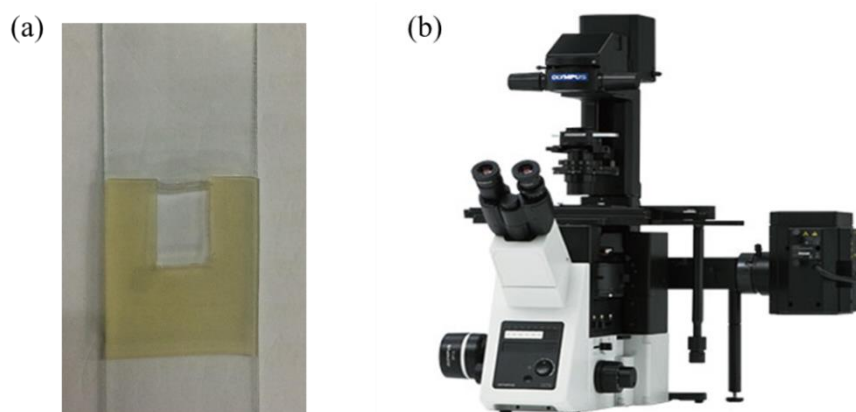
Fig. 3.12 (a) GUVs suspension in the microchamber, and (b) Inverted phase contrast microscope (Olympus IX-73, Japan)

The colorless and clear specimens, as well as live cells, can be viewed using phase contrast microscopy. The GUVs were observed and also the deformation and poration were investigated using an inverted phase contrast fluorescence microscope with a 20× objective at 25 ± 1 °C. The images of GUVs were taken by a charge-coupled device camera as shown in Fig. 3.12(b).

Both phase contrast and fluorescence microscopes were used to evaluate the impacts of cholesterol on the deformation and poration of GUVs. The images are shown in Fig 3.13. The encapsulated calcein solution is indicated by the green color in the inside of GUVs in Fig 3.13(b).
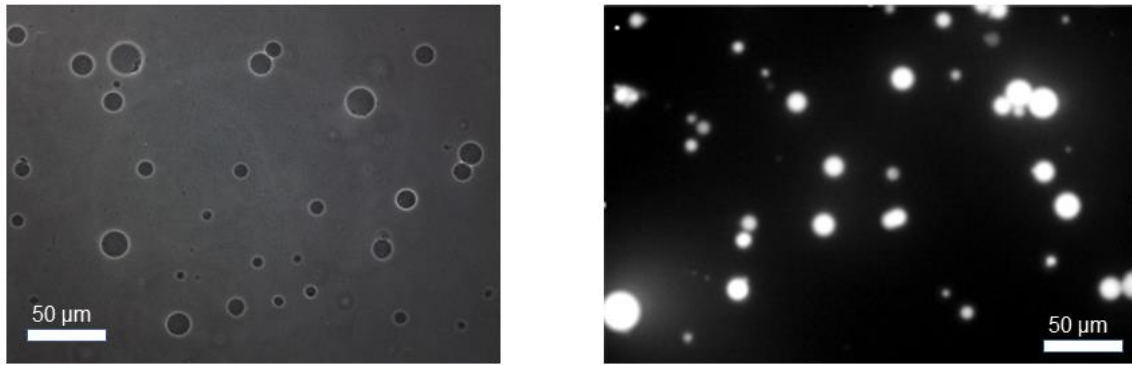
Fig. 3.13 Microscopic images of GUVs in the solution (a) Phase contrast image.
(b) Fluorescence image. Scale bar is 50 μm.

3.7.1 Phase contrast microscope

Phase-contrast microscopy is an optical microscopy technique that transforms brightness variations in the image from phase shifts in light flowing through a transparent material. While phase shifts are imperceptible in and of themselves, brightness differences make them noticeable. Fig. 3.14 shows the different parts of phase contrast microscope.
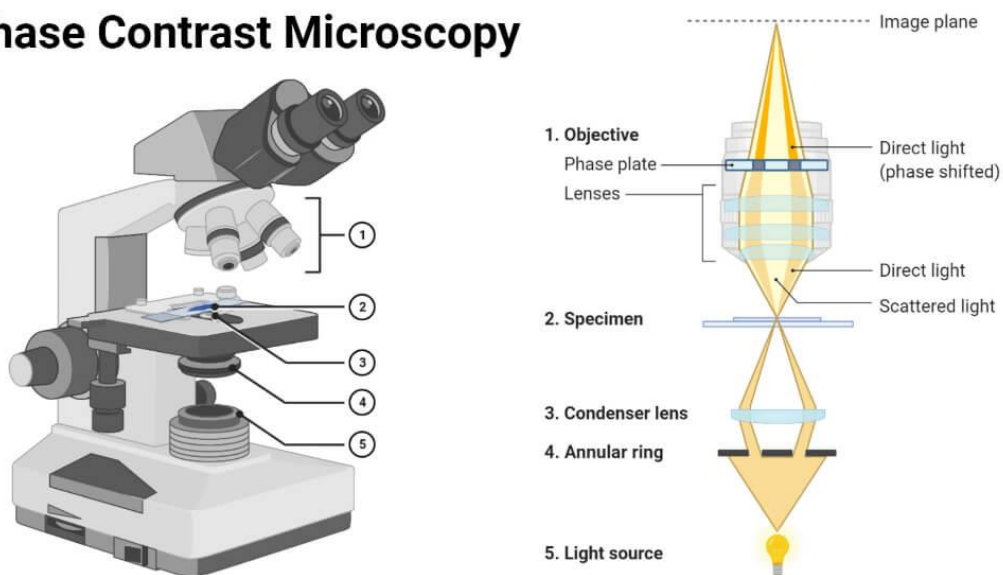
Fig. 3.14 Phase contrast microscope [143]

An annular phase plate and annular diaphragm are added to a specifically constructed light microscope's fundamental components for phase-contrast microscopy. The light rays are

allowed to pass through the annular diaphragm, and then the light rays fall on the specimen or object to be studied. The phase plate is a transparent disc. With the help of the annular diaphragm and the phase plate, the phase contrast is obtained in this microscope. This is obtained by separating the direct rays from the diffracted rays.

Phase contrast microscope has numerous applications to produce high-contrast images of transparent specimens in biological research, such as- living cells (usually in culture), microorganisms, thin tissue slices, lithographic patterns, fibers, latex dispersions, glass fragments, and subcellular particles (including nuclei and other organelles).

3.7.2 Fluorescence microscope

A fluorescence microscope is an optical microscope that studies the characteristics of organic or inorganic substances by using fluorescence instead of, or in addition to, scattering, reflection, attenuation, or absorption. Any microscope that produces images using fluorescence is referred to as a "fluorescence microscope," whether it has a straightforward setup like an epifluorescence microscope or a more intricate setup like a confocal microscope, which uses optical sectioning to improve the resolution of the fluorescence image. Fig. 3.15 shows the fluorescent microscope.

The fundamental idea behind fluorescence microscopy is to colour the components by dyes. A light source with a much higher intensity is used in fluorescence microscopy to illuminate the sample. Fluorescence species in the sample are stimulated by this light, and they subsequently emit light with a larger wavelength. Through the objective lens, light with the excitation wavelength is focused on the specimen. The objective focuses the fluorescence that the specimen emits onto the detector. Only reflected excitation light, along with the emitted light, enters the objective since the majority of excitation light passes through the specimen. The second light source, or the fluorescent species' emission wavelength, is employed to create the image rather than the light that was first used to illuminate and excite the sample.
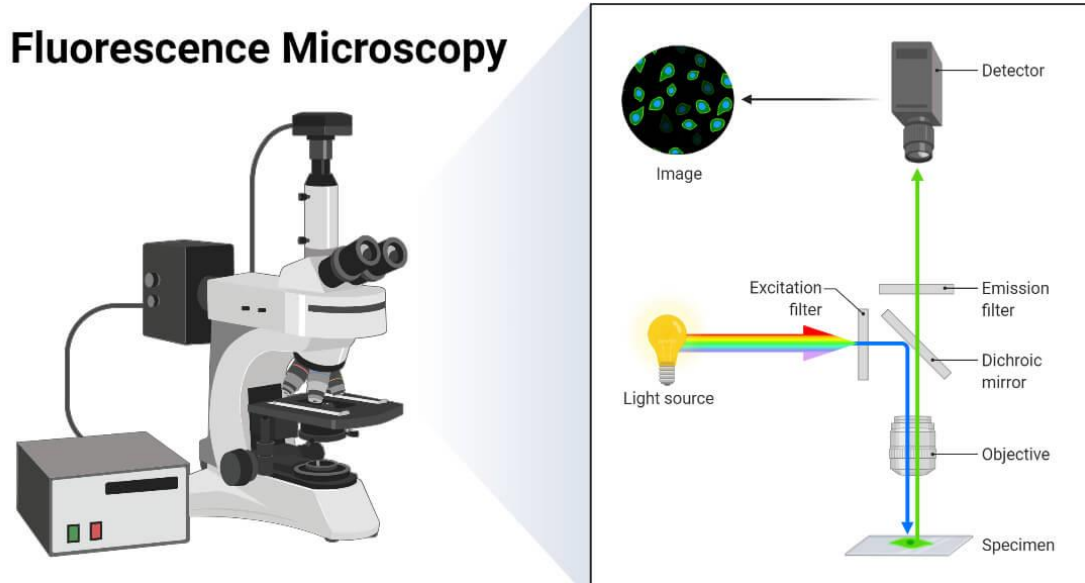
Fig. 3.15 Fluorescence microscope [144]

Because it enables the use of multicolor staining, labeling of structures within cells, and evaluation of the physiological state of a cell, fluorescence microscopy is a frequently used technology in today's life science research.

3.8 Compactness and Surface Area of a GUV

Compactness (C_{om}) is a property in mathematics, specifically general topology that aims to generalize the concept of a closed and limited subset of Euclidean place by defining the concept of a place without "holes" or "missing endpoints," i.e., there are no "limiting values" of points that are excluded from the space.

Compactness (C_{om}) is a typical shape measurement approach in biomedical imaging [145] that quantifies the form change of a GUV and is described as follows:

$$C_{om} = \frac{P^2}{4\pi S_{cr}} \tag{3.1}$$

Here, P denotes the perimeter and S_{cr} denotes the area of the image cross section of GUVs. $C_{om} = 1.0$ is the minimum value for a circle, but it grows with any deviation. The C_{om} for each deformed image was calculated using the MATLAB image processing toolkit. The

primary effect of NPs on GUVs is an increase in their overall surface area (S_{GUV}). As a result, we associate S_{GUV} to the change of C_{om}. For the sake of simplicity we assume that this ellipsoid's long axis is similar to its short one. The following is how a distorted GUV's surface area is calculated:

$$S_{GUV} \approx S_0 \left(1 + \frac{3}{2}\Delta\right) \tag{3.2}$$

Here, S_0 is the surface area of a circular GUVs, $\Delta = \alpha\sqrt{(C_{om} - 1)}$ and $= \sqrt{[1/(\frac{3}{\pi} - \frac{1}{4})]}$.

As a result, the following relationship emerges:

$$S_{GUV} = s_0(1 + 1.78\sqrt{c_{om} - 1}) \tag{3.3}$$

Elastic energy of a closed bilayer is,

$$W_{el} = W_b + W_r$$
$$= \frac{1}{2} k_c \int (C_1 + C_2)^2 dA + \frac{1}{2}\frac{k_r}{A_o h^2}(\Delta A - \Delta A_o)^2 \tag{3.4}$$

Here, W_b is the membrane bending energy, W_r is the correlative single-layer stretching energy, k_c is the local bending modulus, k_r is the nonlocal bending modulus, A_o is the surface area of the bilayer, ΔA is the area difference at stretched state, ΔA_o is the area difference at equilibrium (relaxed) state, h is the distance between two monolayer, and c_1 & c_2 are the two main curvatures.

3.9 Fraction of Deformation and Poration of GUVs

Fraction of deformation (Fr_d) is defined as the ratio of the amount of deformed GUVs N_d (the overall amount of analyzed GUVs was $N = 50-60$) to that of total number of observed GUVs at a definite time. The fraction of deformed is calculated as,

$$\text{Fraction of deformation} = \frac{Number\ of\ deformed\ GUV}{Total\ number\ of\ GUVs} \tag{3.5}$$

By calculating the probability of deformation and poration among all the recorded GUVs, the percentage of deformed GUVs (Fr_d) and fraction of pore formed GUVs (Fr_p) were computed. We'll show how to compute these fractions. 100 μL NPs interacted with purified GUVs suspension of 200 μL at a specific concentration of NPs. In the micro

chamber, the total volume of the NPs-GUVs suspension was 300 µL. The images of vesicles were taken at different moments during interaction, such as 0, 10, 20, 30, 40, 50, and 60 minutes, while holding the focus at a fixed place. Then, for other chambers, similar trials were carried out. The number of distorted and pore-formed GUVs was determined from multiple images of all the studied GUVs at each time. For a separate experiment, we determined the Fr_d and Fr_p at different periods. The same process was followed for numerous independent experiments, yielding Fr_d and Fr_p values for each. For a defined time and cholesterol content, the mean value with standard deviation of Fr_d and Fr_p were calculated.

3.10 NPs-Induced Leakage of Calcein from the Inside of GUVs

To study the poration of GUVs caused by NPs, 100 µL of NPs were introduced to a 200 µL suspension of calcein encapsulated GUVs. During the interaction, we concentrated on one GUV. A CCD camera and a fluorescent microscope were used to capture the GUV. When the leaking of calcein decreased rapidly, the beginning of pore development in GUV membranes occurred. The pre-pore's free energy in the case of a toroidal pore is [169, 170]:

$$U(r, \sigma_n) = 2\pi r \Gamma - \pi r^2 (\sigma_n + B) \tag{3.6}$$

Where B is the electrostatic term due to charge lipids, r is the radius of a pre-pore, and Γ is the line tension (pre-pore's per-length free energy). The energy of a pre-pore's barrier is,

$$U_B(r, \sigma_n) = \frac{\pi \Gamma^2}{\sigma_n + B} \tag{3.7}$$

For varied concentrations of NPs and cholesterol content in membranes, time-dependent leakage of several 'single GUV' was detected. For diverse cholesterol-containing membranes, the average time of poration was estimated.

CHAPTER 4

RESULTS AND DISCUSSION

4.1 Deformation and the Compactness of DOPG/DOPC/chol-GUVs in the presence of 3.33 µg/mL NPs

The effects of cholesterol on the NPs-induced deformation and the degree of deformation (compactness) of GUVs were examined. The interaction of 3.33 µg/mL NPs with a single DOPG/DOPC/chol (70/30/0)-GUV is depicted in Fig. 4.1(a). In the absence of NPs, the GUV has a spherical structure at 0 min, as shown in Fig. 4.1(a). Within the first 4 minutes after adding NPs to the GUV suspension, this shape does not change. A little deformation began at 5 minute, and a major deformation appeared between 45 and 60 minutes. The compactness, C_{om}, is used to determine the degree of deformation. The time course of C_{om}, is shown in Fig. 4.1(b). The value of C_{om} was 1.0 at 0 minutes. At time 5, 10, 15, 25, 35, 45, 55, and 60 minutes, the values of C_{om} were 1.0301, 1.0392, 1.0618, 1.0803, 1.1983, 1.3057, 1.3854, and 1.4004, respectively.
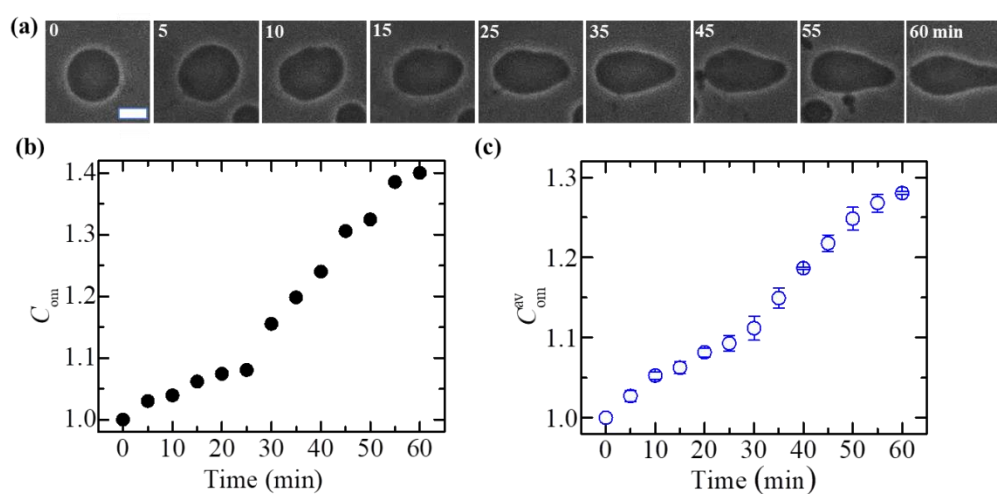
Fig. 4.1 The deformation and the corresponding compactness of DOPG/DOPC/chol (70/30/0)-GUV in the presence of 3.33 µg/mL NPs. (a) Phase contrast images of a single GUV's demonstrate the deformation. The number on each image depicts the time in minutes after the addition of NPs. Scale bar is 15 µm. (b) The time dependen compactness, C_{om}, of the GUV as shown in (a). (c) The time dependent average compactness, C_{om}^{av} of several GUVs under the same conditions as shown in (a).

The change in average compactness, C_{om}^{av}, is shown in Fig. 4.1(c), where C_{om}^{av} increases with time. In each separate experiment, the average value of compactness, C_{om}^{av}, and standard deviations at various times were calculated from three different experiments using a number of $N = 15\text{-}20$ measured GUVs. It is reasonable to assume that as time passes, NPs absorption at membrane interfaces rises, resulting in increased surface pressure in the membrane and, which in turn causes C_{om}'s value to rise.

The interaction of NPs at 3.33 µg/mL with a single DOPG/DOPC/chol (46/39/15)-GUV is shown in Fig. 4.2(a). The GUV has a spherical structure at 0 min in the absence of NPs, as illustrated in Fig. 4.2(a). This structure does not alter in the first 9 min after adding NPs to the GUV suspension. After 10 minutes, a minor deformation emerged, followed by a substantial deformation between 45 and 60 minutes.
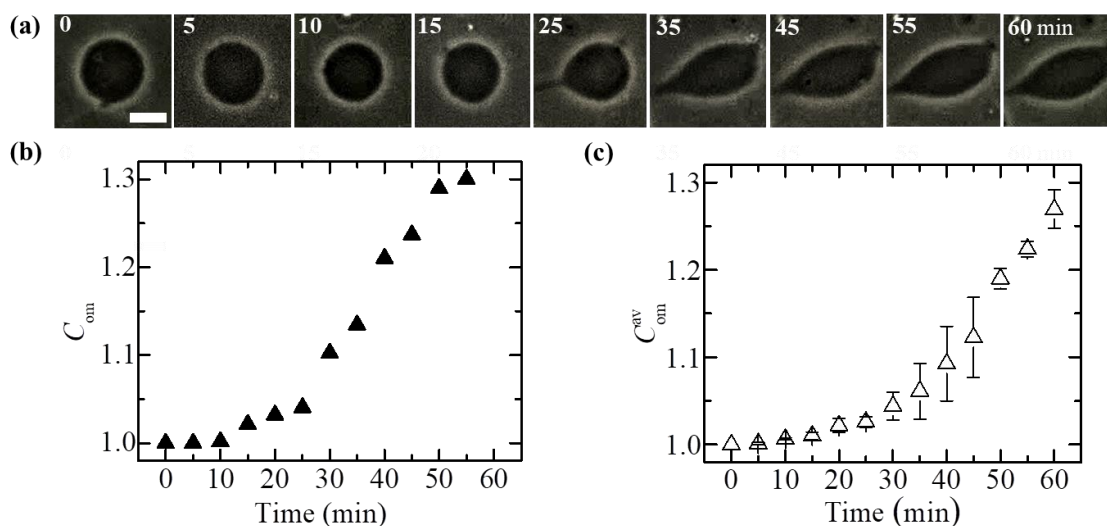
Fig. 4.2 The deformation and the corresponding compactness of DOPG/DOPC/chol (46/39/15)-GUV in the presence of 3.33 µg/mL NPs. (a) Phase contrast images of a single GUV's demonstrate the deformation. The number on each image depicts the time in minutes after the addition of NPs. Scale bar is 15 µm. (b) The time dependent compactness, C_{om}, of the GUV as shown in (a). (c) The time dependent average compactness, C_{om}^{av} of several GUVs under the same conditions as shown in (a).

The time course of compactness, C_{om} is shown in Fig. 4.2(b). At 0 minute, C_{om} was 1.0, and at 5, 10, 15, 25, 35, 45, 55, and 60 minutes, the C_{om} values for DOPG/DOPC/chol (46/39/15)-GUV were 1.000, 1.0087, 1.0214, 1.0405, 1.1345, 1.2366, 1.3001, and 1.334,

respectively. In Fig. 4.2(c), the time course of average compactness, C_{om}^{av}, in the membrane of DOPG/DOPC/chol (46/39/15)-GUVs is depicted, with C_{om}^{av} increasing with time.

Fig. 4.3(a) shows the interaction of 3.33 µg/mL NPs with a single DOPG/DOPC/chol (43/28/29)-GUV. In the absence of NPs, GUV has a spherical structure at 0 min (Fig. 4.3a), and in the first 9 minute after adding NPs to the GUV suspension, this structure does not vary, and a modest deformation appeared after 10 minutes, followed by a significant deformation between 45 and 60 minutes, which is similar to 15% chol containing membranes.
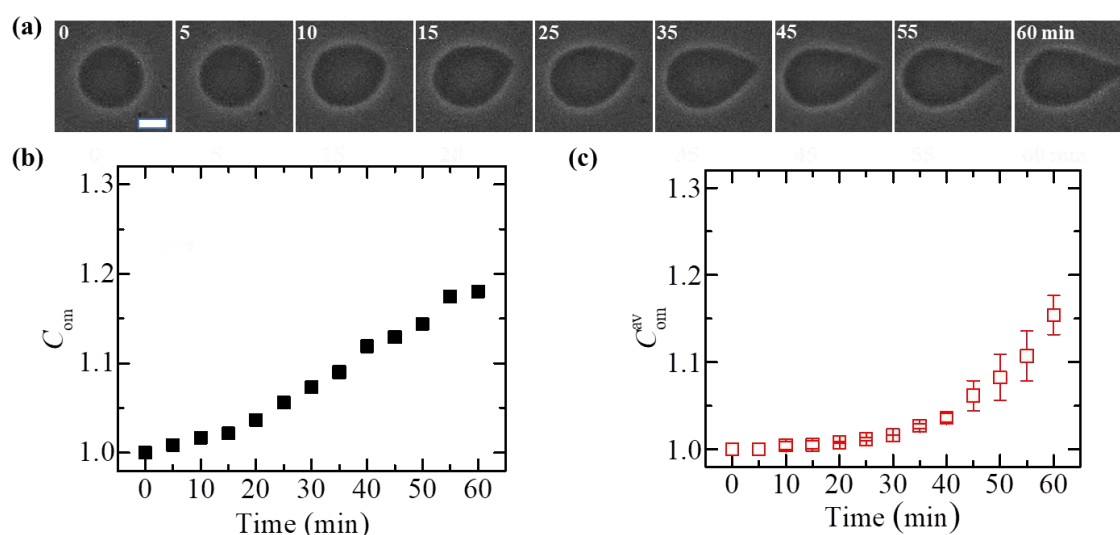
Fig. 4.3 The deformation and the corresponding compactness of DOPG/DOPC/chol (43/28/29)-GUV in the presence of 3.33 µg/mL NPs. (a) Phase contrast images of a single GUV's demonstrate the deformation. The number on each image depicts the time in minutes after the addition of NPs. Scale bar is 15 µm. (b) The time dependent compactness, C_{om}, of the GUV as shown in (a). (c) The time dependent average compactness, C_{om}^{av} of several GUVs under the same conditions as shown in (a).

The time course of compactness, C_{om} is delineated in Fig. 4.3(b). C_{om} was 1.0 at 0 minute, and at 5, 10, 15, 25, 35, 45, 55, and 60 minutes, the C_{om} values for DOPG/DOPC/chol (43/28/29)-GUV were 1.0086, 1.0168, 1.0217, 1.0561, 1.0901, 1.129, 1.1744, and 1.1803, respectively. The time course of average compactness, C_{om}^{av}, of the membrane of DOPG/DOPC/chol (43/28/29)-GUVs is shown in Fig. 4.3 c), which increases with time.

The interaction of 3.33 μg/mL NPs with a single DOPG/DOPC/chol (40/20/40)-GUV is represented in Fig. 4.4(a). In the absence of NPs, the GUV has a spherical form at 0 minute (Fig. 4.4(a)), and this form does not change for the first 9 minute after adding NPs to the GUV suspension. A tiny deformation emerged after 10 minute, followed by a massive deformation between 45 and 60 minutes, which is similar to 15% cholesterol containing membranes.
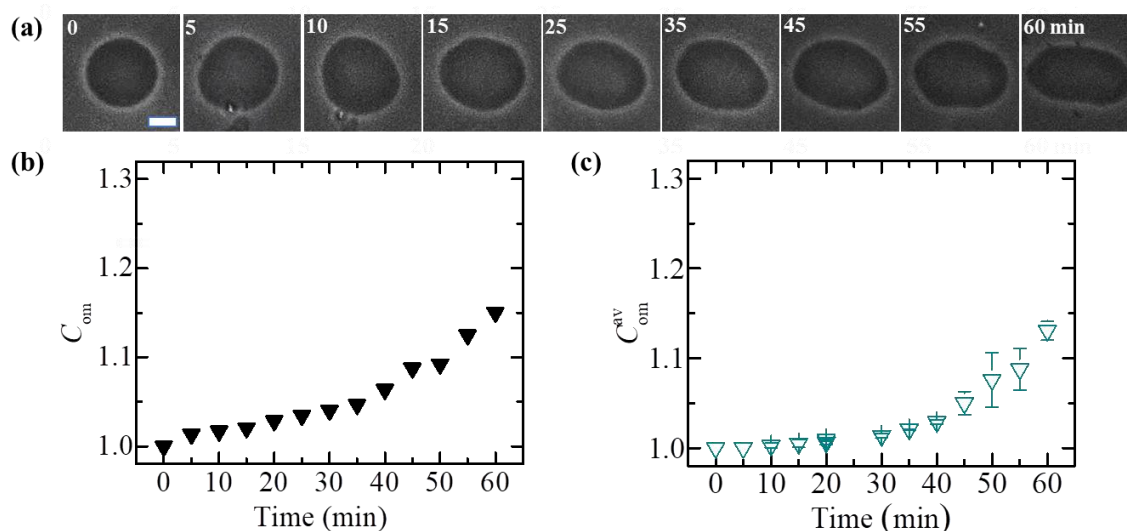
Fig. 4.4 The deformation and the corresponding compactness of DOPG/DOPC/chol (40/20/40)-GUV in the presence of 3.33 μg/mL NPs. (a) Phase contrast images of a single GUV's demonstrate the deformation. The number on each image depicts the time in minutes after the addition of NPs. Scale bar is 15 μm. (b) The time dependent compactness, C_{om}, of the GUV as shown in (a). (c) The time dependent average compactness, C_{om}^{av} of several GUVs under the same conditions as shown in (a).

The time course of compactness, C_{om} is shown in Fig. 4.4(b). The C_{om} values for GUV were 1.0 at 0 minute and at 5, 10, 15, 25, 35, 45, 55, and 60 minutes, 1.0134, 1.017, 1.0205, 1.0345, 1.0467, 1.0687, 1.0825, and 1.1501, respectively. Fig. 4.4(c) represents the time course of average compactness, C_{om}^{av} of DOPG/DOPC/chol (40/20/40)-GUVs membranes, which increases with time. The values of average compactness for different charged membranes at 60 minutes are presented in Table 4.1

Table 4.1 Average compactness of charged DOPG/DOPC/chol GUVs at 60 minute

Sample	Chol (%)	Average Compactness, C_{om}^{av}
70/30/0	0	1.2805 ± 0.0022
46/39/15	15	1.2693 ± 0.0221
43/28/29	29	1.1541 ± 0.0223
40/20/40	40	1.1307 ± 0.0104

4.2 Deformation and the Compactness of DOPC/chol-GUVs in the presence of 3.33 μg/mL NPs

Following that, we looked at the deformation and compactness of cholesterol containing neutral membranes in the presence of 3.33 μg/mL NPs. Fig. 4.5(a) shows the phase contrast images of a DOPC/chol (100/0)-GUV due to the interaction of NPs.
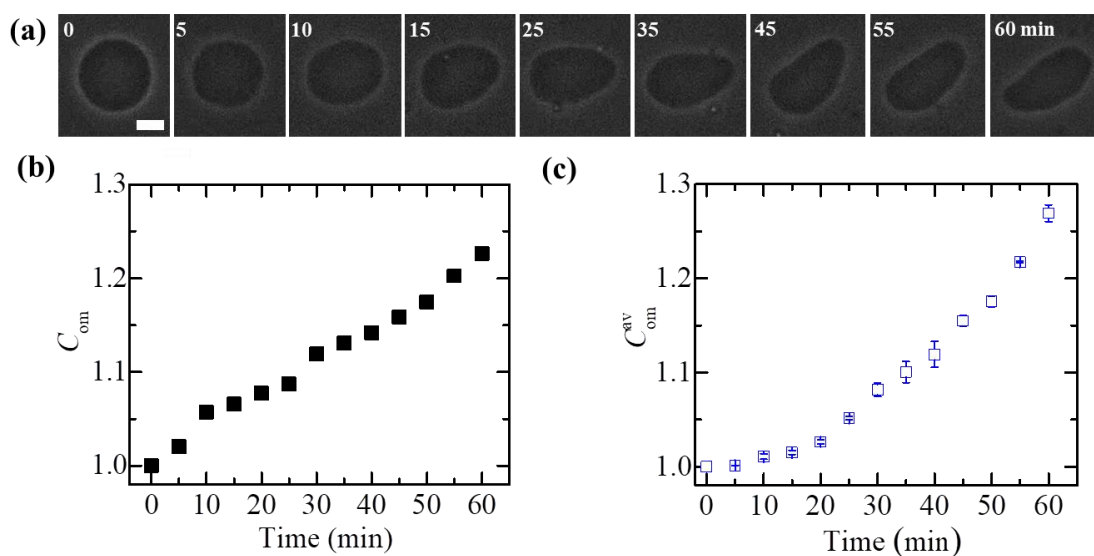
Fig. 4.5 The deformation and the corresponding compactness of DOPC/chol (100/0)-GUV in the presence of 3.33 μg/mL NPs. (a) Phase contrast images of a single GUV's demonstrate the deformation. The number on each image depicts the time in minutes after the addition of NPs. Scale bar is 15 μm. (b) The time dependent compactness, C_{om}, of the GUV as shown in (a). (c) The time dependent average compactness, C_{om}^{av} of several GUVs under the same conditions as shown in (a).

It was spherical in shape before the addition of NPs. With time, the shape deformed from spherical shape, indicating the value of C_{om} to rise. For the first 4 minutes, the GUV was unchanged, but from 5 to 60 minutes, it began to deforme. At 0 minute, C_{om} was 1.0. C_{om} was 1.0202, 1.0569, 1.0656, 1.0872, 1.1306, 1.1583, 1.2025, and 1.226 at 5, 10, 15, 25, 35, 45, 55, and 60 minutes, respectively. Fig. 4.5(b) depicts the time course of C_{om}. The time course of average compactness, C_{om}^{av} is depicted in Fig. 4.5(c).

Fig. 4.6(a) shows the phase contrast images of a DOPC/chol (85/15)-GUV due to the interaction of 3.33 µg/mL NPs. The shape of GUV remains spherical before the addition of NPs in the GUV suspension. The shape deformed from spherical with time, indicating value of C_{om} to grow. For the first 14 minutes, the GUV was unchanged, but from 15 to 60 minutes, it began to deform. At 0 minute, C_{om} was 1.0. C_{om} was 1.001, 1.006, 1.0087, 1.0272, 1.0586, 1.0827, 1.1125, and 1.1271 at 5, 10, 15, 25, 35, 45, 55, and 60 minutes, respectively. Fig. 4.6(b) depicts the time course of C_{om}. The time course of average compactness, C_{om}^{av} is depicted in Fig. 4.6(c).
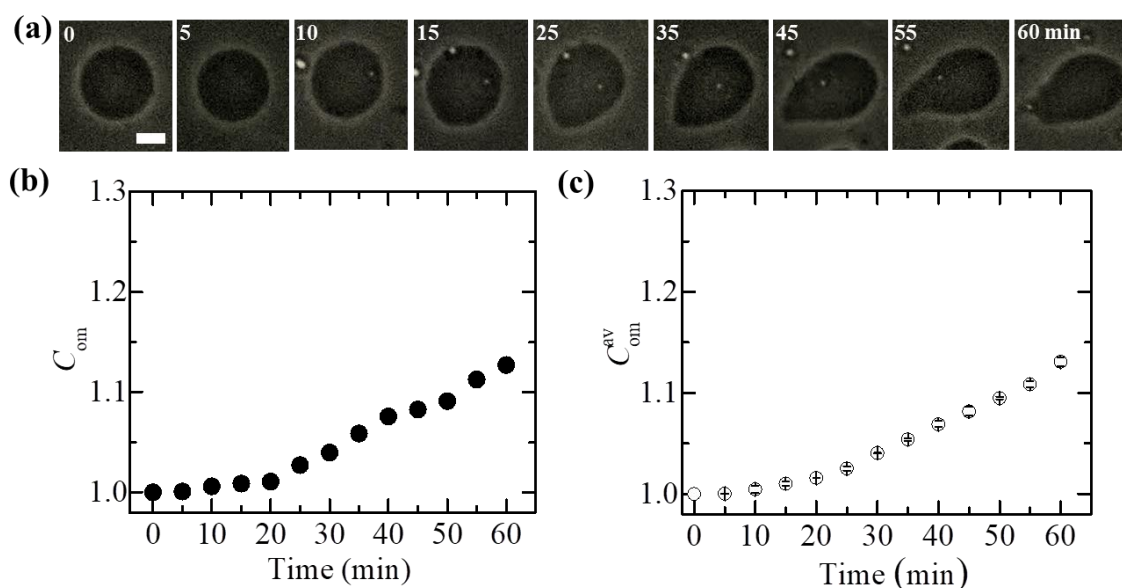
Fig. 4.6 The deformation and the corresponding compactness of DOPC/ chol (85/15)-GUV in the presence of 3.33 µg/mL NPs. (a) Phase contrast images of a single GUV's demonstrate the deformation. The number on each image depicts the time in minutes after the addition of NPs. Scale bar is 15 µm. (b) The time dependent compactness, C_{om}, of the GUV as shown in (a). (c) The time dependent average compactness, C_{om}^{av} of several GUVs under the same conditions as shown in (a).

The representative phase contrast images of a DOPC/chol (71/29)-GUV upon the interaction of 3.33 µg/mL NPs is shown in Fig. 4.7(a). Before the NPs were added into the GUV suspension, GUV was spherical in shape. With time, the shape deformed from spherical shape, demonstrating C_{om}'s value to rise. The GUV was unchanged for the first 9 minutes, but from 10 to 60 minutes, it began to deform. C_{om} was 1.0 at 0 minute. At 5, 10, 15, 25, 35, 45, 55, and 60 minutes, C_{om} was 1.0, 1.001, 1.0086, 1.0266, 1.0423, 1.0728, 1.1023, and 1.1134, respectively. The time course of C_{om} is shown in Fig. 4.7(b). The time course of average compactness, C_{om}^{av} is shown in Fig. 4.7(c).
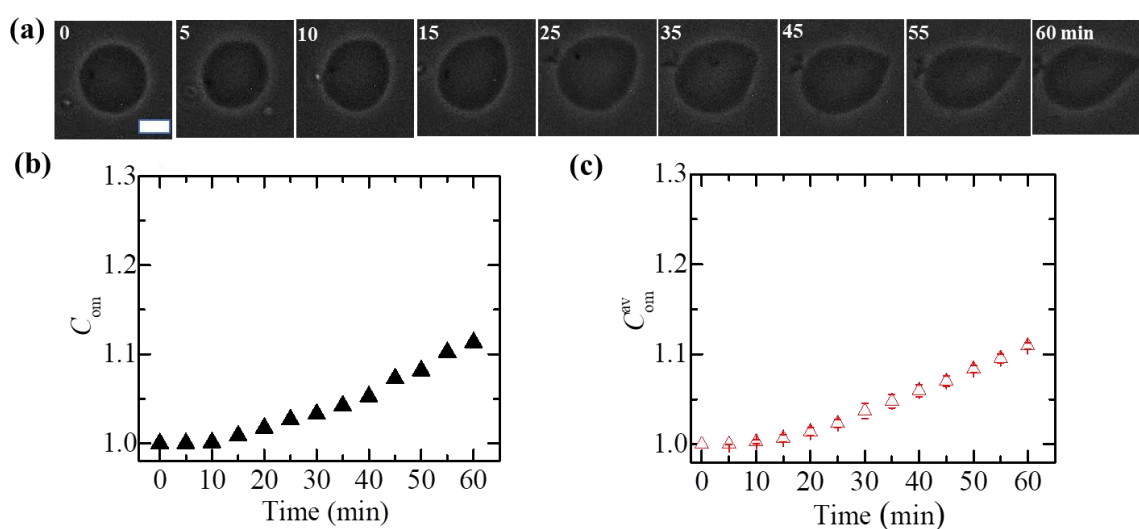
Fig. 4.7 The deformation and the corresponding compactness of DOPC/chol (71/29)-GUV in the presence of 3.33 µg/mL NPs. (a) Phase contrast images of a single GUV's demonstrate the deformation. The number on each image depicts the time in minutes after the addition of NPs. Scale bar is 15 µm. (b) The time dependent compactness, C_{om}, of the GUV as shown in (a). (c) The time dependent average compactness, C_{om}^{av} of several GUVs under the same conditions as shown in (a).

The phase contrast images of a DOPC/chol (60/40)-GUV due to the interaction of 3.33 µg/mL NPs is shown in Fig. 4.8(a). GUV was spherical in shape before the addition of NPs. The shape changed from spherical to deformed GUV over time, indicating the value of C_{om} to rise. The GUV remains unchanged for the first 14 minutes before attaing the significant deformation from 15 to 60 minutes. C_{om} was 1.0 at 0 minute. At 5, 10, 15, 25, 35, 45, 55, and 60 minutes, the values of C_{om} were 1.0, 1.0008, 1.0085, 1.0159, 1.0337, 1.0676, 1.1055, and 1.1055, respectively. The time course of C_{om} is shown in Fig. 4.8(b).

The time course of average compactness, C_{om}^{av} is shown in Fig 4.8(c). The values of average compactness for different neutral membranes at 60 minutes are presented in Table 4.2.
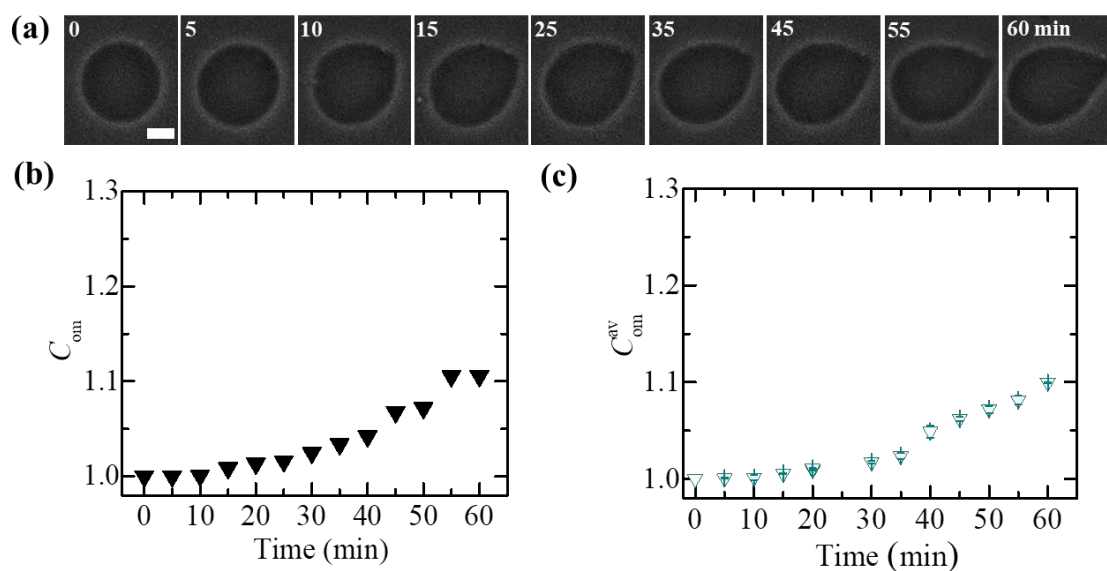
Fig. 4.8 The deformation and the corresponding compactness of DOPC/chol (60/40)-GUV in the presence of 3.33 µg/mL NPs. (a) Phase contrast images of a single GUV's demonstrate the deformation. The number on each image depicts the time in minutes after the addition of NPs. Scale bar is 15 µm. (b) The time dependent compactness, C_{om}, of the GUV as shown in (a). (c) The time dependent average compactness, C_{om}^{av} of several GUVs under the same conditions as shown in (a).

Table 4.2 Average compactness of different neutral DOPC/chol GUVs at 60 minute

Sample	Chol (%)	Average Compactness, C_{om}^{av}
100/0	0	1.2691 ± 0.0089
85/15	15	1.1309 ± 0.0043
71/29	29	1.1094 ± 0.0037
60/40	40	1.0995 ± 0.0045

4.3 Comparison of the Compactness of DOPG/DOPC/chol-GUVs and DOPC/chol-GUVs

The change in average compactness, C_{om}^{av} in the membrane of DOPG/DOPC/chol-GUVs for 0, 15, 29, and 40% chol is shown in Fig. 4.9(a). The values of C_{om}^{av} decrease with the increase of cholesterol content in the charged membranes. For 0, 15, 29, and 40% chol, the values of C_{om}^{av} at 60 minutes were 1.280 ± 0.002, 1.269 ± 0.022, 1.154 ± 0.022, and 1.131 ± 0.010, respectively.
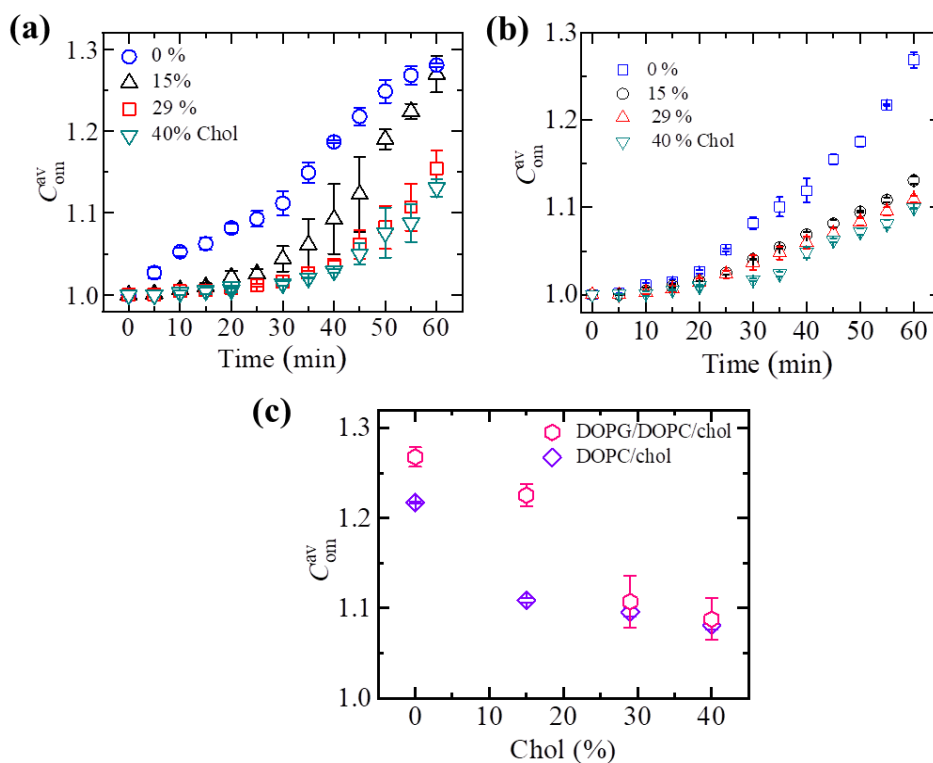
Fig. 4.9 Compactness of DOPG/DOPC/chol-GUVs and DOPC/chol-GUVs induced by 3.33 µg/mL NPs. Time courses of average compactness, C_{om}^{av} of (a) DOPG/DOPC/chol-GUVs and (b) DOPC/chol-GUVs for 0, 15, 29, and 40% chol. (c) The cholesterol-dependent C_{om}^{av} at 55 minutes for charged and neutral GUVs. Three different investigations with a total of 21-27 GUVs were used to calculate the average values with standard deviations.

For various cholesterol containing neutral membranes, the time-dependent C_{om}^{av} is interpreted in Fig. 4.9(b). For example, C_{om}^{av} value for DOPC/chol (60/40)-GUVs was 1.099 ± 0.005, 1.109 ± 0.004 for DOPC/chol (71/29)-GUVs, 1.131 ± 0.004 for DOPC/chol (85/15)-GUVs, and 1.269 ± 0.009 for DOPC/chol (100/0)-GUVs at 60 minutes. As presented in Fig. 4.9(c), the average compactness of neutral and charged membranes

decreased as cholesterol increased in the membranes of vesicles. In the presence of NPs, cholesterol reduced deformation for both types of vesicles, according to these studies. Charged vesicles have a greater average compactness than neutral ones (Fig. 4.9c). Hence, anionic magnetite NPs has a considerable effect on a variety of cholesterol contained GUVs, both neutral and charged.

4.4 Fraction of Deformation of DOPG/DOPC/chol-GUVs

The interaction of NPs with charged and neutral GUVs comprising of different cholesterol containing membranes was described in sections 4.1 – 4.9. These sections discussed the interaction of NPs with a 'single GUV'. Here, the results of 3.33 μg/mL NPs interaction with an ensemble of GUVs are shown. Both the deformed and intact GUVs were found with the addition of NPs to the vesicle suspension shown in Fig. 4.10.
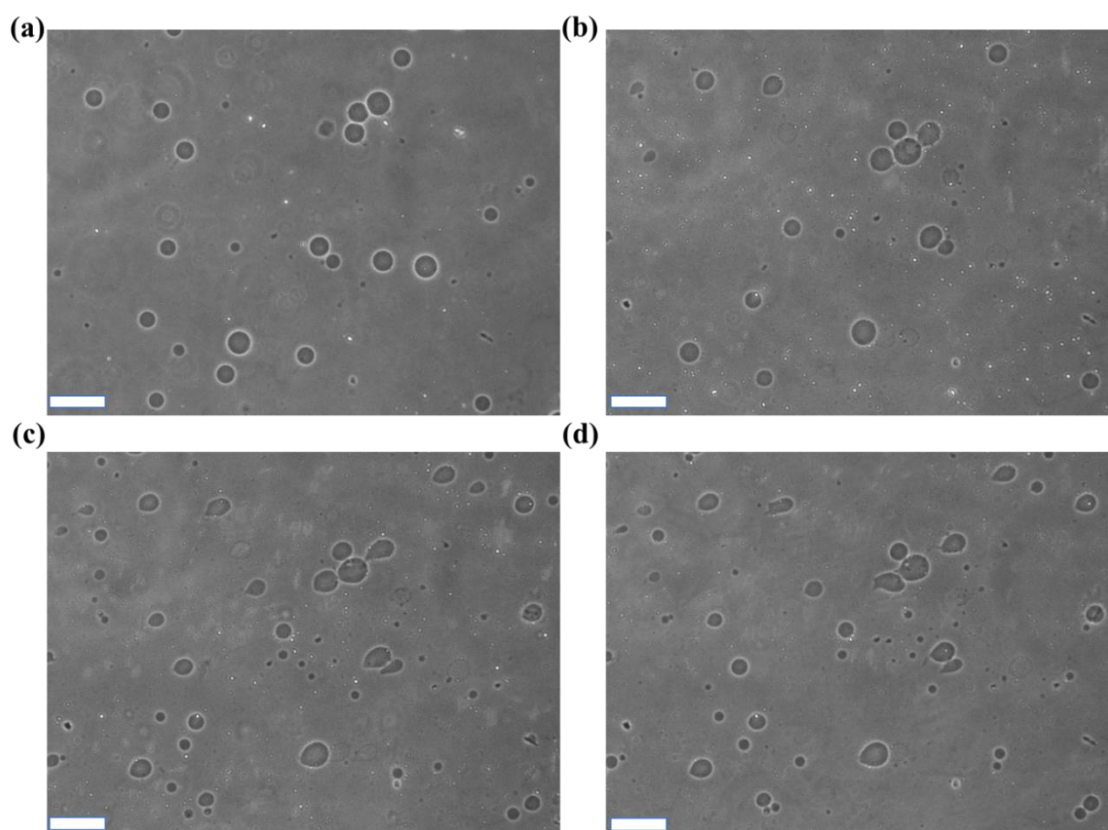
Fig. 4.10 The deformed and un-deformed DOPG/DOPC/chol-GUVs with the addition of 3.33 μg/mL NPs. (a) 0 minute, (b) 10 minute, (c) 40 minute, and (d) 60 minute. The scale bar is 50 μm.

To look into the fraction of deformed GUVs (Fr_d), we first put the NPs concentration in a suspension of DOPG/DOPC/chol (46/39/15)-GUVs into a special chamber. GUV images were taken in a fixed focal position at 0, 10, 20, 30, 40, 50, and 60 minutes. We regarded these observations as an independent experiment (i.e. $n = 1$).

The similar analysis was carried out in the second and third independent experiments (i.e. total independent experiment was $n = 3$) and the fraction of deformed GUVs were calculated from the values of 3 independent experiments at the specified point. From several images taken at different times, the amount of GUVs with deformed was counted among all the examined GUVs ($N = 40$-50, were the number of examined GUVs). For example, if 40 single GUVs were counted from several images at 20 minutes, and 10 GUVs were determined to be deformed, the value of Fr_d at that time would be 0.25. For various times, we calculated Fr_d. These researches were classified as separate experiments. Three independent experiments were carried out using the same approach. Fig. 4.11(a) shows the time-dependent average value of Fr_d at each defined time, which increased over time. At 0, 10, 20, 30, 40, 50, and 60 minutes, the average value with standard deviation of Fr_d was 0, 0.15 ± 0.02, 0.22 ± 0.03, 0.29 ± 0.04, 0.40 ± 0.01, 0.48 ± 0.02, and 0.50 ± 0.04, respectively as shown in Fig. 4.11(a). As a result, it is evident that the average value of fraction of deformed GUVs, Fr_d, increased with time.

We carried out the similar type of experiments for a variety of cholesterol concentrations, such as 0, 15, 29 and 40%. The time-dependent bar diagram for the average Fr_d at 3.33 µg/mL under various cholesterol concentrations is shown in Fig. 4.11(b) and the average fraction of deformed GUVs were calculated from the values of 3 independent experiments using 40 – 50 GUVs in an independent experiment at the specified point. The average Fr_d dropped as the cholesterol concentration in the charged membranes increased. Fig. 4.11(c) shows the cholesterol-dependent average Fr_d for DOPG/DOPC/chol-GUVs at various intervals. Fr_d values at 60 minutes were (0.63 ± 0.02) for 0% cholesterol, (0.50 ± 0.00) for 15% cholesterol, (0.43 ± 0.01) for 29% cholesterol, and (0.24 ± 0.01) for 40% cholesterol. The average Fr_d dropped as the cholesterol concentration in the charged membranes increased, fig. 4.11(c)'s tendency is very similar to fig. 4.11(b), which demonstrating that cholesterol impedes the fragment of deformed GUVs.

(a)

(b)

(c)
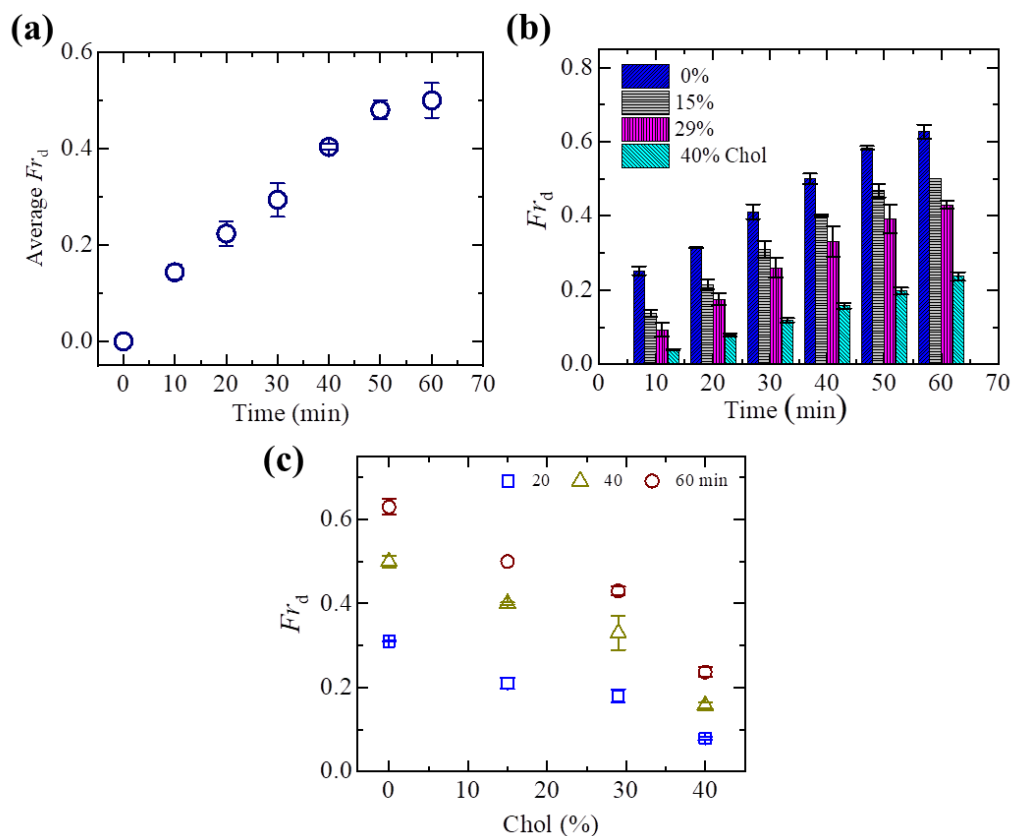
Fig. 4.11 Fraction of deformed (Fr_d) DOPG/DOPC/chol-GUVs in the presence of NPs concentration of 3.33 μg/mL. (a) Average Fr_d of DOPG/DOPC/chol (46/39/15)-GUVs over time for three different experiments. (b) A bar graph depicting the average Fr_d over time for various cholesterol concentrations. (c) Cholesterol dependent the values of Fr_d, at 20, 40, and 60 minutes. The average values with standard deviations were calculated from three different experiments, each of which used 20-25 GUVs.

4.5 Fraction of Deformation of DOPG/DOPC/chol (46/39/15)-GUVs in the Presence of Various Concentrations of NPs

We employed different NPs concentrations to better understand the interaction trend. Fig. 4.12(a) shows a time-dependent bar graph of average Fr_d of DOPG/DOPC/chol (46/39/15)-GUVs at concentrations of 2.00, 3.33, and 4.70 μg/mL NPs. The increasing trend of deformation with time is observed in all concentrations. Fig. 4.12(b) depicts the NPs concentration-dependent average values Fr_d for various times. The value of Fr_d was 0.43 ± 0.01 for 2.00 μg/mL NPs, 0.47 ± 0.01 for 3.33 μg/mL NPs, and 0.62 ± 0.02 for 4.70 μg/mL NPs at 50 minutes. According to these findings, the fraction of deformation at any given time is dependent on the concentration of NPs interacting with vesicles.
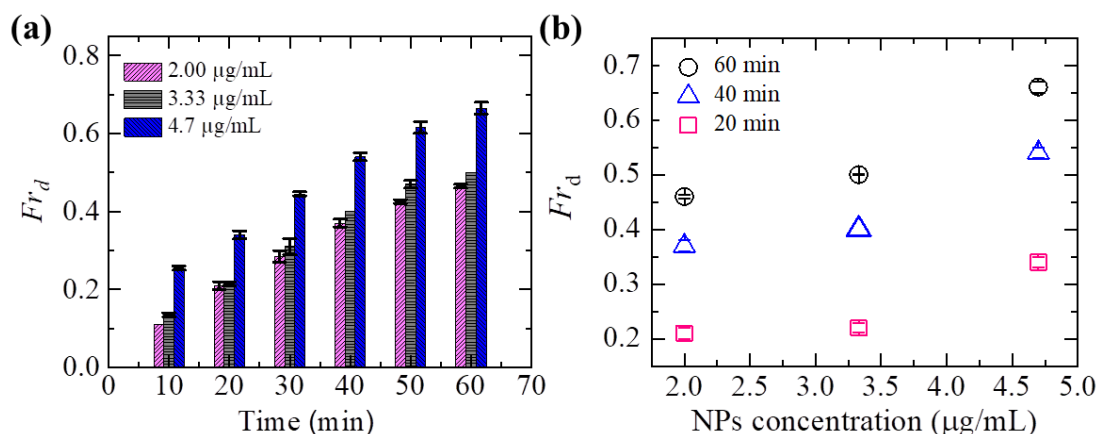
Fig. 4.12 Fraction of deformed DOPG/DOPC/chol (46/39/15)-GUVs in the presence of different NPs concentrations, (a) The time course of the fraction of deformed GUVs at 2.00, 3.33, and 4.7 μg/mL NPs as a bar graph. (b) The NPs concentrations dependent fraction of deformed GUVs at 20, 40, and 60 minutes. The average values with standard deviations were calculated from three different experiments, each of which used 20-25 GUVs.

4.6 Encapsulated Calcein Leakage of DOPG/DOPC/chol-GUVs in the presence of 3.33 μg/mL NPs

The results of water-soluble fluorescent probe, calcein, releases from the DOPG/DOPC/chol (70/30/0)-GUV's interior are presented here. Fig. 4.13(a) depicts a representative empirical outcome of NPs at 3.33 μg/mL interacted with a DOPG/DOPC/chol (70/30/0)-GUV. GUV exhibits a strong contrast in an inverted phase contrast microscopic picture at 0 s (i.e., in the absence of NPs) of Fig. 4.13(a(i)) due to the distinction in refractive indices between the inside sucrose and outer glucose solution of a GUV. The same GUV is shown in a fluorescence microscopic image in Fig. 4.13(a(ii)), with a high contrast of calcein inside the vesicle. The fluorescence intensity within the GUV remained same until 20 s after adding NPs solution to the vesicle suspension, after which it rapidly decreased as seen in Fig. 4.13(a(ii)). The fluorescence intensity declined by a modest amount from 20 to 47 seconds, and then rapidly decreased to zero at 48 seconds. Within 1 second, the fluorescence intensity was nil. The phase contrast image (Fig. 4.13a(iii)) shows the same GUV. It means that GUV is still intact and hasn't been broken. The swift diminution in fluorescence intensity is comparable to that seen in peptide-induced fluorescent probe leakage [146, 34]. The size of such pores was so small

that the vesicles were intact with spherical structure after injecting the internal calcein. Fig. 4.13(b) depicts the change in normalized fluorescence intensity over time. There was no calcein leakage as long as the normalized fluorescence intensity in the GUV lumen was 1.0 (or close to 1.0). On the other hand, a rapid reduction in normalized fluorescence intensity implies pore formation. A similar study was conducted with several GUVs, and a similar decrease in fluorescence intensity was found. In Fig. 4.13(c), we show 5 separate DOPG/DOPC/chol (70/30/0)-GUVs under 3.33 μg/mL NPs. Fig. 4.13(c) depicts the stochastic nature of pore formation. It means that pore formation occurred at different times for several similar sized GUVs, even though the NPs concentration is the same. The average time of poration was calculated from the calculation of 16 GUVs.

Fig. 4.13 The calcein leakage from DOPG/DOPC/chol (70/30/0)-GUVs due to the interaction of 3.33 μg/mL NPs. (a) Phase contrast (i and iii) and fluorescence (ii) images demonstrates how calcein changes within the GUV. The time in seconds after the addition of NPs in the GUVs suspension is shown by the number on each image. The scale bar is 15 μm. (b) The time dependent change in normalized fluorescence intensity inside of GUV, as indicated in (a). The inset displays the rapid change in fluorescence intensity with time. (c) The variation in normalized fluorescence intensity for 5 different GUVs under the same conditions as in (b).

The interaction of 3.33 μg/mL NPs with a DOPG/DOPC/chol(46/39/15)-GUV is shown in Fig. 4.14(a). In the absence of NPs, Fig. 4.14(a(i)) illustrates an inverted phase contrast

microscopic image, while Fig. 4.14(a(ii)) illustrates a fluorescence microscopic image of the equivalent GUV with a strong contrast of calcein inside the vesicle. After adding NPs solution to the vesicle suspension, the fluorescence intensity inside the GUV remained constant for 40 s before rapidly decreasing as shown in Fig. 4.14(a(ii)). From 40 to 67 seconds, the fluorescence intensity fell gradually before dropping quickly to zero at 68 seconds. The fluorescence intensity dissipated in less than a second. The identical GUV is visible in the phase contrast image (Fig. 4.14a(iii)). It indicates that GUV is still intact and unbroken. The variation in normalized fluorescence intensity across time is seen in Fig. 4.14(b).

Fig. 4.14 The calcein leakage from DOPG/DOPC/chol(46/39/15)-GUVs due to the interaction of 3.33 μg/mL NPs. (a) Phase contrast (i and iii) and fluorescence (ii) images demonstrates how calcein changes within the GUV. The time in seconds after the addition of NPs in the GUVs suspension is shown by the number on each image. The scale bar is 15 μm. (b) The time dependent change in normalized fluorescence intensity inside of GUV, as indicated in (a). The inset displays the rapid change in fluorescence intensity with time. (c) The variation in normalized fluorescence intensity for 5 different GUVs under the same conditions as in (b).

We provide the results of 5 separate DOPG/DOPC/chol(46/39/15)-GUV s under 3.33 μg/mL NPs in Fig. 4.14(c). The stochastic nature of pore growth is shown in Fig. 4.14(c). It indicates that, despite the identical NPs concentration, pore formation took place at

varied times for various DOPG/DOPC/chol(46/39/15)-GUVs of equal size. The average time of poration was calculated from the calculation of 16 GUVs.

Fig. 4.15(a) shows the interaction 3.33 μg/mL NPs with a DOPG/DOPC/chol (43/28/29)-GUV. Fig. 4.15(a(i)) exhibits an inverted phase contrast microscopic images of the same GUV in the absence of NPs, while Fig. 4.15(a(ii)) exhibits fluorescence microscopic images of the same GUV with a striking contrast of calcein inside the vesicle.

Fig. 4.15 The calcein leakage from DOPG/DOPC/chol (43/28/29)-GUVs due to the interaction of 3.33 μg/mL NPs. (a) Phase contrast (i and iii) and fluorescence (ii) images demonstrates how calcein changes within the GUV. The time in seconds after the addition of NPs in the GUVs suspension is shown by the number on each image. The scale bar is 15 μm. (b) The time dependent change in normalized fluorescence intensity inside of GUV, as indicated in (a). The inset displays the rapid change in fluorescence intensity with time. (c) The variation in normalized fluorescence intensity for 5 different GUVs under the same conditions as in (b).

The fluorescence intensity inside the GUV remained unchanged for 55 s after injecting NPs solution to the vesicle suspension before abruptly dropping, as illustrated in Fig. 4.15 (a(ii)). The fluorescence intensity decreased progressively from 55 to 81 seconds before abruptly ceasing at 82 seconds. In less than a second, the fluorescence's intensity diminished. The phase contrast image (Fig. 4.15a(iii)) exhibits the same GUV. It implies

that GUV is still unbroken and intact. Fig. 4.15(b) depicts the variation in normalized fluorescence intensity with time. In Fig. 4.15(c), we present the results of 5 distinct DOPG/DOPC/chol (43/28/29)-GUVs with NPs concentration of 3.33 μg/mL. Fig. 4.15(c) illustrates the stochastic nature of pore formation. It shows that different DOPG/DOPC/chol (43/28/29)-GUVs of equivalent size experienced pore formation at different times despite having the same concentration of NPs. The average time of poration was calculated from the calculation of 16 GUVs.

The interaction of 3.33 μg/mL NPs with DOPG/DOPC/chol (40/20/40)-GUV is presented in Fig. 4.16 (a). The same GUV is shown in Fig. 4.16(a(i)) using an inverted phase contrast microscopic image in the absence of NPs, while Fig. 4.16(a(ii)) presents the same GUV in a fluorescence microscopic image with a remarkable contrast of calcein inside the vesicle. After adding NPs solution into the vesicle suspension, the fluorescence intensity inside the GUV unchanged for 70 s before suddenly decreasing, as shown in Fig. 4.16(a(ii)). From 70 to 95 seconds, the fluorescence intensity gradually declined before ending entirely at 96 seconds. The intensity of the fluorescence decreased in less than a second. The equivalent GUV can be seen in the phase contrast image (Fig. 4.16a(iii)). It suggests that the GUV is still intact and unbroken. The normalized fluorescence intensity over time is shown in Fig. 4.16(b). We have presented 5 different DOPG/DOPC/chol (40/20/40)-GUVs with NPs concentration of 3.33 μg/mL in Fig. 4.16(c). The stochastic nature of pore formation is shown in Fig. 4.16(c). It demonstrates that while having the same NP concentration, pore formation occurred at different times in various DOPG/DOPC/chol (40/20/40)-GUVs of equal size. The average time of poration was calculated from the calculation of 16 GUVs.
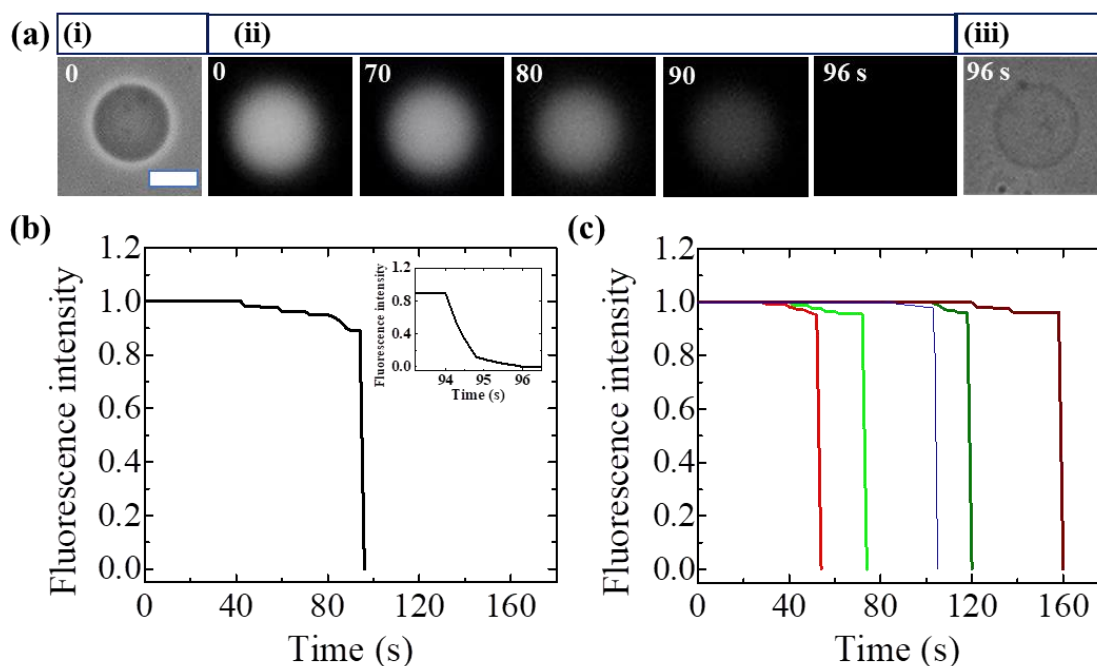
Fig. 4.16 The calcein leakage from DOPG/DOPC/chol (40/20/40)-GUVs due to the interaction of 3.33 μg/mL NPs. (a) Phase contrast (i and iii) and fluorescence (ii) images demonstrates how calcein changes within the GUV. The time in seconds after the addition of NPs in the GUVs suspension is shown by the number on each image. The scale bar is 15 μm. (b) The time dependent change in normalized fluorescence intensity inside of GUV, as indicated in (a). The inset displays the rapid change in fluorescence intensity with time. (c) The variation in normalized fluorescence intensity for 5 different GUVs under the same conditions as in (b).

4.7 Encapsulated Calcein Leakage of DOPC/chol-GUVs in the presence of 3.33 μg/mL NPs

We also looked into calcein releases from the interior of neutral GUVs such DOPC/chol (100/0)-GUVs to see if the leakage followed the same pattern as charged vesicles. A sample empirical outcome of the effect of NPs at 3.33 μg/mL with a DOPC/chol (100/0)-GUV is exhibits in Fig. 4.17(a). Fig. 4.17(a(i)) exhibits the spherical shaped GUV in a phase contrast image at 0 s without NPs in the suspension of vesicles. The same GUV is shown in a fluorescence microscopic image in Fig. 4.17(a(ii)), with a sharp contrast of calcein within the vesicle. Following the addition of NPs solution to the GUV suspension, the fluorescence intensity inside the GUV remained nearly steady for the first 39 seconds, before rapidly decreasing at 40 seconds.
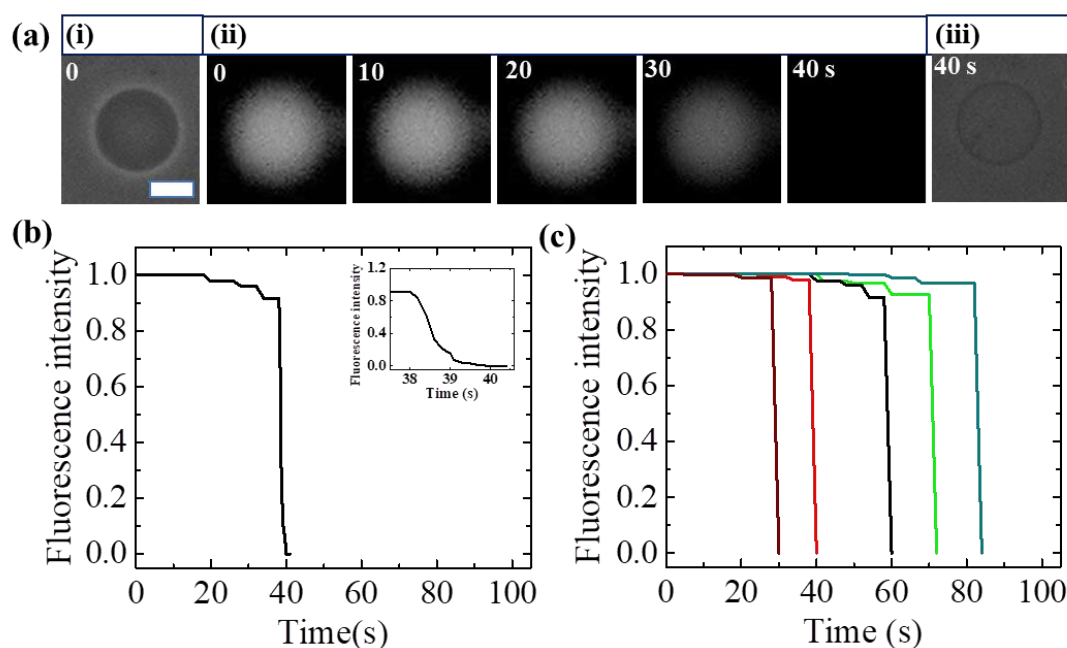
Fig. 4.17 The calcein leakage from DOPC/chol (100/0)-GUVs due to the interaction of 3.33 µg/mL NPs. (a) Phase contrast (i and iii) and fluorescence (ii) images demonstrates how calcein changes within the GUV. The time in seconds after the addition of NPs in the GUVs suspension is shown by the number on each image. The scale bar is 15 µm. (b) The time dependent change in normalized fluorescence intensity inside of GUV, as indicated in (a). The inset displays the rapid change in fluorescence intensity with time. (c) The variation in normalized fluorescence intensity for 5 different GUVs under the same conditions as in (b).

Within 1 second, the fluorescence intensity was nil. In the phase contrast image of Fig. 4.17(a(iii)), the GUV with undetectable break is seen. Fig. 4.17(b) depicts the progression of the GUV's normalized intensity change over time. Several DOPC/chol-GUVs showed stochastic pore formation, similar to charged GUVs. It demonstrates that while having the same NP concentration, pore formation occurred at different times in various DOPC/chol (100/0)-GUVs of equal size. The average time of poration was calculated from the calculation of 16 GUVs. We illustrate five different DOPC/chol (100/0)-GUVs with NPs concentration of 3.33 µg/mL in Fig. 4.17(c). The average time of poration was calculated from the calculation of 16 GUVs.

Fig. 4.18(a) shows a representative findings of the interaction of NPs at 3.33 µg/mL with a DOPC/chol (85/15)-GUV. The spherical GUV is depicted in a phase contrast image at 0

second in absence of NPs in the suspension of vesicles in Fig. 4.18(a(i)). A fluorescence microscopic image of the similar GUV with a great contrast of calcein inside the vesicle can be seen in Fig. 4.18(a(ii)). The fluorescence intensity inside the GUV stayed relatively the same for the first 58 seconds since the insertion of NPs solution before significantly declining at 59 seconds. The fluorescence intensity vanished in less than a second. The GUV with undetectable break is visible in the phase contrast image of Fig. 4.18(a(iii)). The standardized luminosity variation of the GUV is shown as a time series in Fig. 4.18(b). Similar to charged GUVs, a number of DOPC/chol-GUVs demonstrated stochastic pore formation. It demonstrates that while having the same NP concentration, pore formation occurred at different times in various DOPC/chol(100/0)-GUVs of equal size. The average time of poration was calculated from the calculation of 16 GUVs. In Fig. 4.18(c), we present five distinct DOPC/chol(85/15)-GUVs at a concentration of 3.33 µg/mL NPs. The average time of poration was calculated from the calculation of 16 GUVs.
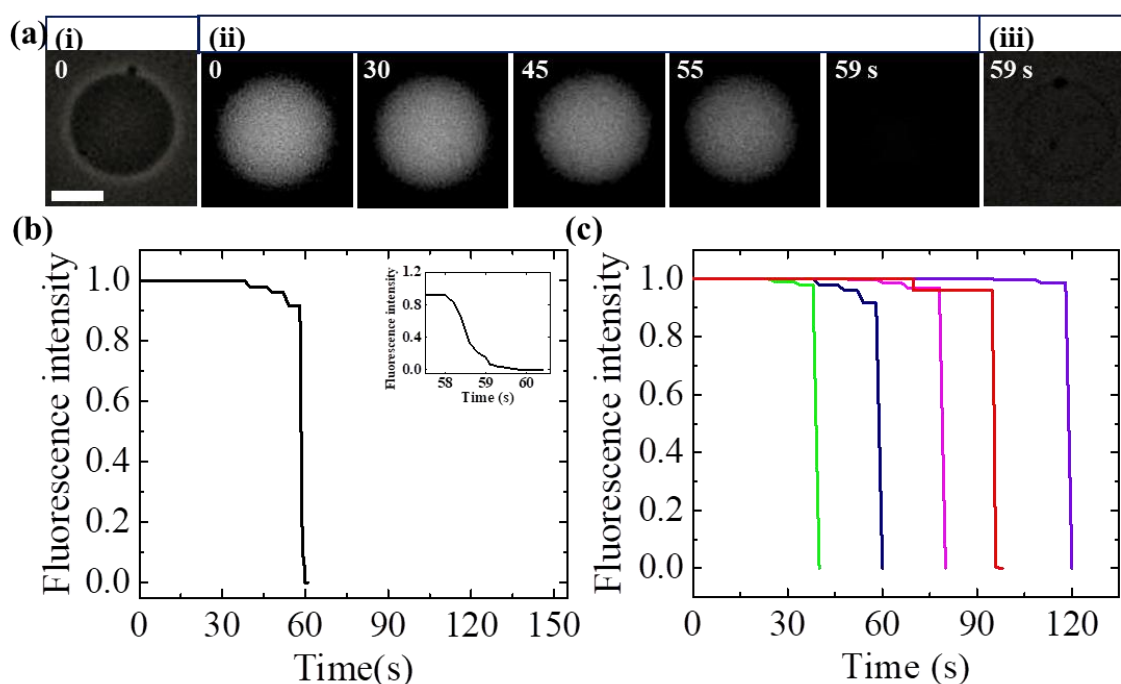
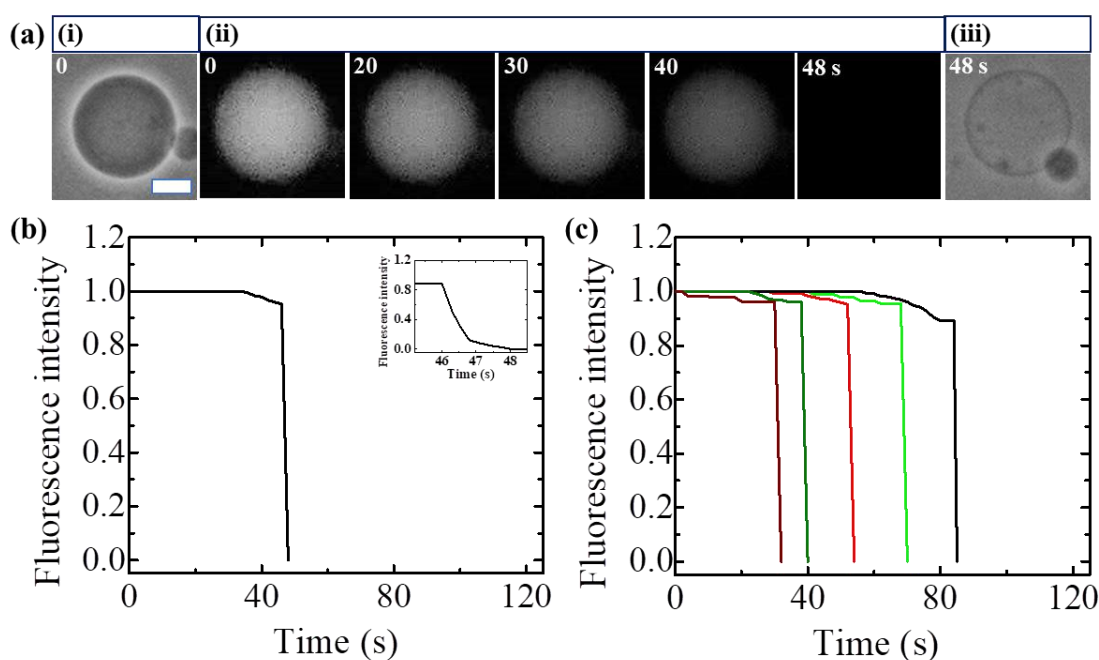**Fig. 4.18** The calcein leakage from DOPC/chol(85/15)-GUVs due to the interaction of 3.33 µg/mL NPs. (a) Phase contrast (i and iii) and fluorescence (ii) images demonstrates how calcein changes within the GUV. The time in seconds after the addition of NPs in the GUVs suspension is shown by the number on each image. The scale bar is 15 µm. (b) The time dependent change in normalized fluorescence intensity inside of GUV, as indicated in (a). The inset displays the rapid change in fluorescence intensity with time. (c) The variation in normalized fluorescence intensity for 5 different GUVs under the same conditions as in (b).

The results of the interaction of 3.33 µg/mL NPs with a DOPC/chol(71/29)-GUV is shown in Fig. 4.19(a). Fig. 4.19(a(i)) presents a phase contrast image at 0 second of the spherical GUV absent of NPs in the suspension of vesicles. Fig. 4.19(a(ii)) shows a fluorescence microscopic image of the similar GUV with highly contrasted calcein inside the vesicle. Following the addition of NPs solution, the fluorescence intensity inside the GUV stayed relatively the same for the first 77 seconds before noticeably decreasing at 78 seconds. In about a second, the fluorescence's intensity disappeared. The phase contrast image of Fig. 4.19(a(iii)) indicates the GUV with undetectable break. Fig. 4.19(b) displays a time series of the GUV's normalized luminosity variation. A number of DOPC/chol-GUVs showed stochastic pore formation, just like charged GUVs do. We show five different DOPC/chol (71/29)-GUVs at NPs concentration of 3.33 µg/mL NPs in Fig. 4.19(c). The average time of poration was calculated from the calculation of 16 GUVs.
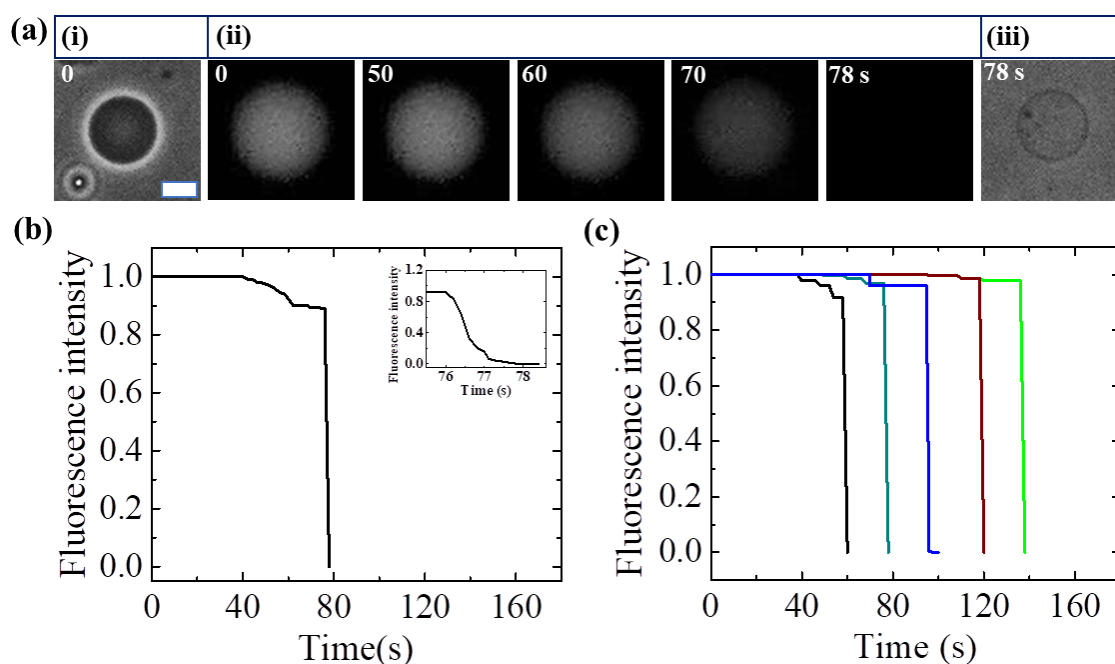
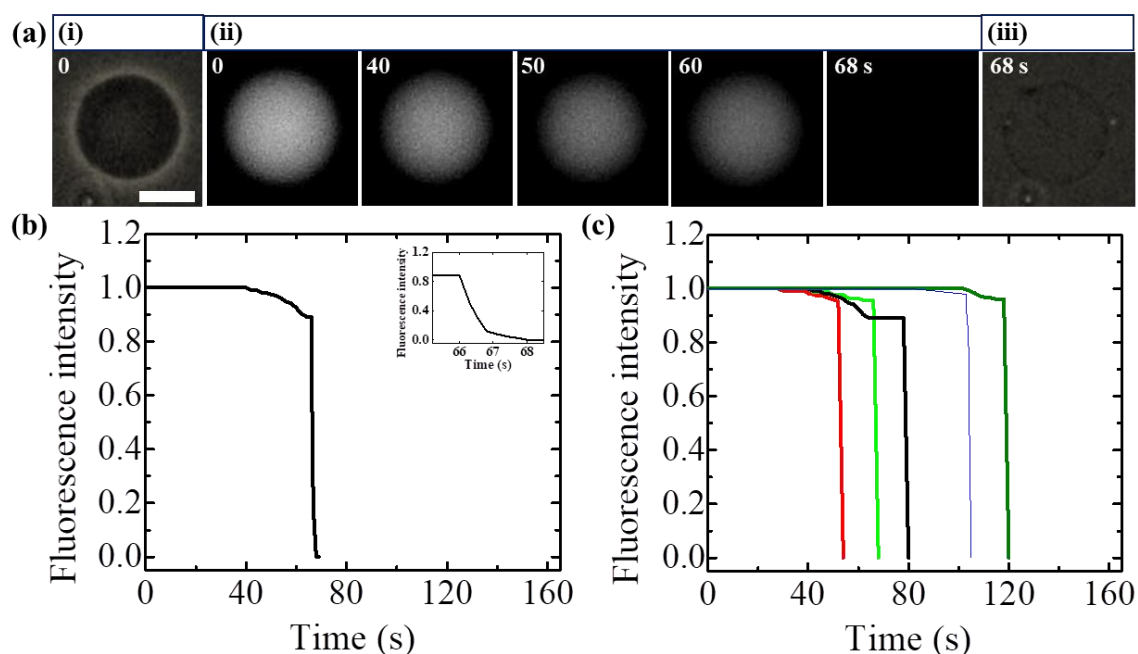**Fig. 4.19** The calcein leakage from DOPC/chol (71/29)-GUVs due to the interaction of 3.33 µg/mL NPs. (a) Phase contrast (i and iii) and fluorescence (ii) images demonstrates how calcein changes within the GUV. The time in seconds after the addition of NPs in the GUVs suspension is shown by the number on each image. The scale bar is 15 µm. (b) The time dependent change in normalized fluorescence intensity inside of GUV, as indicated in (a). The inset displays the rapid change in fluorescence intensity with time. (c) The variation in normalized fluorescence intensity for 5 different GUVs under the same conditions as in (b).

Fig. 4.20(a) shows the interactions of 3.33 µg/mL NPs with a DOPC/chol (60/40)-GUV. A phase contrast image at 0 second of the spherical GUV in the absence of NPs in the suspension of vesicles is exhibited in Fig. 4.20(a(i)). A fluorescence microscopic image of the similar GUV with significantly contrasted calcein inside the vesicle is shown in Fig. 4.20(a(ii)). The fluorescence intensity within the GUV stayed essentially consistent since the addition of the NPs solution for the first 89 seconds before dramatically declining at 90 seconds. The intensity of the luminescence vanished in about a second. The GUV with undetectable break is depicted in the phase contrast image of Fig. 4.20(a(iii)). A time course of the normalized luminosity variation of the GUV is illustrated in Fig. 4.20(b). Like charged GUVs a number of DOPC/chol-GUVs exhibited stochastic pore formation. Fig. 4.20(c) displays five distinct DOPC/chol (60/40)-GUVs at NPs concentration of 3.33 µg/mL. The average time of poration was calculated from the calculation of 16 GUVs.
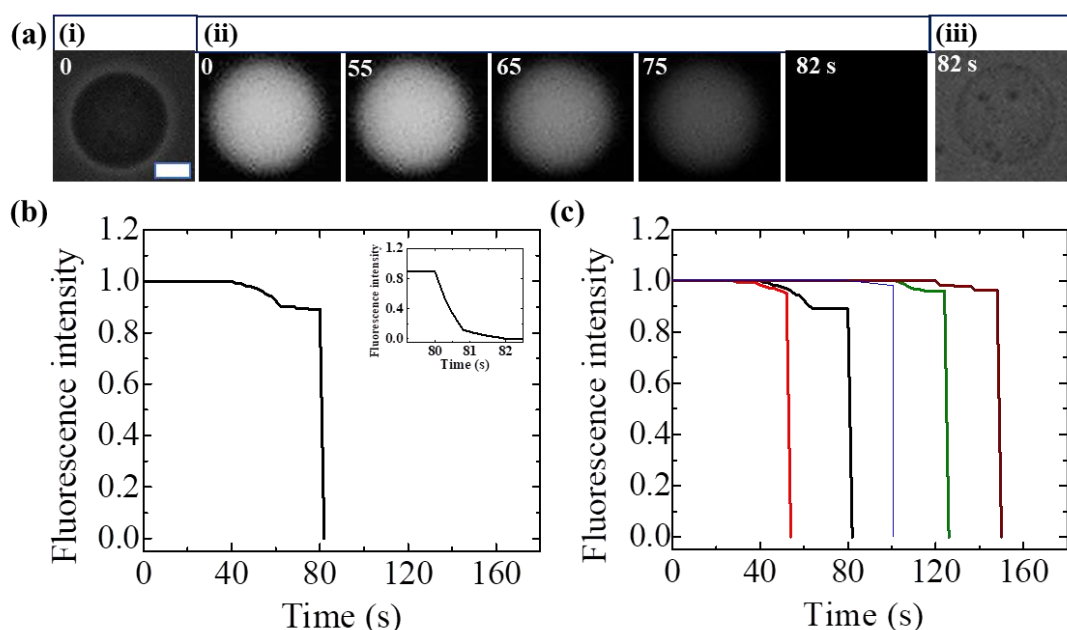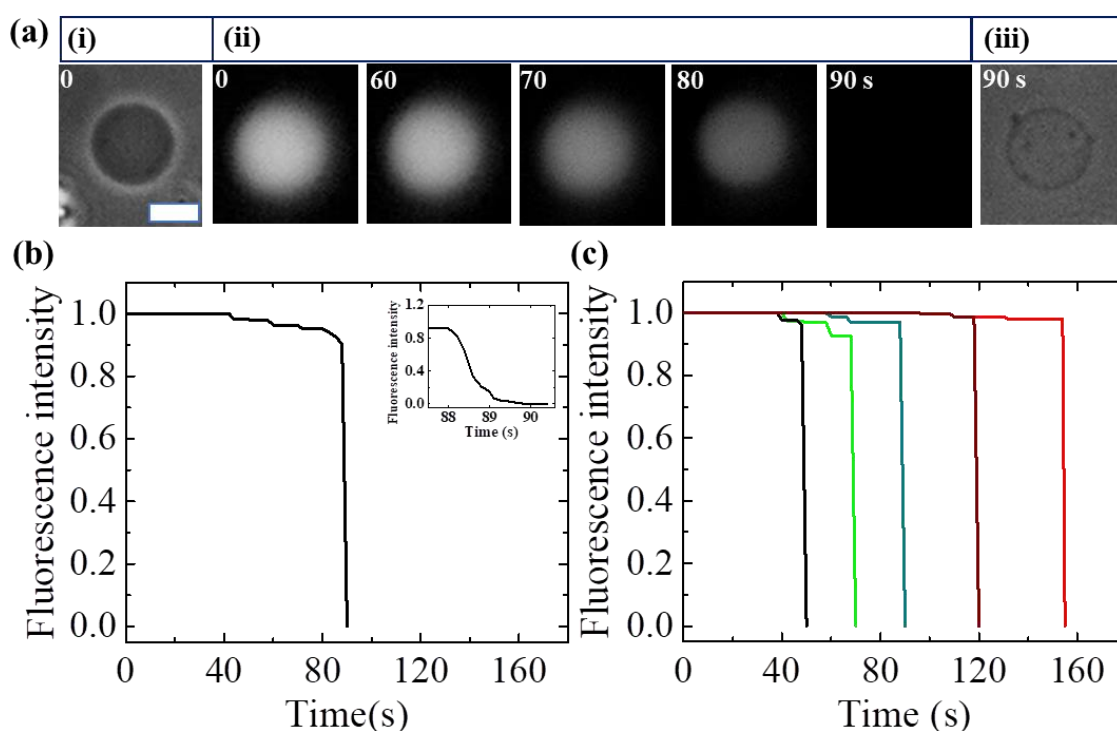

Fig. 4.20 The calcein leakage from DOPC/chol (60/40)-GUVs due to the interaction of 3.33 µg/mL NPs. (a) Phase contrast (i and iii) and fluorescence (ii) images demonstrates how calcein changes within the GUV. The time in seconds after the addition of NPs in the GUVs suspension is shown by the number on each image. The scale bar is 15 µm. (b) The time dependent change in normalized fluorescence intensity inside of GUV, as indicated in (a). The inset displays the rapid change in fluorescence intensity with time. (c) The variation in normalized fluorescence intensity for 5 different GUVs under the same conditions as in (b).

4.8 Comparison of the Average Time of Calcein Leakage of DOPG/DOPC/chol-GUVs and DOPC/chol-GUVs

Under 3.33 μg/mL NPs, we calculated the average time of poration for various cholesterol containing charged and neutral membranes. Fig. 4.21(a) shows the variation in the average time of pore formation in the charged membrane of DOPG/DOPC/chol-GUVs containing 15, 29, and 40% cholesterol in the membranes. The average time of poration increases with the increase of cholesterol content. The variation in the average time of pore formation for different neutral membranes (i.e., DOPC/chol-GUVs) that include 0, 15, 29, and 40% cholesterol is shown in Fig. 4.21(b). With the increases of cholesterol in the neutral membranes, the average time of poration increases in a similar pattern to that seen for charged GUVs.
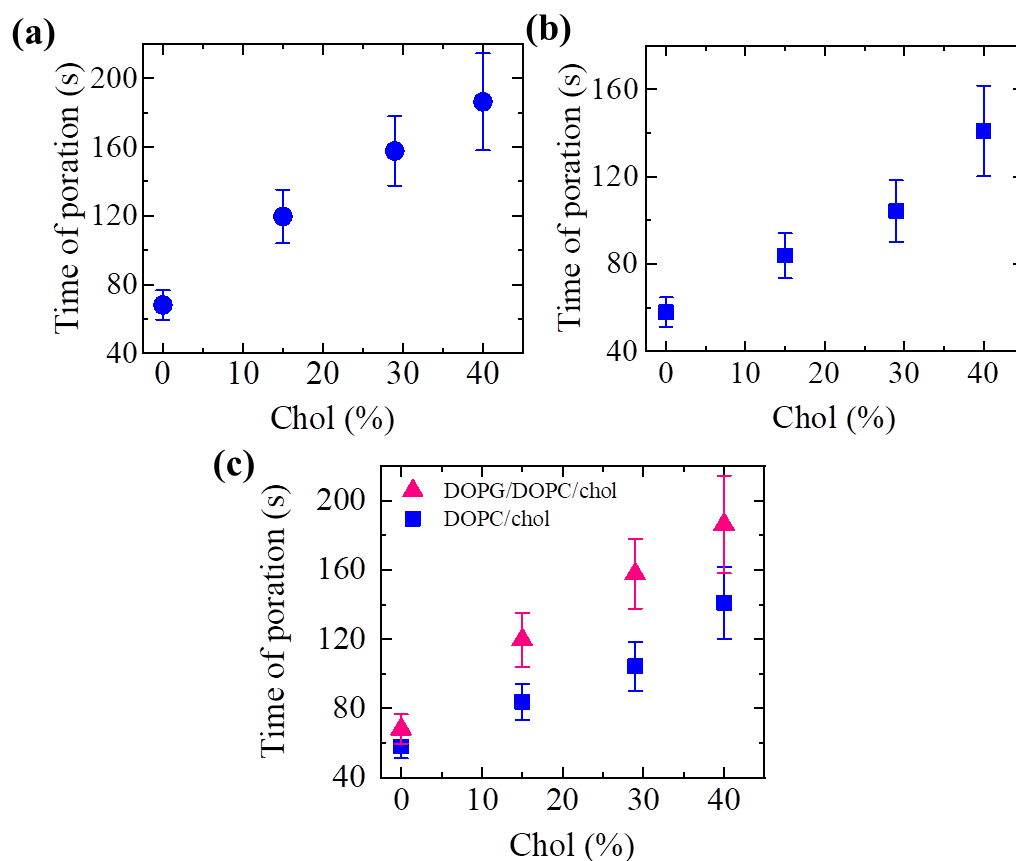
Fig. 4.21 Cholesterol dependent average time of calcein leakage from DOPG/DOPC/chol and DOPC/chol-GUVs due to the interaction of 3.33 μg/mL NPs. Average time of poration of several (a) DOPG/DOPC/chol-GUVs and (b) DOPC/chol-GUVs for 0, 15, 29, and 40% chol. (c) Comparison of the cholesterol dependent average time of poration in neutral and charged GUVs. The average values with standard deviations were yielded from 3 different experiments, each including 22–27 GUVs.

Fig. 4.21(c) depicts the average time for pore formation for different cholesterol containing charged and neutral membranes. For both types of GUVs, the average time of pore formation increased with cholesterol. Based on these findings, an increase in cholesterol concentration in lipid membranes, pore formation in vesicles inhibits. The average period of poration for neutral membranes containing cholesterol is shorter than for charged membranes (Fig. 4.21c).

4.9 Fraction of Deformation and Pore Formation of DOPG/DOPC/chol-GUVs and DOPC/chol-GUVs

In this section, we studied the fraction of deformed GUVs (Fr_d) and the fraction of pore formed GUVs (Fr_p) for various cholesterol containing charged and neutral GUVs. Under 3.33 µg/mL NPs, similar fractions for DOPG/DOPC/chol (46/39/15)-GUVs are shown in Fig. 4.22(a). The value of Fr_d increased until it reached 50 minutes, after which it remained constant. On the other hand, Fr_p increased till 30 minutes and then stayed the same. Fig. 4.22(b) depicts the corresponding portions of DOPG/DOPC/chol (46/39/15)-GUVs that are concentration-dependent on NPs, at 50 minute. As the NPs consistency increased in both cases, the fractions grew. For example, the values of Fr_d and Fr_p at 2.00 µg/mL NPs were 0.29 ± 0.02 and 0.03 ± 0.01, respectively, while at 3.33 µg/mL NPs, they were 0.31 ± 0.02 and 0.13 ± 0.01. Fig. 4.22(c) shows the cholesterol-dependent Fr_d and Fr_p under NPs concentration 3.33 µg/mL at 50 minutes, with both factions decreasing as cholesterol increased.

In order to compare the results with the charged ones, we looked at the fraction of deformed GUVs and the fraction of pore formed GUVs for cholesterol-containing neutral membranes. The change in Fr_d and Fr_p with time for DOPC/chol-GUVs under 3.33 µg/mL NPs is shown in Fig. 4.22(d). Such fractions clearly decreased as the cholesterol level of the DOPC/chol-GUVs increased. Fr_d and Fr_p were 0.32 ± 0.03 and 0.24 ± 0.03, respectively, for DOPC/chol (85/15)-GUVs, whereas these values were 0.18 ± 0.01 and 0.04 ± 0.01, respectively, for DOPC/chol (60/40)-GUVs.
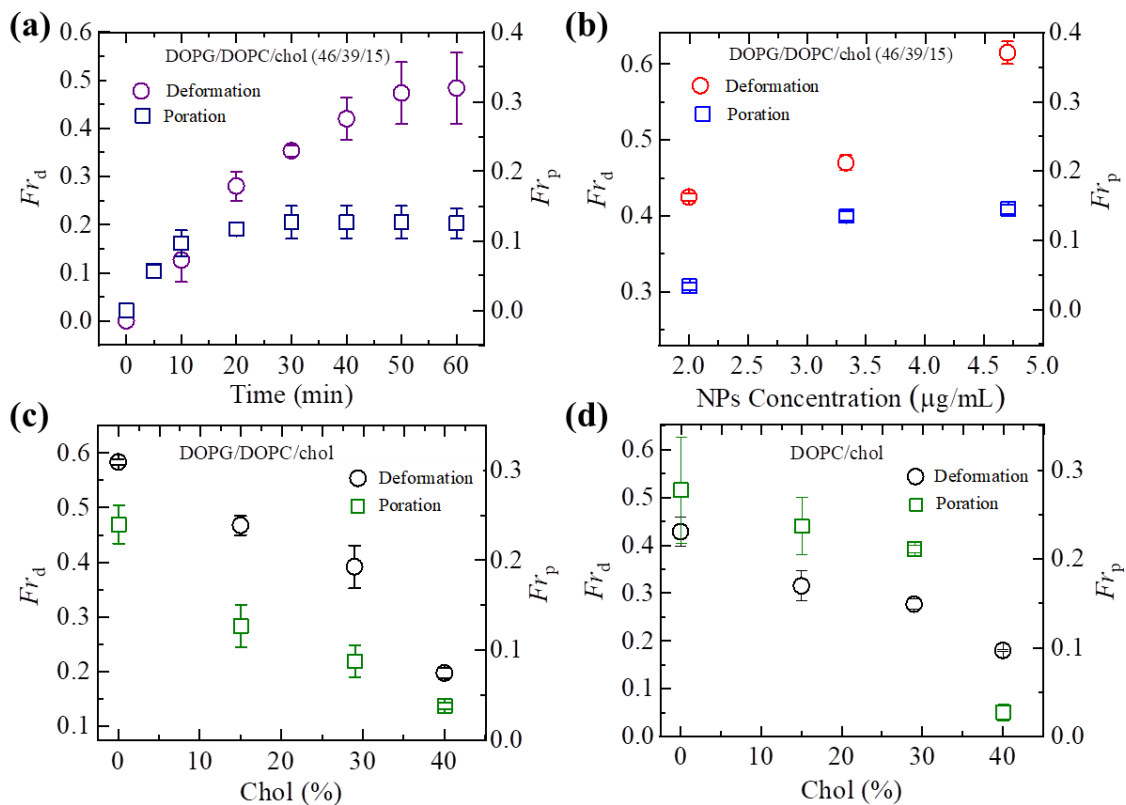
Fig. 4.22 The fraction of deformation and pore formation of charged and neutral GUVs because of the interaction of 3.33 μg/mL NPs. (a) The fraction of deformation and poration in DOPG/DOPC/chol (46/39/15)-GUVs with time. (b) Deformation and poration of DOPG/DOPC/chol (46/39/15)-GUVs at 50 minutes as a function of NP concentration. (c) The cholesterol-dependent deformation and poration of DOPG/DOPC/chol-GUVs at 50 minute. (d) The cholesterol-dependent deformation and poration of DOPC/chol-GUVs at 50 minute. The average values with standard deviations were determined from three different experiments, each of which used 12-27 GUVs.

4.10 Comparison of Fraction of Deformation and Pore Formation Between DOPG/DOPC/chol-GUVs and DOPC/chol-GUVs

In Fig. 4.23, we compared Fr_d and Fr_p of charged DOPG/DOPC/chol and neutral DOPC/chol-GUVs. With the increase of cholesterol, both fractions show a decreasing trend. When comparing cholesterol-containing charged membranes to cholesterol-containing neutral membranes, the Fr_d values are higher (Fig. 4.23a). Fr_p's scenario (Fig. 4.23b) demonstrates the opposite pattern. For example, Fr_d were (0.39 ± 0.04) and (0.28 ± 0.01), respectively, in the cases of DOPG/DOPC/chol (43/28/29)-GUVs and DOPC/chol (71/29)-GUVs. On the other hand, DOPG/DOPC/chol (46/39/15)-GUVs and DOPC/chol

(85/15)-GUVs, had the value of Fr_p (0.13 ± 0.02) and (0.24 ± 0.03), respectively. The values of the fraction of deformation and poration in DOPG/DOPC/chol and DOPC/chol-GUVs at 3.33 µg/mL NPs for 50 minute is presented in Table 4.3.
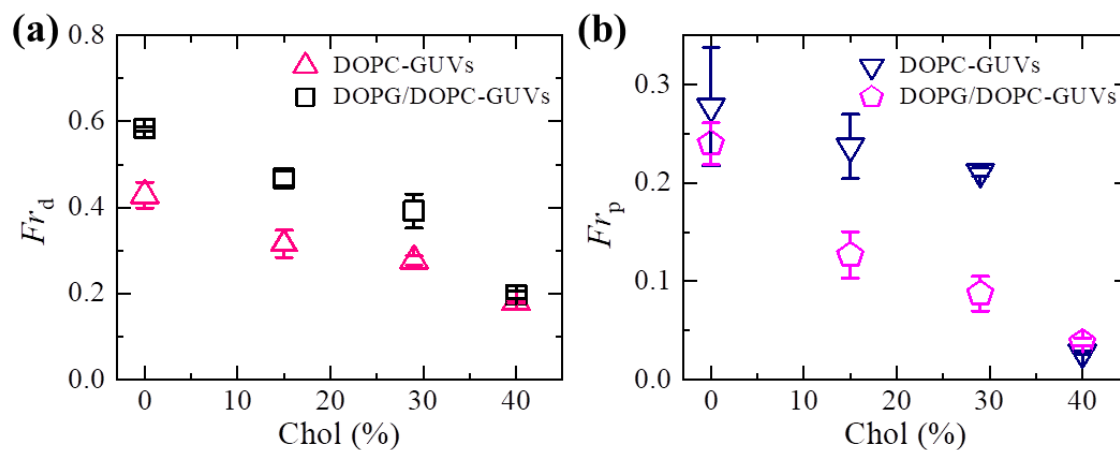
Fig. 4.23 The fraction of deformed and pore formed GUVs at 50 minute. (a) The cholesterol dependent fraction of deformed DOPG/DOPC/chol and DOPC/chol-GUVs. (b) The cholesterol dependent fraction of pore formed DOPG/DOPC/chol and DOPC/chol-GUVs. The average values with standard deviations were computed from three different experiments, each of which used 12-27 GUVs.

Table 4.3 Fraction of deformation and poration in DOPG/DOPC/chol and DOPC/chol-GUVs for 50 minute

Chol (%)	Fraction of deformation, Fr_d		Fraction of poration, Fr_p	
	DOPG/DOPC/chol	DOPC/chol	DOPG/DOPC/chol	DOPC/chol
0	0.58 ± 0.01	0.43 ± 0.03	0.24 ± 0.02	0.28 ± 0.06
15	0.47 ± 0.02	0.32 ± 0.03	0.13 ± 0.02	0.24 ± 0.03
29	0.39 ± 0.04	0.28 ± 0.01	0.09 ± 0.02	0.21 ± 0.01
40	0.20 ± 0.01	0.18 ± 0.01	0.04 ± 0.01	0.03 ± 0.01

4.11 Different Types of Deformation of DOPG/DOPC/chol-GUVs

The deformation of DOPG/DOPC/chol-GUVs for 0, 15, 29, and 40% cholesterol under 3.33 µg/mL NPs are shown in Fig. 4.24. For various cholesterol concentrations, we observed diverse types of deformations in our studies. The GUVs were spherical in structure at 0 min in all circumstances (i.e., before interaction of NPs with GUVs). At 60 minutes, the final structure of GUVs is revealed as a result of NPs adsorption in the membranes. "Balloon-shaped" GUVs was seen in Fig. 4.24(a) for DOPG/DOPC/chol (70/30/0)-GUV. Fig. 4.24(b) shows the "stingray fish-shaped" DOPG/DOPC/chol (46/39/15)-GUV. Fig. 4.24(c) presents the "common murre egg-shaped" DOPG/DOPC/chol (43/28/29)-GUV. In Fig. 4.24(d), "maleo egg-shaped" or "oval-shaped" DOPG/DOPC/chol(40/20/40)-GUV was observed.
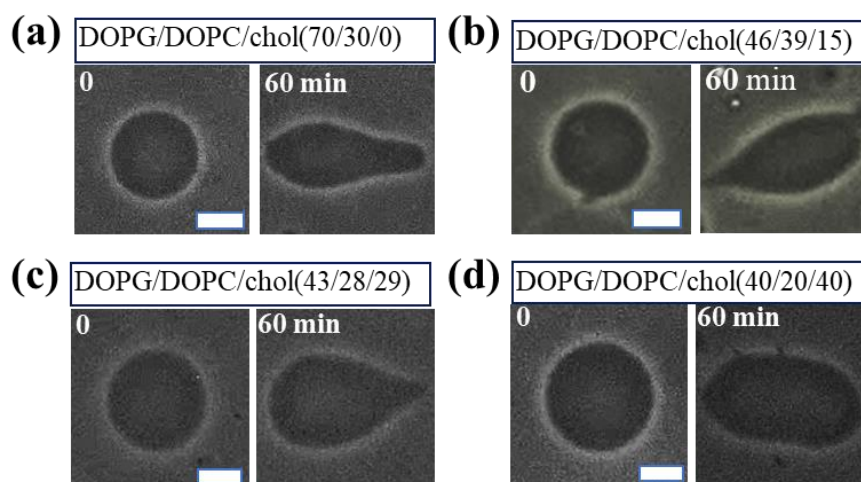
Fig. 4.24 Various types deformations of DOPG/DOPC/chol-GUVs in the presence of 3.33 µg/mL NPs. "Balloon-shaped" GUV in (a), "stingray fish-shaped" GUV in (b), "common murre egg-shaped" GUV in (c), and "oval-shaped" or "maleo egg-shaped" GUV in (d). The number on each image represents the time in minutes after the addition of NPs. The scale bar is 15 µm.

When we used the same concentration of NPs (e.g., 3.33 µg/mL NPs) in DOPG/DOPC/chol (46/39/15)-GUVs, we noticed various types of deformation. For instance, Fig. 4.25 depicts various deformations of GUVs. In all cases, the GUVs had a spherical structure at 0 min (i.e., before the interaction of NPs with GUVs). The interaction of NPs with membranes causes a minor deformation to begin at 25 minute, and at 60 min, the final structure of GUVs is revealed. The "stingray fish-shaped" GUVs are

depicted in Fig. 4.25(b), while the "common murre egg-shaped" GUVs are shown in Fig. 4.25 (a) and (c).
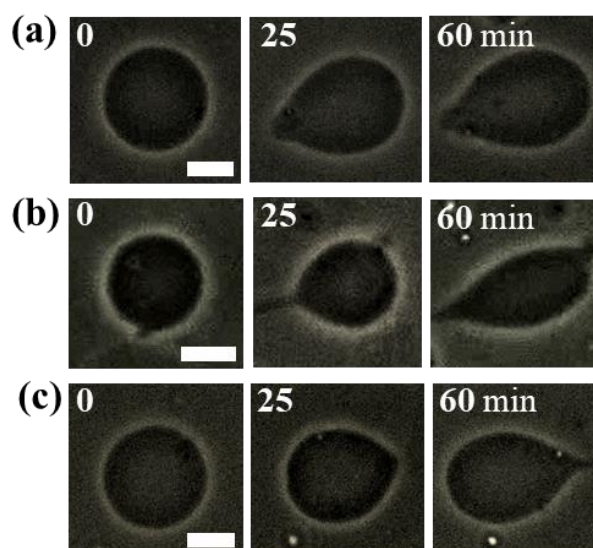
Fig. 4.25 Various forms of deformation in DOPG/DOPC/chol (46/39/15)-GUVs due to the interaction of 3.33 μg/mL NPs. "Common murre egg-shaped" GUV in (a) and (c), and "stingray fish-shaped" GUV in (b). The time in minute after the addition of NPs is depicted by the number on each image. The scale bar is 15 μm.

We also observed some fission-type shape change for DOPG/DOPC/chol (46/39/15)-GUVs at 3.33 μg/mL NPs in our study (Fig. 4.26). The GUV has a spherical structure at 0 min in the absence of NPs. At 10 min, there was a slight deformation; and between 30 and 60 min, there was a significant deformation. The GUV's shape changed from spherical to dumble after 30 min. The neck of the dumble increases with time and after 60 min, a single GUV split into two GUVs.
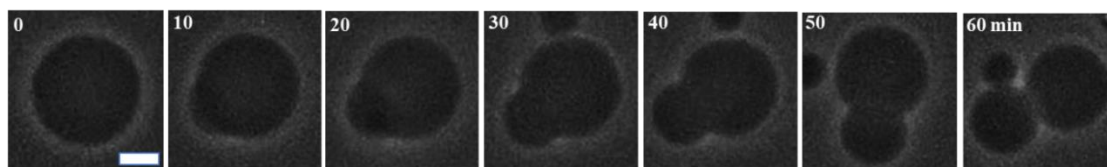
Fig. 4.26 Fission-type shape change of DOPG/DOPC/chol (46/39/15)-GUV in the presence of 3.33 μg/mL NPs, the number on every image shows the time in minutes after the interaction of NPs. The scale bar is 15 μm.

We also identified a very few number (at most one or two) of fusion type deformation for DOPG/DOPC/chol (46/39/15)-GUVs under 3.33 μg/mL NPs in our experiment. This kind

of shape change of GUV is shown in Fig. 4.27. The GUV has a spherical structure at 0 min in the absence of NPs. A small size GUV arrives to a larger size GUV and merges with it after five min. The two distinct GUVs formed a single GUV after 60 min.
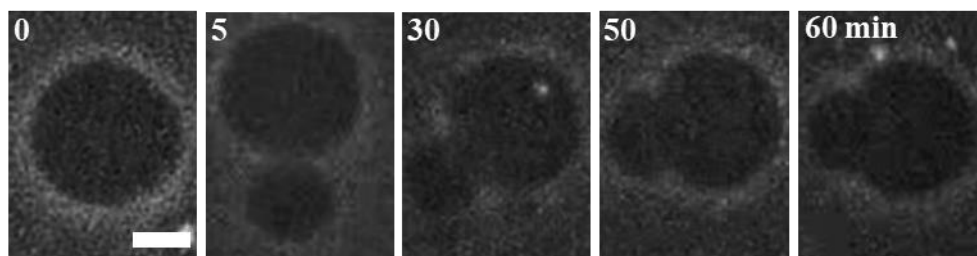
Fig. 4.27 Fusion-type shape change of DOPG/DOPC/chol (46/39/15)-GUV in the presence of 3.33 µg/mL NPs, the number on every image depicts the time in minutes after the addition of NPs in the vesicles. The scale bar is 15 µm.

4.12 Different Types of Deformation of DOPC/chol-GUVs

Following that, we looked at the deformation of cholesterol containing neutral membranes in the presence of 3.33 µg/mL NPs. The deformations of DOPC/chol-GUVs for 0, 15, 29, and 40% cholesterol under 3.33 µg/mL NPs are shown in Fig. 4.28.
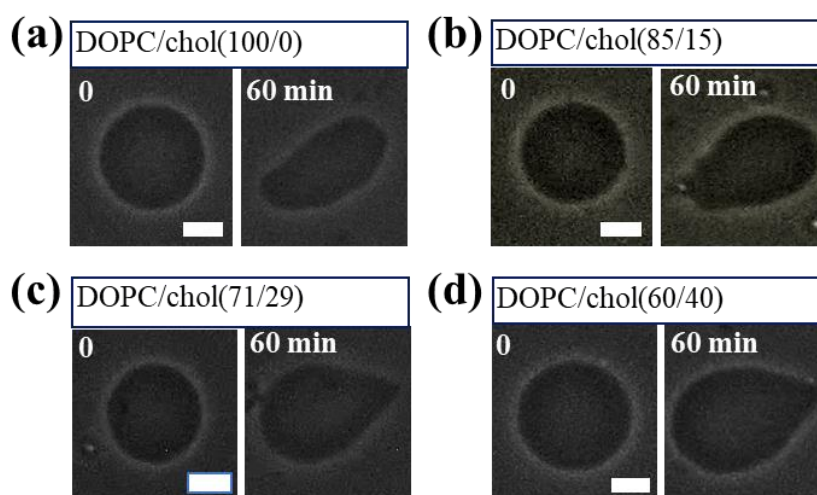
Fig. 4.28 Various types deformation of DOPC/chol-GUVs in the presence of 3.33 µg/mL NPs. "oval-shaped" or "maleo egg-shaped" GUV in (a), "Balloon-shaped" GUV in (b), "common murre egg-shaped" GUV in (c and (d). The number on each image represents the time in minutes after the addition of NPs. The scale bar is 15 µm.

For various cholesterol concentrations, we observed diverse types of deformations in our studies. The GUVs were spherical in structure at 0 min in all circumstances (i.e., before interaction of NPs with GUVs). At 60 min, the ultimate structure of GUVs is revealed as a result of NPs association with membranes. "Maleo egg-shaped" or "oval-shaped" GUVs was seen in Fig. 4.28(a) for DOPC/chol (100/0)-GUV. Fig. 4.28(b) shows the "Balloon-shaped" DOPC/chol (85/15)-GUV. Fig. 4.28(c) and (d) presents the "common murre egg-shaped" DOPC/chol (71/29) and DOPC/chol (60/40) -GUV.

4.13 Discussion

In DOPG/DOPC/chol and DOPC/chol-GUVs, the effects of cholesterol on anionic magnetite NPs induced deformation and poration were examined. With time, the degree of deformation (i.e. compactness) and the fraction of deformation increased, whereas with cholesterol these values reduced. Charged membranes (surface charge density - 0.16 C/m^2) have higher compactness and fraction of deformation than neutral membranes. Cholesterol inhibited NP-induced membrane poration, and neutral membranes have lower average period of poration than charged membranes. The fraction of poration increased with time until stabilizing. This fraction is higher in neutral membranes than in charged membranes.

A single dipole generation created by the lipid molecule's phosphorus-nitrogen (P$^-$-N$^+$) group determines the hydrophilicity of DOPC-GUVs. This dipole is made up of negatively charged phosphate group PO$_2^-$, which is ~0.5 nm away from N$^+$ choline group, which is positively charged and a big dipole with a value of ~20 Debye [147]. In typically, this dipole vector is aligned at an angle of (50-80°) to the bilayer periphery's normal [148]. The OH$^-$ groups in DOPG-contained GUVs create many short dipoles that contribute to hydrophilicity, with an equilibrium bond length of 0.097 nm. As a result, one DOPG molecule has a total dipole moment of 1.76 Debye [149]. Terminus P$^-$ can only displace with the whole molecule in the dipole of zwitterionic DOPC GUVs because it is firmly connected to the primary atomic construction of a lipid molecule, whereas under the influence of an external electric field produced by anionic NPs, terminal N$^+$ can move more freely under the effect of external electric field induced by anionic NPs. Negatively charged DOPG molecules generate an electric field near and within the bilayer, repelling

anionic NPs from the bilayer's surface. As a result of the interaction of NPs with the positive N^+ terminal, the tilt of the angle of (P^--N^+) dipole vector increases. This dipole tilt reduces the area of the bilayer's exterior monolayer, affecting the area mismatch between the two membrane monolayers.

The mechanical states of the monolayers can differ greatly due to the interaction between them. The 'bilayer coupling model' [64] describes the mechanical condition of such vesicles. The structure of GUVs is defined by the closed bilayer's elastic energy (W_{el}) minimization in this model. This energy only took into account membrane bending energy (W_b), not the elastic stretching of monolayers. For a given area and volume of GUVs, the area distinction among the two single-layers of a bilayer determines the minimum elastic energy [150–152]. Later, the area-difference-elasticity model (ADE model) [153, 154] was considered to be a significant fit for the change of shape (i.e., deformation) of vesicles. The area of each monolayer in the ADE model is not set to the symmetry area, but can extend elastically to enhance the membranes' nonlinear resilient energy. The resilient energy in this scenario is equal to the sum of W_b and the energy of correlative single-layer stretching (W_r), as shown in equation (3.4).

The bilayer's neutral surface with area A_0 is used for integration. The area distinction among the bilayer's outer and inner monolayers is given by out in the stretched condition of $\Delta A = A^{out} - A^{in}$. The distance between two monolayers' neutral surfaces is h. At equilibrium (i.e., un-stretched condition), the area distinction among the two single-layers in the GUVs is $\Delta A_o = A_o^{out} - A_o^{in}$. The structure of GUVs is determinate by the minimizing of W_{el} for a conferred area A, volume V, and a symmetry (i.e., reclined) area distinction ΔA_o, according to the ADE model. The deformation of vesicles from spherical under constant volume of GUVs is related to $(\Delta A - \Delta A_o)^2$. As a result, the degree of vesicle's deformation (i.e., compactness) increased over time for NPs adsorption (Fig. 4.1). As illustrated in Fig. 4.1(a), this model may also explain various types of deformation. The ADE model and the 'bilayer coupling model' are two probable processes for GUV deformation.

We incorporated cholesterol to the membranes and examined how vesicles deformed and porated in the presence of NPs. Cholesterol hindered the deformation and development of

pores in the membranes of spherical-shaped GUVs. Vesicles can be considered as a 'thin-walled closed shell' with various stable forms in continuum mechanics [155, 156], and therefore the approach utilized to analyze such vesicles [157–160]. The vesicle maintains the minimal energy (E_{sph}) for a spherical-shaped vesicle by having a variety of fixed structures with various types of energy (E_i). $E_{def} \gg E_{sph}$, is the energy of deformed GUVs. The fraction of deformed GUVs (F_{rd}) is calculated as follows [59]:

$$Fr_d = \frac{1}{E_{def}} \left(1 + \frac{E_{sph}}{E_{def}} \right)$$ (4.1)

If E_{sph} increases over time as a result of the area mismatch between the two membranes layers, the possibility of deformed GUVs increases. The incorporation of cholesterol affects the bending modulus of vesicles, which is an important mechanical property. Increased cholesterol concentration in the DOPC/chol and DOPG/DOPC/chol membranes increases the bending modulus by several orders of magnitude [57, 58, 37]. As a result, increasing cholesterol concentration in the membranes causes a decrease in the C_{om}^{av}, which is supported our findings (Fig. 4.9c). As a result of incorporating cholesterol, E_{sph} is reduced, and hence Fr_d is reduced. Vesicles must overcome the barrier width $\Delta E_{bar} = E_{bar} - E_{sph}$, where E_{bar} is the energy barrier, to transform the spherical-shaped GUVs into various forms. As cholesterol levels increases, so does the energy barrier increases, and as a result, Fr_d decreases (Fig. 4.11c). On the other hand, adsorption of more NPs, i.e., an increase in NPs concentration in the membrane, causes an area mismatch between the monolayers, which increases Fr_d and supports our findings (Fig. 4.12b).

The experimental results on NPs-induced calcein leakage from GUVs are now discussed (Fig. 4.13). The method of antimicrobial peptide-induced release of encapsulating fluorescent probes (e.g., calcein, Alexa fluor) has been elucidated in several recent articles [34, 65, 161]. The peptide's engagement to the membrane's external layer enhancements the area of this layer, causing the inner layer of the membrane to expand. Stretching the inner layer membrane creates positive lateral tension, which leads to the creation of vesicle pores and, as a result, the leakage of encapsulating probes. Pore or rupture generation in GUVs has been studied in various experiments due to the stretching of the lipid bilayer [162-164, 49]. The pore radius is too small for calcein leakage at the beginning of pore formation hence a little change in fluorescence intensity was seen before a rapid change at relatively larger sized pores (Fig. 4.13(b, c)). Polystyrene NPs are

capable of penetrating the lipid bilayer of GUVs due to lateral membrane stress [165]. Membrane rupture or pore development is caused by the lateral pressure created by adsorbed AuNPs in membranes [68]. The dynamics and mechanism of membrane rupture in the presence of carbon NPs under mechanical stress were explored using coarse-grained molecular dynamics simulations. Large and tiny NPs have been shown to have both strengthening and weakening effects on the strength of lipid bilayers [166]. Janus NPs diffuse to the static pore, which endures after the external stimulus has been eliminated, according to a coarse-grained numerical simulation. A slight increase in membrane stress causes the particle-lined pore to develop and immediately close, preventing transmission thru the membrane [167]. Based on the foregoing, we use the two-state transition model [168] to narrate the anionic magnetite NPs-induced membrane poration shown in Fig. 4.29. The first state is the 'intact state,' in which NPs adsorb to the GUVs' membrane's exterior monolayer (Fig. 4.29(a-c)), and the second status is the 'pore state,' in which a pore forms in the membrane (Fig. 4.29(d,e)). In this concept, a pore is created by a toroidal pattern of membrane surface bending. The transition rate from the whole phase to the pore phase is used to define the rate constant, k_p, which is determined by the Arrhenius equation's energy barrier, U_B.

$$k_p = A \exp\left(-\frac{U_B}{k_B T}\right) \tag{4.2}$$

Here, the Boltzmann constant is k_B, the absolute temperature is T, and A is a constant. However, individual occurrences in the two-state transition are stochastic. The portion of the whole phase can be defined as the fraction of intact GUVs, Fr_{intact} *(t)*, at which no calcein leakage occurred if the two-state conversion from the whole phase to the pore phase leads in irreversible pore generation.
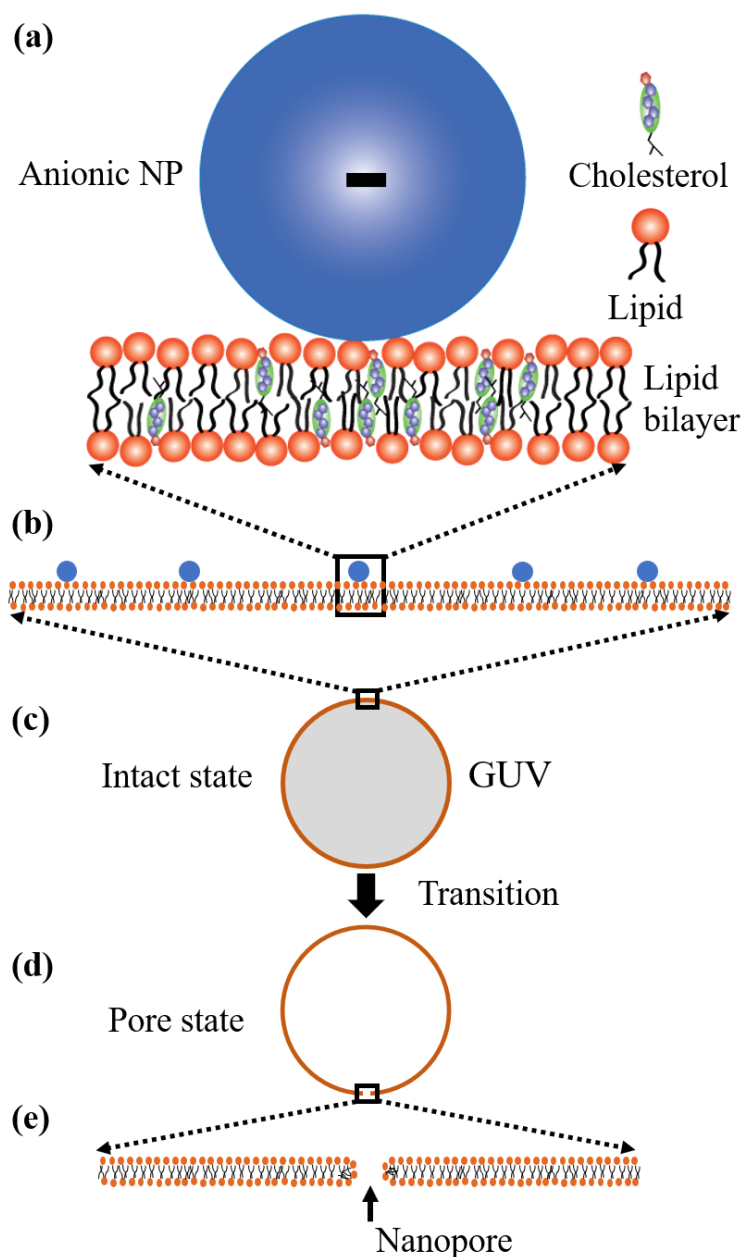
Fig. 4.29 Two-state transition model for NPs persuaded pore development in lipid membranes, (a-c) Adsorption of NPs in the outer layer of membranes of GUV, (d-e) Poration in the membranes of GUV

At time $t = 0$, this state was discovered for DOPG/DOPC/chol and DOPC/chol-GUVs in our experiment (Fig. 4.13). After adding NPs to the suspension of GUVs, this state was maintained for a period of time, with the fluorescence intensity remaining constant. The fluorescence intensity drops sharply after a specific amount of time, showing the pore condition. As a result, the pore phase can be referred as the GUV phase at which calcein releases out, and the fraction of pore state, Fr_p, can be written as $1 - Fr_{intact}(t)$.

We can take into account that NP binding in the outer monolayer causes the membranes to stretch (i.e., lateral tension, σ_n), resulting in the creation of a transmembrane pore in the bilayer. The pre-pore's free energy in the case of a toroidal pore is [169, 170] shown in equation (3.6). The energy of a pre-pore's barrier is shown in equation (3.7).

Addition of cholesterol in DOPG/DOPC/chol-GUVs (surface charge density - 0.16 C/m^2) increased the Γ from 12.9 to 14.6 pN [171]. This raises the value of U_B (r, σ_n), slowing the transition from intact to pore state (see Eq. 4.2). The time it took for pores to form increased with the addition of cholesterol (Fig. 4.21), while the fraction of pore created GUVs reduced (Fig. 4.22(c, d)), confirming our findings.

As described previously in this section, because of the electrostatic repulsion between OH$^-$ and the anionic NPs, the dipole (P$^-$-N$^+$) of DOPC/chol-GUVs is attracted to the anionic NPs more than DOPG/DOPC/chol-GUVs. The attractive force between anionic NPs and N$^+$ may approach a critical value in the case of DOPC/chol-GUVs, resulting in higher proportions of pore produced DOPC/chol-GUVs than DOPG/DOPC/chol-GUVs. On the other hand, the repulsive force between OH$^-$ and the anionic NPs may induce less attraction in DOPG/DOPC/chol-GUVs than in DOPC/chol-GUVs. As a result, area mismatch in DOPG/DOPC/chol-GUVs may increase with a longer time gap. This may result in a higher fraction of deformed DOPG/DOPC/chol-GUVs than DOPC/chol-GUVs. This debate is in line with the findings of the study (Fig. 4.23).

CHAPTER 5

CONCLUSIONS

5.1 Summary of Results

We have examined the deformation and poration of charged DOPG/DOPC/chol-GUVs and neutral DOPC/chol-GUVs induced by anionic magnetite NPs. Eco-friendly technique was used to synthesize the NPs, and the natural swelling method was used to synthesize the GUVs. The cholesterol content in both membranes varied from 0 to 40% mole in a physiological buffer.

The degree of deformation (i.e., compactness) of spherical shaped GUVs increased over time after the addition of NPs. The average compactness values at 60 minute for 0, 15, 29, and 40% chol in DOPG/DOPC/chol-GUVs were 1.280 ± 0.002, 1.269 ± 0.022, 1.154 ± 0.022, and 1.131 ± 0.010, respectively under 3.33 μg/mL NPs. At 60 minute, the values of average compactness were 1.009 ± 0.005 for DOPC/chol(60/40)-GUVs, 1.109 ± 0.004 for DOPC/chol(71/29)-GUVs, 1.131 ± 0.004 for DOPC/chol(85/15)-GUVs, and 1.269 ± 0.009 for DOPC/chol(100/0)-GUVs. Hence, the increase of cholesterol in both charged and neutral membranes decreased the values of compactness of GUVs.

The fraction of deformation of DOPG/DOPC/chol-GUVs increased with time under 3.33 μg/mL NPs. At 0, 10, 20, 30, 40, 50, and 60 minutes, the fractions of deformed GUVs were 0, 0.15 ± 0.02, 0.22 ± 0.03, 0.29 ± 0.04, 0.40 ± 0.01, 0.48 ± 0.02, and 0.50 ± 0.04, respectively. The fraction of deformation of GUVs increased with NPs concentration. At 50 minute, the fraction of deformed GUVs was 0.43 ± 0.01 for 2.00 μg/mL NPs, 0.47 ± 0.01 for 3.33 μg/mL NPs, and 0.62 ± 0.02 for 4.70 μg/mL NPs. As surface pressure in lipid membranes is more in higher NPs concentration, the fraction of deformation was higher.

The fraction of deformed GUVs depended on cholesterol in the vesicle membranes. The fractions of deformed GUVs were 0.63 ± 0.02 for 0% chol, 0.50 ± 0.00 for 15% chol, 0.43 ± 0.01 for 29% chol, and 0.24 ± 0.01 for 40% chol at 60 minute. Hence, cholesterol inhibits the deformation of GUVs. From this analysis, we found that for both (neutral and charged) systems, the values of compactness and the fraction of deformed GUVs increased over time. The deformation began with a negligible one and subsequently increased to a

value that was nearly constant. The amount of cholesterol in the membranes reduced both types of deformation.

We determined the average time of poration for various (0, 15, 29, & 40 % chol) cholesterol containing charged and neutral membranes under 3.33 μg/mL NPs. The average time for pore formation increased for both types of GUVs as cholesterol increased in the membranes. These results suggest that vesicle pore formation is inhibited by an increase in cholesterol concentration in lipid membranes. However, cholesterol containing neutral membranes showed a shorter time of poration than charged ones.

The thin-walled closed shell model and the bilayer coupling model are used to describe the deformation. The leaking of the water-soluble fluorescent probe calcein from the inside of GUVs was used to study the membrane poration. The poration in GUVs can be adequately explained by the two-state transition model. One of the key factors for inhibiting poration in membranes containing cholesterol is the higher line tension near the pore's edge. Charged vesicles exhibit a higher fraction of deformed GUVs than neutral ones at given cholesterol content, but poration exhibits the opposite trend. Due to the chemical differences between DOPG and DOPC lipids, this trend developed. These studies would aid in understanding the results of anionic NPs' interactions with real cells.

It can be said that adsorption of NPs can alter the morphology of cells and can damage the cell membranes. As biomembranes contain cholesterol, which can reduce this damage. Cardiovascular and pulmonary activities are affected by the interaction of NPs, resulting in cardiorespiratory disorders with significant mortality and morbidity. Because NPs-based insecticides and food items are utilized in agriculture, they may inhibit or harm beneficial bacterial activity because NPs adhere to their membranes. On the other hand, these NPs can be utilized to kill or harm pathogenic bacteria (bacterial membranes are cholesterol-free). Since nanotechnology-based research and industry have grown rapidly, it is important to maintain proper safety in nanotechnology-based laboratories and companies in order to prevent NPs exposure.

5.2 Concluding Remarks

We conclude that cholesterol inhibited the deformation and poration. The values of compactness and the fraction of deformed GUVs increase with time for both charged and neutral systems. Both types of deformation decrease with cholesterol content in the membranes. At a specific cholesterol content, the value of the fraction of deformed vesicle is higher for the charged vesicles as compared to the neutral ones, in which poration shows the opposite trend. Such a trend occurs due to the differences in head's chemical structure of DOPG and DOPC lipids. Hence cholesterol increases the stability of cell membrane.

This research would help to understand the effects of cholesterol on the interaction of anionic NPs with real cells.

5.3 Suggestion for Future Research

1. Investigation of NPs-induced deformation and poration in the presence of membrane potential.
2. Investigation of vesicle deformation and leakage of calcein due to NPs using micropipette technique.

REFERENCES

1. Monaliben, S., Derek, F., Shashi, S., Suraj, K. T., Gérrard E. J. P., "Green synthesis of metallic nanoparticles via biological entities," *Mater. Sci.,* vol. 8, pp. 7278–7308, 2015.

2. Gregory, G., Sergio, M., Francis, L. D., "Nanomaterial properties: size and shape dependencies," *J. Nanomater.,* vol. 2012, pp. 2, 2012.

3. Francois, F., Ludovic, E., Gerard, B., "Optical properties of nanostructured materials: a review," *J. Nanophotonics,* vol. 5, pp. 1934-2608, 2011.

4. Dougherty, T. J., Gomer, C. J., Henderson, B. W., Jori, G., Kessel, D., Korbelik, M., Moan, J., and Peng, Q., "Photodynamic Therapy," *J. Natl. Cancer Inst*., vol. 90, pp. 889-905, 1998.

5. Lee, C. C., Gillies, E. R., Fox, M. E., Guillaudeu, S. J., Fréchet, J. M. J., Dy, E. E. and Szoka, F. C., "A single dose of doxorubicin-functionalized bow-tie dendrimer cures mice bearing C-26 colon carcinomas," *Proc. Natl. Acad. Sci. U.S.A,* vol. 103, pp. 16649–16654, 2006.

6. Beyer, T., Townsend, D. W., Brun, T., Kinahan, P. E., Charron, M., Roddy, R., Jerin, J., Young, J., Byars, L., and Nutt, R., "A combined PET/CT scanner for clinical oncology," *J. Nucl. Med.,* vol. 12, pp. 1369-1376, 2000.

7. Han, G., Ghosh, P., Rotello, V. M., "Functionalized gold nanoparticles for drug delivery," *Nanome,* vol. 2, pp. 113–123, 2007.

8. Jain, S., Hirst, D. G., O'Sullivan, J. M., "Gold nanoparticles as novel agents for cancer therapy," *Br. J. Radiol.,* vol. 85, pp. 101–113, 2012.

9. Gehr, P., Zellner, R., "Biological responses to nanoscale particles: molecular and cellular aspects and methodological approaches," *Springer Sci. Rev.*, 2019.

10. Hainfeld, J. F., Dilmanian, F. A., Slatkin, D. N., Smilowitz, H. M., "Radiotherapy enhancement with gold nanoparticles," *J. Pharm. Pharmacol.,* vol. 60, pp. 977–985, 2008.

11. Hainfeld, J. F., Dilmanian, F. A., Zhong, Z., Slatkin, D. N., Kalef-Ezra, J. A., Smilowitz, H. M., "Gold nanoparticles enhance the radiation therapy of a murine squamous cell carcinoma," *Phys. Med. Biol.,* vol. 55, pp. 3045–3059, 2010.

12. Chithrani, D. B., Jelveh, S., Jalali, F., van Prooijen, M., Allen, C., Bristow, R.G., Hill, R.P., Jaffray, D. A., "Gold nanoparticles as radiation sensitizers in cancer therapy," *Radiat. Res.,* vol. 173, pp. 719–728, 2010.

13. Awasthi, R., Roseblade, A., Hansbro, P. M., Rathbone, M. J., Dua, K., Bebawy, M., "Nanoparticles in cancer treatment: opportunities and obstacles," *Curr. Drug Targets,* vol. 19, pp. 1696–1709, 2018.

14. Colvin, V. L., "The potential environmental impact of engineered nanomaterials," *Nat. Biotechnol.,* vol. 21, pp. 1166–1170, 2003.

15. Fischer, H. C., Chan, W. C. W., "Nanotoxicity: the growing need for in vivo study," *Curr. Opin. Biotechnol.,* vol. 18, pp. 565–571, 2007.

16. Lewinski, N., Colvin, V., Drezek, R., 2008 "Cytotoxicity of nanoparticles," *Small Weinh. Bergstr. Ger.,* vol. 4, pp. 26–49, 2008.

17. Nel, A. E., Mädler, L., Velegol, D., Xia, T., Hoek, E. M. V, Somasundaran, P., Klaessig, F., Castranova, V., Thompson, M., "Understanding biophysicochemical interactions at the nano-bio interface," *Nat. Mater.,* vol. 8, pp. 543–557, 2009.

18. Fadeel, B., Garcia-Bennett, A. E., "Better safe than sorry: understanding the toxicological properties of inorganic nanoparticles manufactured for biomedical applications," *Adv. Drug Deliv. Rev.,* vol. 62, 362–374, 2010.

19. Brook, R. D., *et al.,* "Particulate matter air pollution and cardiovascular disease: An update to the scientific statement from the American Heart Association," *Circulation,* vol. 121, pp. 2331–2378, 2010.

20. Xia, T., Zhu, Y., Mu, L., Zhang, Z-F., Liu, S., "Pulmonary diseases induced by ambient ultrafine and engineered nanoparticles in twenty-first century," *Natl. Sci. Rev.,* vol. 3, pp. 416–429, 2016.

21. Buzea, C., Pacheco, I. I., Robbie, K., "Nanomaterials and nanoparticles: sources and toxicity," *Biointerphases,* vol. 2, MR17–MR71, 2007.

22. Kendall, M., Lynch, I., "Long-term monitoring for nanomedicine implants and drugs," *Nat. Nanotechnol.,* vol. 11, pp. 206–210, 2016.

23. Souza, V. G. L., Fernando, A. L., "Nanoparticles in food packaging: Biodegradability and potential migration to food—a review," *Food Packag. Shelf Life,* vol. 8, pp. 63–70, 2016.

24. Shaffer, R. E., & Rengasamy, S., "Respiratory protection against airborne nanoparticles: a review," *J. Nanopart Res.*, vol. 11, pp. 1661–1672, 2009.

25. Chan, J. K., W. Fanucchi, M. V., Anderson, D. S., Abid, A. D., Wallis, C. D., Dickinson, D. A., Kumfer, B. M., Kennedy, I. M., Wexler, A. S., Winkle, L. S. V., "Susceptibility to inhaled flame-generated ultrafine soot in neonatal and dult rat

lungs," *Toxicol. Sci.,* vol. 124, pp. 472–486, 2011.

26. Cross, R., "Air-pollution-derived magnetic nanoparticles found in human brains," *C&EN*, Vol. 94(36), 2016.

27. Simeonidis, K., Kermenidou, M., Martinez-Boubeta, C., "Magnetic nanoparticles: an indicator of health risks related to anthropogenic airborne particulate matter," *Environ. Pollut.,* vol. 271,pp. 116309, 2021.

28. Maher, B. A., Ahmed, I. A. M., Karloukovski, V., MacLaren, D. A., Foulds, P. G., Allsop, D., Mann, D. M. A, Torres-Jardón, R., Calderon-Garciduenas, L., "Magnetite pollution nanoparticles in the human brain," *Proc. Natl. Acad. Sci.,* vol. 113, pp. 10797–10801, 2016.

29. Plascencia-Villa, G., Ponce, A., Collingwood, J. F., Arellano-Jiménez, M. J., Zhu, X., Rogers, J. T., Betancourt, I., José-Yacamán, M., Perry, G., "High-resolution analytical imaging and electron holography of magnetite particles in amyloid cores of Alzheimer's disease," *Sci. Rep.,* vol. 6, pp. 24873, 2016.

30. Chapman, D., "Phospholipid bilayers physical principles and models," *Cell Biochem Funct*, vol. 6(2), pp. 147-148, 1988.

31. Róg, T., Pasenkiewicz-Gierula, M., Vattulainen, I., Karttunen, M., "Ordering effects of cholesterol and its analogues," *Biochim. Biophys. Acta*, vol. 1788, pp 97–121, 2009.

32. Evans, E., Smith, B.A., "Kinetics of hole nucleation in biomembrane rupture," *New J Phys.,* vol. 13, pp 095010, 2011.

33. Vasir, J.K., Labhasetwar, V., "Biodegradable nanoparticles for cytosolic delivery of therapeutics," *Adv. Drug Deliv*. *Rev.*, vol. 59, pp 718–728, 2007.

34. Karal, M. A. S., Alam, J. M., Takahashi, T., Levadny, V., Yamazaki, M., "Stretch activated pore of the antimicrobial peptide, maganin 2," *Langmuir,* vol. 31, pp. 3391-3401, 2015.

35. Islam, M. Z., Ariyama, H., Alam, J. M., Yamazaki, M., "Entry of cell-penetrating peptide transportan 10 into a single vesicle by translocating across lipid membrane and its induced pores," *Biochemistry,* vol. 53, pp. 386-396, 2014.

36. DePierre, J. W., Karnovsky, M. L., "Plasma membranes of mammalian cells," *J. Cell Biol.,* vol. 56, pp. 275–303, 1973.

37. Eid, J., Razmazma, H., Jraij, A., Ebrahimi, A., Monticelli, L., "On calculating the bending modulus of lipid bilayer membranes from buckling simulations," *J. Phys.*

Chem. B, vol. 124, pp. 6299–6311, 2020.

38. Yeagle, P.L., "Cholesterol and the cell membrane," *Biochim. Biophys. Acta*, vol. 822, pp 267–287, 1985.

39. Hinzpeter, A., Fritsch, J., Borot, F., Trudel, S., Vieu, D.L., Brouillard, F., Baudouin-Legros, M., Clain, J., Edelman, A., Ollero, M., "Membrane cholesterol content modulates ClC-2 gating and sensitivity to oxidative stress," *J biology Chem*, vol. 282, pp 2423–32, 2007.

40. Pucadyil, T.J., Chattopadhyay, A., "Role of cholesterol in the function and organization of G-protein coupled receptors," *Prog. Lipid Res.*, vol. 45, pp 295–333, 2006.

41. Holthuis, J.C.M., Meer, G.V., Huitema, K., "Lipid microdomains, lipid translocation and the organization of intracellular membrane transport (review)," *Mol. Membr. Biol.*, vol. 20, pp 231–241, 2003.

42. Evans, E., Heinrich, V., Ludwig, F., Rawicz, W., "Dynamic tension spectroscopy and strength of biomembranes," *Biophys J.*, vol. 85, pp 2342–2350, 2003.

43. Semple, S.C., Chonn, A., Cullis, P.R., "Influence of cholesterol on the association of plasma proteins with liposomes," *Biochemistry*, vol. 35, pp 2521–2525, 1996.

44. Coderch, L., Fonollosa, J., De Pera, M., Estelrich, J., De La, M.A., Parra, J.L., "Influence of cholesterol on liposome fluidity by EPR. Relationship with percutaneous absorption," *J control release: official journal of the Controlled Release Society*, vol. 68, pp 85–95, 2000.

45. Needham, D., Nunn, R.S., "Elastic deformation and failure of lipid bilayer membranes containing cholesterol," *Biophys. J.*, vol. 58, pp 997–1009, 1990.

46. Islam, M. Z., Alam, J. M., Tamba, Y., Karal, M. A. S., Yamazaki, M., "The single GUV method for revealing the functions of antimicrobial, pore-forming toxin, and cell-penetrating peptides or proteins," *Phys. Chem. Chem. Phys. PCCP,* vol. 16, pp. 15752–15767, 2014.

47. Wang, B., Zhang, L., Bae, S. C., Granick, S., "Nanoparticle-induced surface reconstruction of phospholipid membranes," *Proc. Natl. Acad. Sci. U.S.A.,* vol. 105, pp. 18171–18175, 2008.

48. Dimova, R., Riske, K. A., Aranda, S., Bezlyepkina, N., Knorr, R. L., Lipowsky, R., "Giant vesicles in electric fields," *Soft Matter,* vol. 3, pp. 817, 2007.

49. Karal, M. A. S., Ahamed, M. K., Ahmed, M., Mahbub, Z. B., "Recent

developments in the kinetics of ruptures of giant vesicles under constant tension," *RSC Adv.,* vol. 11, pp. 29598–29619, 2021.

50. Chen, Z., Rand, R. P., "The influence of cholesterol on phospholipid membrane curvature and bending elasticity," *Biophys. J.,* vol. 73, pp. 267–276, 1997.

51. Doktorova, M., *et al.,* "Cholesterol promotes protein binding by affecting membrane electrostatics and solvation properties," *Biophys. J.,* vol. 113, pp. 2004–2015, 2017.

52. Evans, E., Rawicz, W., "Entropy-driven tension and bending elasticity in condensed-fluid membranes," *Phys. Rev. Lett.,* vol. 64, pp. 2094–2097, 1990.

53. Henriksen, J., Rowat, A. C., Brief, E., Hsueh, Y. W., Thewalt, J. L., Zuckermann, M. J., Ipsen, J. H., "Universal behavior of membranes with sterols," *Biophys. J.,* vol. 90, pp. 1639–1649, 2006.

54. Pan, J., Tristram-Nagle, S., Nagle, J. F., "Effect of cholesterol on structural and mechanical properties of membranes depends on lipid chain saturation," *Phys. Rev. E,* vol. 80, pp. 021931, 2009.

55. Pan, J., Mills, T. T., Tristram-Nagle, S., Nagle, J. F., "Cholesterol perturbs lipid bilayers nonuniversally," *Phys. Rev. Lett.,* vol. 100, pp. 198103, 2008.

56. Ashkar, R., *et al.,* "Cholesterol affects the bending rigidity of DOPC membranes," *Biophys. J.,* vol. 116, pp. 328a, 2019.

57. Chakraborty, S., *et al.,* "How cholesterol stiffens unsaturated lipid membranes," *Proc. Natl. Acad. Sci.,* vol. 117, pp. 21896–21905, 2020.

58. Karal, M. A. S., Mokta, N. A., Levadny, V., Belaya, M., Ahmed, M., Ahamed, M. K., Ahammed, S., "Effects of cholesterol on the size distribution and bending modulus of lipid vesicles," *PLOS ONE,* vol. 17, e0263119, 2022.

59. Karal, M. A. S., Ahammed. S., Levadny, V., Belaya, M., Ahamed, M. K., Ahmed, M., Mahbub, Z. B., Ullah, A. K. M. A., "Deformation and poration of giant unilamellar vesicles induced by anionic nanoparticles," *Chem. Phys. Lipids*, vol. 230, pp. 104916, 2020.

60. Contini, C., Schneemilch, M., Gaisford, S., Quirke, N., "Nanoparticle–membrane interactions," *J. Exp. Nanosci.,* vol. 13, pp. 62–81, 2018.

61. Laurencin, M., Georgelin, T., Malezieux, B., Siaugue, J-M., Ménager, C., "Interactions between giant unilamellar vesicles and charged core−shell magnetic nanoparticles," *Langmuir,* vol. 26, pp. 16025–16030, 2010.

62. Yu, Y., Granick, S., "Pearling of lipid vesicles induced by nanoparticles," *J. Am. Chem. Soc.,* vol. 131, pp. 14158–14159, 2009.

63. Li, S., Malmstadt, N., "Deformation and poration of lipid bilayer membranes by cationic nanoparticles," *Soft Matter,* vol. 9, pp. 4969–4976, 2013.

64. Käs, J., Sackmann, E., "Shape transitions and shape stability of giant phospholipid vesicles in pure water induced by area-to-volume changes," *Biophys. J.,* vol. 60, pp. 825–844, 1991.

65. Hasan, M., Karal, M. A. S., Levandnyy, V., Yamazaki, M., "Mechanism of initial stage of pore formation induced by antimicrobial peptide magainin 2," *Langmuir ACS J.*, vol. 34, pp. 3349-3362, 2018.

66. Karal, M. A. S., Yamazaki, M., "Communication: activation energy of tension-induced pore formation in lipid membranes," *J. Chem. Phys.*, vol. 143, pp. 081103, 2015.

67. Karal, M. A. S., Levadny, V., Yamazaki, M., "Analysis of constant tension-induced rupture of lipid membranes using activation energy," *Phys. Chem. Chem. Phys.*, vol. 18, pp. 13487–13495, 2016.

68. Bhat, A., Edwards, L. W., Fu, X., Badman, D. L., Huo, S., Jin, A. J., Lu, Q., "Effects of gold nanoparticles on lipid packing and membrane pore formation," *Appl. Phys. Lett.,* vol. 109, pp. 263106, 2016.

69. Mueller, P., Rudin, D. O., Tien, H. T., and Wescott, W. C., "Methods for the formation of single bimolecular lipid membranes in aqueous solution," *J. Phys. Chem.*, vol. 67(2), pp. 534–535, 1963.s

70. Bastus, N. G., Comenge, J., and Puntes, V., "Kinetically controlled seeded growth synthesis of citrate-stabilized gold nanoparticles of up to 200 nm: size focusing versus ostwald ripening," *Langmuir*, vol. 27, pp. 11098–11105, 2011.

71. Sezgin, E., Sadowski, T., and Simons, K., "Measuring lipid packing of model and cellular membranes with environment sensitive probes," *Langmuir*, vol. 30, pp. 8160-8166, 2014.

72. Sanchez, S. A., Tricerri, M. A., and Gratton, E., "Laurdan generalized polarization fluctuations measures membrane packing micro-heterogeneity in vivo," *Proc. Natl. Acad. Sci. U.S.A.,* VOL. 109(19), pp. 7314–7319, 2012.

73. Yu, W., So, P. T., French, T., and Gratton, E., "Fluorescence generalized polarization of cell membranes: a two-photon scanning microscopy approach,"

Biophys. J., vol. 70, pp. 626-636, 1996.

74. Parasassi, T., Gratton, E., Yu, W. M., Wilson, P., and Levi, M., "Two-photon fluorescence microscopy of laurdan generalized polarization domains in model and natural membranes," *Biophys. J.*, vol. 72, pp. 2413-2429, 1997.

75. Tricerri, M. A., Toledo, J. D., Sanchez, S. A., Hazlett, T. L., Gratton, E., Jonas, A., and Garda, H. A., "Visualization and analysis of apolipoprotein AI interaction with binary phospholipid bilayers," *J. Lipid Res.*, vol. 46, pp. 669-678, 2005.

76. Janiak, M. J., Small, D. M., and Shipley, G. G., "Temperature and compositional dependence of the structure of hydrated dimyristoyl lecithin," *J. Biol. Chem.*, Vol. 254, pp. 6068-6078, 1979.

77. Lipowsky, R., "The morphology of lipid membranes," *Curr. Opin. Struct. Biol.*, vol. 5, pp. 531-540, 1995.

78. Heimburg, T., "Thermal biophysics of membranes," (Wiley-VCH, Weinheim, 2007), Chap. 12, p. 261.

79. Angelova, M. I., Luisi, P. L., Walde, P., "Liposome electroformation. In giant vesicles, perspectives in supramolecular chemistry," Eds.; John Wiley and Sons, Ltd.: West Sussex, England, vol. 6, pp. 27-36, 2000.

80. Massart, R., "Preparation of aqueous magnetic liquids in alkaline and acidic media," *IEEE Trans. Magn.*, vol. 17(2), pp. 1247–1248, 1981.

81. Fauconnier, N.; Bee, A.; Roger, J.; Pons, J. N. "Adsorption of gluconic and citric acids on maghemite particles in aqueous medium," *Prog. Colloid Polym. Sci.*, vol. 100, pp. 212–216, 1996.

82. Lu, Y., Yin, Y., Mayers, B. T., Xia, Y., "Modifying the surface properties of superparamagnetic iron oxide nanoparticles through a sol−gel approach," *Nano Lett.*, vol. 2(3), pp. 183–186, 2002.

83. Maurice, V.; Georgelin, T.; Siaugue, J. M.; Cabuil, V., "Synthesis and characterization of functionalized core–shell ΥFe_2O_3–SiO_2 nanoparticles," *J. Magn. Magn. Mater.*, vol. 321, pp. 1408–1413, 2009.

84. Georgelin, T., Maurice, V., Malizieux, B., Siaugue, J. M., Cabuil, V., "Design of multifunctionalized Υ-Fe_2O_3@SiO_2 core–shell nanoparticles for enzymes immobilization," *J. Nanopart. Res.*, vol. 12, pp. 675–680, 2010.

85. d'Orlye, F., Varenne, A., Georgelin, T., Siaugue, J. M., Teste, B., Descroix, S., Gareil, P., "Charge-based characterization of nanometric cationic bifunctional

maghemite/silica core/shell particles by capillary zone electrophoresis," *J. Electrophor*, vol. 30(14), pp. 2572–2582, 2009.

86.   Akashi, K., Miyata, H., Itoh, H., Kinosita, K., "Preparation of giant liposomes in physiological conditions and their characterization under an optical microscope," *Biophys. J.,* vol. 71, pp. 3242-3250, 1996.

87.   Yu, Y., Anthony, S. M., Zhang, L. F., Bae, S. C., Granick, S., "Cationic nanoparticles stabilize zwitterionic liposomes better than anionic ones," *J Phys Chem C,* vol.111, pp. 8233–8236, 2007.

88.   Zhang, H., 'Thin-film hydration followed by extrusion method for liposome preparation," (chapter 2), *Liposomes: Methods and Protocols*, Methods in Molecular Biology, vol. 1522, pp. 17-22, 2017.

89.   Krichevsky, O., and Bonnet, G., "Fluorescence correlation spectroscopy: the technique and its applications," *IOPSCIENCE,* vol. 65, pp. 251-297, 2002.

90.   Clegg, Robert, M., "Fo̎rster resonance energy transfer—FRET what is it, why do it, and how it's done," (CHAPTER 1), *Elsevier*, vol. 33, pp. 1-57, 2009.

91.   Campoy, A. V., Ohtaka, H., Nezami, A., Muzammil, S., and Freire, E., "Isothermal titration calorimetry," *Curr Protoc Cell Biol.,* unit. 17.8, 2004.

92.   Gaus, K., Gratton, E., Kable, E. P. W*.,* Allan S., Jones, A. S., Gelissen, I., Kritharide, L., and Jessup, W., "Visualizing lipid structure and raft domains in living cells with two-photon microscopy," *Proc. Natl. Acad. Sci. U.S.A.,* vol. 100(26), pp. 15554–15559, 2003.

93.   de Almeida, R. D. F., Loura, L. M. S., Fedorov, A., Prieto, M., "Lipid rafts have different sizes depending on membrane composition: A time-resolved fluorescence resonance energy transfer study," *J. Mol. Bol.,* vol. 346, pp. 1109–1120, 2005.

94.   Zhang, L. F., Granick, S., "How to stabilize phospholipid liposomes (using nanoparticles)," *Nano Lett.,* vol. 6, pp. 694–698, 2006.

95.   Roiter, Y., Ornatska, M, Rammohan, A. R, et al., "Interaction of nanoparticles with lipid membrane," *Nano Letters*, vol. 8(3), pp. 941–944, 2008.

96.   Levene, M. J.; Korlach, J.; Turner, S. W.; Foquet, M.; Craighead, H. G.; Webb, W. W., "Zero-mode waveguides for single-molecule analysis at high concentrations," *Science*, vol. 299, pp. 682–686, 2003.

97.   Roiter, Y., Minko, S., "AFM single molecule experiments at the solid-liquid interface: in situ conformation of adsorbed flexible polyelectrolyte chains," *J. Am.*

Chem. Soc., vol. 127, pp. 15688–15689, 2005.

98. Chernomordik, L., Kozlov, M., Zimmerberg, J., "Lipids in biological membrane fusion," *J. membr. Biol.*, vol. 146, pp 1, 1995.

99. Liu, J., Kaksonen, M., Drubin, D.G., Oster, G., "Endocytic vesicle scission by lipid phase boundary forces," *Proc. Natl. Acad. Sci. U.S.A.*, vol. 103, pp 10277, 2006.

100. Noguchi, H., "Anisotropic surface tension of buckled fluid membranes," *Phys. Rev. E* Stat Nonlin Soft Matter Phys., vol. 83(6), pp. 061919, 2011.

101. Hu, M.; Diggins, P.; Deserno, M., "Determining the bending modulus of a lipid membrane by simulating buckling," *J. Chem. Phys.*, vol. 138(21), pp. 214110, 2013.

102. Helfrich, W., "Elastic properties of lipid bilayers: theory and possible experiments," *Z. Naturforsch., C: J. Biosci.*, vol. 28(11−12), pp. 693−703, 1973.

103. Rawicz, W., Olbrich, K. C., McIntosh, T., Needham, D., Evans, E., "Effect of chain length and unsaturation on elasticity of lipid bilayers," *Biophys. J.*, vol. 79(1), pp. 328−339, 2000.

104. Arriaga, L. R., Montero, I. L., Monroy, F., Gil, G. O., Farago, B., Hellweg, T., "Stiffening effect of cholesterol on disordered lipid phases: A combined neutron spin echo + dynamic light scattering analysis of the bending elasticity of large unilamellar vesicles," *Biophys. J.*, vol. 96, pp. 3629-3637, 2009.

105. Martinez, G. V., Dykstra, E. M., Lope-Piedrafita, S., Job, C., Brown, M. F., "NMR elastometry of fluid membranes in the mesoscopic regime," *Phys. Rev. E*, vol. 66, pp. 050902, 2002.

106. Doktorova, M., Harries, D., Khelashvili, G., "Determination of bending rigidity and tilt modulus of lipid membranes from real-space fluctuation analysis of molecular dynamics simulations," *Phys. Chem. Chem. Phys.,* vol. 19, pp. 16806–16818, 2017.

107. Kuˇcerka, N., Pencer, J., Nieh, M. P., Katsaras, J., "Influence of cholesterol on the bilayer properties of monounsaturated phosphatidylcholine unilamellar vesicles," *Eur. Phys. J. E*, vol. 23, pp. 247–254, 2007.

108. Kučerka, N., Tristram-Nagle, S., and Nagle, J. F., "Structure of fully hydrated fluid phase lipid bilayers with monounsaturated chains," *J. Membr. Biol.*, vol. 208, pp.193-202, 2005.

109. Henriksen, J., Rowat, A. C., Brief, E., Y. Hsueh, Y. W., Thewalt, J. L., Zuckermann, M. J., and Ipsen, J. H., "Universal behavior of membranes with sterols," *Biophys. J.*, vol. 90(5), pp. 1639-1649, 2006.

110. Song, J. B., and Waugh, R. E., "Bending rigidity of SOPC membranes containing cholesterol," *Biophys. J.*, vol. 64(6), pp. 1967-1970, 1993.

111. Pan, J. J., Mills, T. T., Tristram-Nagle, S., and Nagle, J. F., "Cholesterol perturbs lipid bilayers nonuniversally," *Phys. Rev. Lett.*, vol. 100(19), pp. 198103(4), 2008.

112. *https://en.wikiversity.org/wiki/The_Cell_Membrane*

113. Walde, P., Cosentino, K., Engel, H., and Stano, P., "Giant vesicles: preparations and applications," *ChemBioChem,* vol. 11, pp. 848–865, 2010.

114. Altamura, E., Carrara, P., D'Angelo, F., Mavelli, F., and Stano, P., "Extrinsic stochastic factors (solute partition) in gene expression inside lipid vesicles and lipidstabilized water-in-oil droplets: a review," *Synth. Biol.,* vol. 3, 2018.

115. Mashaghi, S., Jadidi, T., Koenderink, G. & Mashaghi, A., "Lipid nanotechnology," *Int. J. Mol. Sci.,* vol. 14, pp. 4242–4282, 2013.

116. Teissie, J., Prats, M., Soucaille, P. and Tocanne, J. F., "Evidence for conduction of protons along the interface between water and a polar lipid monolayer," *Proc. Natl. Acad. Sci. U.S.A.,* vol. 82, pp. 3217–3221, 1985.

117. Nakano, T., Kikugawa, G., and Taku Ohara, T., "A molecular dynamics study on heat conduction characteristics in DPPC lipid bilayer," *J. Chem. Phys.,* vol. 133, pp. 154705, 2010.

118. Prats, M., Teissié, J., and Tocanne, J. F., "Lateral proton conduction at lipid–water interfaces and its implications for the chemiosmotic-coupling hypothesis," *Nature,* vol. 322, pp. 756–758, 1986.

119. Mashaghi, A., Partovi-Azar, P., Jadidi, T., Nafari, N., Esfarjani, K., Maass, P., Tabar, M. R. R., Bakker, H. J., Bonn, M., "Interfacial water facilitates energy transfer by inducing extended vibrations in membrane lipids," *J. Phys. Chem. B,* vol. 116, pp. 6455–6460, 2012.

120. *https://open.oregonstate.education/aandp/chapter/3-1-the-cell-membrane/*

121. Bretscher, M. S., "Membrane structure: some general principles," *Science,* vol. 181, pp. 622–629, 1973.

122. Baumgart, T., Hess, S. T., and Webb, W. W., "Imaging coexisting fluid domains in biomembrane models coupling curvature and line tension," *Nature,* vol. 425, pp.

821–824, 2003.

123. Karal, M. A. S., Rahman, M., Ahamed, M. K., Shibly, S. U. A., Ahmed, M., Shakil, M., "Low cost non-electromechanical technique for the purification of giant unilamellar vesicles," *Eur Biophys J,* vol. 48, pp. 349–359, 2019.

124. Jash, A., Ubeyitogullari, A., and Rizvi, S. S. H., " Liposomes for oral delivery of protein and peptide-based therapeutics: challenges, formulation strategies, and advances," *J. Mater. Chem. B*, vol. 9, pp. 4773–4792, 2021.

125. Olson, R. E., "Discovery of the lipoproteins, their role in fat transport and their significance as risk factors," *J. Nutr.,* vol. 128 (2): pp. 439S–443S, 1998.

126. http://id.nlm.nih.gov/mesh/D015217

127. Sadava, D., Hillis, D.M., Heller, H.C., Berenbaum, M.R., "Life: the science of biology," vol. 9, pp. 105–114, 2011.

128. Lewis, G. F., and Rader, D. J., "New insights into the regulation of HDL metabolism and reverse cholesterol transport," *Circ. Res.,* vol. 96 (12), pp. 1221–1232, 2005.

129. Gordon, D. J., Probstfield, J. L., Garrison, R. J., Neaton, J. D., Castelli, W. P., Knoke, J. D., JacobsJr, D. R., Bangdiwala, S., and Tyroler, H. A., "High-density lipoprotein cholesterol and cardiovascular disease. Four prospective American studies," *Circulation*, vol. 79 (1), pp. 8–15, 1989.

130. Linlin, W., Chen, H., Longquan, S., "The antimicrobial activity of nanoparticles: present situation and prospects for the future," *Int. J. Nanomedicine,* vol. 12, pp. 1227–1249, 2017.

131. Dreaden, E. C., Alkilany, A. M., Huang, X., Murphy, C. J., El-Sayed, M. A., "The golden age: gold nanoparticles for biomedicine," *Chem. Soc. Rev.*, vol. 41, pp. 2740–2779, 2012.

132. Zaman, M. M., Karal, M. A. S., Khan, M. N. I., Tareq, A. R. M., Ahammed, S., Akter, M., Hossain, A., Ullah, A. K. M. A., "Eco-friendly synthesis of Fe_3O_4 nanoparticles based on natural stabilizers and their antibacterial applications", *ChemistrySelect*, vol. 4, pp. 7824-7831, 2019.

133. Tai, C. Y., Tai, C., Chang, M., and Liu, H., "Synthesis of magnesium hydroxide and oxide nanoparticles using a spinning disk reactor," *Ind. Eng. Chem. Res.*, vol. 46 (17), pp. 5536–5541, 2007.

134. Ganapathe, L. S., Mohamed, M. A., Yunus, R. M., Berhanuddin, D. D.,

"Magnetite (Fe_3O_4) nanoparticles in biomedical application: from synthesis to surface functionalisation," *Magnetochemistry,* vol. *6*(4), pp. 68, 2020.

135.   https://www.selectscience.net/products/avanti-polar-lipids-181-%289-cis%29-pc-%28dopc%29/?prodID=216566

136.   https://avantilipids.com/product/840475

137.   https://www.istockphoto.com/vector/cholesterol-structure-of-a-molecule-gm990554220-268480575

138.   https://en.m.wikipedia.org/wiki/File:Calcein.svg

139.   Ibarra, C., Koski, J. A. & Warren, R. F., "Tissue engineering meniscus," *Orthop. Clin. North Am.,* vol. 31, pp. 411–418, 2000.

140.   Iida, H., Takayanagi, K., Nakanishi, T. & Osaka, T., "Synthesis of Fe_3O_4 nanoparticles with various sizes and magnetic properties by controlled hydrolysis," *J. Colloid Interface Sci.,* vol. 314, pp. 274–280, 2007.

141.   Reeves, J. P., Dowben, R. M., "Formation and properties of thin-walled phospholipid vesicles," *J Cell Physiol*., vol. 73, pp 49–60, 1969.

142.   Karal, M. A. S., Nasrin, T., Ahmed, M., Ahamed, M. K., Ahammed, S., Akter, S., Hasan, S., Mahbub, Z. B., "A new purification technique to obtain specific size distribution of giant lipid vesicles using dual filtration," *PLOS ONE,* vol. 16(7): e0254930, 2021.

143.   https://microbenotes.com/phase-contrast-microscopy/

144.   https://microbenotes.com/fluorescence-microscope-principle-instrumentation-applications-advantages-limitations/

145.   Fenster, A., "Handbook of medical imaging, processing and analysis," Edited by Isaac N. Bankman, PhD, Academic Press, 2000, ISBN 0-12-077790-8, 901 pp. *Ultrasound Med. Biol.* **27**, 727, 2001.

146.   Islam, M. Z., Alam, J. M., Tamba, Y., Karal, M. A. S., Yamazaki, M., "The single GUV method for revealing the functions of antimicrobial, pore-forming toxin, and cell-penetrating peptides or proteins," *Phys. Chem. Chem. Phys.,* vol. 16, pp. 15752–15767, 2014.

147.   Shepherd, J. C. W., Büldt, G., "Zwitterionic dipoles as a dielectric probe for investigating head group mobility in phospholipid membranes," *Biochim. Biophys. Acta – Biomembr,* vol. 514, pp. 83–94, 1978.

148.   Petrov, M., Cwiklik, L., Jungwirth, P., "Interactions of molecular ions with model

phospholipid membranes," *Collect. Czechoslov. Chem. Commun,* vol. 76, pp. 695–711, 2011.

149. Pabis, A., Szala-Bilnik, J., Swiatla-Wojcik, D., "Molecular dynamics study of the hydration of the hydroxyl radical at body temperature," *Phys. Chem. Chem. Phys.,* vol. 13, pp. 9458–9468, 2011.

150. Iglic, A., Kralj-Iglic, V., Majhenc, J., "Cylindrical shapes of closed lipid bilayer structures correspond to an extreme area difference between the two monolayers of the bilayer," *J. Biomech.,* vol. 32, pp. 1343–1347, 1999.

151. Seifert, U., Berndl, K., Lipowsky, R., "Shape transformations of vesicles: Phase diagram for spontaneous- curvature and bilayer-coupling models," *Phys. Rev. A,* vol. 44, pp. 1182–1202, 1991.

152. Svetina, S., Žekš, B., "Membrane bending energy and shape determination of phospholipid vesicles and red blood cells," *Eur. Biophys. J.,* vol. 17, pp. 101–111, 1989.

153. Heinrich, V., Svetina, S., Žekš, B., "Nonaxisymmetric vesicle shapes in a generalized bilayer-couple model and the transition between oblate and prolate axisymmetric shapes," *Phys. Rev. E,* vol. 48, pp. 3112–3123, 1993.

154. Miao, L., Seifert, U., Wortis, M., Döbereiner, H-G., "Budding transitions of fluid-bilayer vesicles: the effect of area-difference elasticity," *Phys. Rev. E,* vol. 49, pp. 5389–5407, 1994.

155. Dill, E. H., "Continuum mechanics: elasticity, plasticity, viscoelasticity," 1 edition. *Boca Raton*, FL: CRC Press, 2006.

156. Landau, L. D., Lifshitz, E. M., Sykes, J. B., Reid, W. H., Dill, E. H., "Theory of elasticity: vol. 7 of course of theoretical physics," *Phys. Today,* vol. 13, pp. 44, 2009.

157. Deuling, H. J., Helfrich, W., "The curvature elasticity of fluid membranes: A catalogue of vesicle shapes," *J. Phys.,* vol. 37, pp. 1335–1345, 1976.

158. Zhong-can, O-Y., Helfrich, W., "Instability and deformation of a spherical vesicle by pressure," *Phys. Rev. Lett.,* vol. 59, pp. 2486–2488, 1987.

159. Gennis, R. B., "Biomembranes: molecular structure and function*," New York: Springer-Verlag,* 1989.

160. Berndl, K., Käs, J., Lipowsky, R., Sackmann, E., Seifert, U., "Shape transformations of giant vesicles: extreme sensitivity to bilayer asymmetry,"

Europhys. Lett. EPL, vol. 13, pp. 659–664, 1990.

161. Billah, M. M., Saha, S. K., Rashid, M. M. O., Hossain, F., Yamazaki, M., "Effect of osmotic pressure on pore formation in lipid bilayers by the antimicrobial peptide magainin 2," *Phys. Chem. Chem. Phys.,* vol. 24, pp. 6716–6731, 2022.

162. Fuertes, G., Giménez, D., Esteban-Martín, S., Sánchez-Muñoz, O. L., Salgado, J., "A lipocentric view of peptide-induced pores," *Eur. Biophys. J.,* vol. 40, pp. 399–415, 2011.

163. Ludtke, S. J., He, K., Heller, W. T., Harroun, T. A., Yang, L., Huang, H. W., "Membrane pores induced by magainin," *Biochemistry,* vol. 35, pp. 13723–13728, 1996.

164. Rawicz, W., Smith, B. A., McIntosh, T. J., Simon, S. A., Evans, E., "Elasticity, strength, and water permeability of bilayers that contain raft microdomain-forming lipids," *Biophys. J.,* vol. 94(12), pp. 4725–4736, 2008.

165. Shigyou, K., Nagai, K. H., Hamada, T., "Lateral tension-induced penetration of particles into a liposome," *Materials,* vol. 10, pp. 765, 2017.

166. Lai, K., Wang, B., Zhang, Y., Zheng, Y., "Computer simulation study of nanoparticle interaction with a lipid membrane under mechanical stress," *Phys. Chem. Chem. Phys.,* vol. 15, pp. 270–278, 2012.

167. Alexeev, A., Uspal, W. E., Balazs, A. C., "Harnessing janus nanoparticles to create controllable pores in membranes," *ACS Nano,* vol. 2, pp. 1117–1122, 2008.

168. Tamba, Y., Yamazaki, M., "Single giant unilamellar vesicle method reveals effect of antimicrobial peptide magainin 2 on membrane permeability," *Biochemistry,* vol. 44, pp. 15823–15833, 2005.

169. Karal, M. A. S., Levadnyy, V., Tsuboi, T., Belaya, M., Yamazaki, M., "Electrostatic interaction effects on tension-induced pore formation in lipid membranes," *Phys. Rev. E,* vol. 92, 2015.

170. Litster, J. D., "Stability of lipid bilayers and red blood cell membranes," *Phys. Lett. A,* vol. 53, pp. 193–194, 1975.

171. Karal, M. A. S., Ahamed, M. K., Mokta, N. A., Ahmed, M., Ahammed, S., "Influence of cholesterol on electroporation in lipid membranes of giant vesicles," *Eur. Biophys. J.,* vol. 49, pp. 361–370, 2020.

APPENDIX

List of Publications

Peer reviewed journal:

Effects of cholesterol on the anionic magnetite nanoparticles-induced deformation and poration of giant lipid vesicles

Authors: <u>Salma Akter</u>, Mohammad Abu Sayem Karal, Sharif Hasan, Md. Kabir Ahamed, Marzuk Ahmed, and Shareef Ahammed

Journal: *RSC Advances,* vol. 12, pp. 28283–28294, 2022.

Conference Presentations:

1. **Salma Akter**, Sharif Hasan, and Mohammad Abu Sayem Karal; Deformation and poration of giant lipid vesicles by magnetite nanoparticles under various concentrations of cholesterol in membranes, **(Abstract-pp-81**) **International Conference on physics-2022, Organized by BPS,** Dhaka Bangladesh. 19-21 May, 2022 (Poster Presentation), pg-178,179.

2. **Salma Akter**, Sharif Hasan, and Mohammad Abu Sayem Karal; Static and Dynamic Responses of Cell like Vesicles to Magnetite Nanoparticles Under Various Concentrations of Cholesterol in Membranes for Biomedical Applications**, (Abstract-PP32-20178), International Conference on Electronic and Informatics 2021**, Dhaka, Bangladesh, 27-28 November 2021 (Poster Presentation), Pg-103.

3. **Salma Akter**, Sharif Hasan, and Mohammad Abu Sayem Karal; Effects of Cholesterol on the Anionic Magnetite Nanoparticles-Induced Deformation and Poration of Giant Lipid Vesicles**, (Abstract-MP-05), National Conference on Physics, Virtual, Organized by BPS**, Dhaka Bangladesh. 06-07 August, 2021 (Oral Presentation), Zoom online platform.

Collaborative Presentations:

1. Sharif Hasan, **Salma Akter** and Mohammad Abu Sayem Karal; Nanoparticles induced deformation and poration in lipid vesicles under various sugar concentrations**, (Abstract-pp-79), International Conference on physics-2022, Organized by BPS**, Dhaka Bangladesh. 19-21 May, 2022 (Poster Presentation), pg-178,179.

2. Sharif Hasan, **Salma Akter** and Mohammad Abu Sayem Karal; Effects of Sugar Concentration on the Magnetite Nanoparticles-Induced Deformation and Poration in Giant Lipid Vesicles**, (Abstract-BHP04-20179), International Conference on Electronic and Informatics 2021**, Dhaka, Bangladesh, 27-28 November 2021 (Oral Presentation), Pg-72.

3. Tawfika Nasrin, **Salma Akter**, Shareef Ahammed, Marzuk Ahmed, Md. Kabir Ahamed and Mohammad Abu Sayem Karal; Dual Filtration in Purification Controls the Size Distribution of Giant Vesicles**, (Abstract-SMM-06), 6th Conference (Virtual) of BAC**, Dhaka, Bangladesh, 15-16 January 2021, (Oral Presentation), Pg-107.

MATLAB Code for Compactness Measurement

```
%-----------------------------------------------------------------------------------------------
% Startup code.
tic; % Start timer.
clc; % Clear command window.
clearvars; % Get rid of variables from prior run of this m-file.
fprintf('Running BlobsDemo.m...\n'); % Message sent to command window.
workspace; % Make sure the workspace panel with all the variables is showing.
imtool close all; % Close all imtool figures.
format long g;
format compact;
captionFontSize = 14;

I0 = imread('F:\Sharif\fig 1 compactness of figure 1_ 5_27\Untitled-107825.jpg');
originalImage=im2uint16(I0(:,:,1));

% Check to make sure that it is grayscale, just in case the user substituted their own image.

% Display the grayscale image.
% subplot(1, 3, 1);
I = originalImage;
imshow(I);
h = imfreehand;
% h= imellipse;
position = wait(h);
% h = fhroi;
%
BW = createMask(h);
figure; imshow(BW)
binaryImage = BW;
% originalImage = imcrop(I,position);
% imshow(originalImage); % the output image of your ROI
```

```
% Maximize the figure window.
% Display the binary image.
subplot(1, 3, 2);
imshow(binaryImage);
title('Binary Image, obtained by thresholding', 'FontSize', captionFontSize);


labeledImage = bwlabel(binaryImage, 8); % Label each blob so we can make
measurements of it


% Let's assign each blob a different color to visually show the user the distinct blobs.
coloredLabels = label2rgb (labeledImage, 'hsv', 'k', 'shuffle'); % pseudo random color
labels


% Get all the blob properties. Can only pass in originalImage in version R2008a and later.
blobMeasurements = regionprops(labeledImage, originalImage, 'all');
peri = blobMeasurements.Perimeter;
ar = blobMeasurements.Area;
compactness = peri*peri/ar
```

Table: The elements of leaf extract according to their functional group [132]

Element Name	Element Area%	Functional Group	Area%
2,4-Decadien-1-ol	2.52	Alcohol	20.54
2,4-Pentadien-1-ol, 3-ethyl-, (2Z)	0.21		
1-Hexanol, 2-ethyl	0.49		
Benzyl Alcohol	1.87		
Phenylethyl Alcohol	3.63		
2-Adamantanol, 2-(bromomethyl)-	0.19		
Benzenemethanol, 2-chloro-	0.19		
3-Butene-1,2-diol, 1-(2-furanyl)-	0.18		
pentadecanal	0.85		
Phytol	10.41		
1,3-Benzodioxole, 4-methoxy-6-(2-propenyl)	0.87	Phenol	3.80
Phenol, 2,6-dimethoxy-4-(2-propenyl)-	0.10		
2-(4-Hodroxyphenyl)-2-(4-methoxyphenyl	0.45		
Phenol, 4,4-(1-methylethyliclene) bis-	2.16		
2-Phenyl-2-(4-trimethylsilyloxyphenyl) pr	0.22		
1-Ethyl-1-methylcyclohexane	0.94	Elkin	5.95
Spiro [2,4] hepta-4,6-diene	4.07		
Alpha-Caryophyllene	0.40		
Naphthalene, 1,2,3,4,4a,5,6,8a-octahydro-1,1,7-trimethyl-	0.35		
7-Tetradecene	0.19		
2-Cyclohexen-1-one, 4,5-dimethyl-	0.28	Ketone	5.58
2,6,6 –Trimethyle-2-cyclohexene-1, 4-dione	0.49		
3-Buten-2-one, 4-(2,6,6-trimethyl-1-cyclohexen-1-yl)-	2.11		
3-Buten-2-one, 4-(2,2,6-trimethyl-7 oxabicyclo[4.1.0]hept-1-yl)-	1.06		
2(4H)-Benzofuranone, 5,6,7,7a-tetrahydro-	0.47		

4,4,7a-trimethyl-			
Cyclooctasiloxane, hexadecamethyl-	0.63		
Cyclononasiloxane, octadecamethyl-	0.44		
2-Pentadecanone, 6,10,14-trimethyl-	0.10		
Benzaldehyde, 2,4-dimethyl-	0.26	Aldehyde	1.48
1-Cyclohexene-1-carboxaldehyde, 2,6,6-trimethyl	0.76		
2,6,6-Trimethyl-1-cyclohexene-1-acetaldehyde	0.23		
Vanillin Or 4-Hydroxy-3-methoxybenzaldehyde	0.23		
Benzenamine, 3-methyl-	0.61	Amine	12.27
Azobenzene	0.42		
Hydroxylamine, O-decyl-	0.37		
Hydroxylamine, O-decyl-	0.22		
3-(Trifluoromethyl) benzylamine 98%	5.03		
3-(Trifluoromethyl) benzylamine	1.40		
3-(Trifluoromethyl) benzylamine	1.82		
3-(Trifluoromethyl) benzylamine	2.40		
2-Hexenoic acid, 3,4,4-trimethyl-5-oxo- OR 3,4,4-trimethyl-5-oxo-2-hexenoic acid	0.27	Carboxylic Acid	11.52
Tetradecanoic acid	0.19		
8,11,14-Eicosatrienioic acid, (Z, Z,Z)-	0.09		
1,2-Benzenedicarboxylic acid, butyl 2-methyl	1.70		
n-Hexadecanoic acid	9.27		
m-Toluic acid, 4-nitrophenyl ester	0.06	Ester	1.87
9-Octadecen-12-ynoic acid, methyl ester	0.22		
Phthalic acid, isobutyl nonyl ester	0.18		
Pentadecanoic acid, 14-methyl-, methyl estar	0.73		
1,2-Benzenedicarboxylic acid, diisooctyl ester	0.68		